Aging Processes in Complex Systems

Nasrin Afzal

Dissertation submitted to the Faculty of the
Virginia Polytechnic Institute and State University
in partial fulfillment of the requirements for the degree of

Doctor of Philosophy
in
Physics

Michel Jean Pleimling, Chair
Giti Khodaparast
Hans Robinson
Eric R. Sharpe

April 1, 2013
Blacksburg, Virginia

Keywords: Equilibrium and Non-Equilibrium Statistical Physics, Soft Matter, Polymer Physics,
Aging in Biophysics, Driven Diffusive Systems, Reaction Diffusion Systems

Aging Processes in Complex Systems

Nasrin Afzal

(ABSTRACT)

Recent years have seen remarkable progress in our understanding of physical aging in nondisordered systems with slow, i.e. glassy-like dynamics. In many systems a single dynamical length L(t), that grows as a power-law of time t or, in much more complicated cases, as a logarithmic function of t, governs the dynamics out of equilibrium. In the aging or dynamical scaling regime, these systems are best characterized by two-times quantities, like dynamical correlation and response functions, that transform in a specific way under a dynamical scale transformation. The resulting dynamical scaling functions and the associated non-equilibrium exponents are often found to be universal and to depend only on some global features of the system under investigation.

We discuss three different types of systems with simple and complex aging properties, namely reaction diffusion systems with a power growth law, driven diffusive systems with a logarithmic growth law, and a non-equilibrium polymer network that is supposed to capture important properties of the cytoskeleton of living cells.

For the reaction diffusion systems, our study focuses on systems with reversible reaction diffusion and we study two-times functions in systems with power law growth. For the driven diffusive systems, we focus on the ABC model and a related domain model and measure two- times quantities in systems undergoing logarithmic growth. For the polymer network model, we explain in some detail its relationship with the cytoskeleton, an organelle that is responsible for the shape and locomotion of cells. Our study of this system sheds new light on the non- equilibrium relaxation properties of the cytoskeleton by investigating through a power law growth of a coarse grained length in our system.

This work was supported by the US National Science Foundation through Grants DMR-0904999 and DMR-1205309.

Dedicated

To my parents, sibling and my cousin Azita.

Acknowledgment

This dissertation would not have been possible without the guidance and the help of several individuals who in one way or another contributed and extended their valuable assistance in the preparation and completion of this study. First and foremost, I would like to express my appreciation for the mentoring and assistance of my advisor Professor Michel Pleimling for his untiring and unfailing support and guidance not only for my research, but also for training me to be a proper member of the scientific community. I would also like to thank other members of my committee, Prof. Giti Khodaparast, Prof. Eric Sharpe, and Prof. Hans Robinson. I am grateful to Prof. Giti Khodaparast for her great advises and support through all the stages of my PhD. I am thankful to have worked in the wonderful environment of the Non-equilibrium Statistical Mechanics group.

There are other people in the physics department who have helped me during my journey. Many thanks to Christa Thomas for her patience and guidance to get me through all the necessary steps of graduation, and for providing crucial insights during my graduate studies. I am grateful to Roger Link and Travis Heat for their great support for any kind of computational challenges that I faced. Many thanks to Betty Wilkins for making the travel arrangements fast and painless and to all the members of the machine shop for their assistance and endless support. My sincere gratitude to all the members of the physics department, faculty, staff, and fellow graduate students for providing the wonderful environment in which I studied.

It would never be possible to pursue so many years of education without the unconditional support, love, and patience from my family. I owe a great deal to my parents, my brothers, and my sisters. I would love to express my appreciation to my family and my cousin Azita who kept me motivated till the last day of my work and had never let me down.

Finally, I am immensely thankful for the financial support provided by the National Science Foundation. This material is based upon work supported by the National Science Foundation under grants No. DMR-0904999 and DMR-1205309. Any opinions, findings, and conclusions or recommendations expressed in this material are those of the author and do not necessarily reflect the views of the National Science Foundation.

Contents

1 Introduction **1**

1.1 Physical aging 1

1.2 Reversible reaction diffusion systems 3

1.3 Driven diffusive systems 5

1.4 The cytoskeleton 5

2 Aging processes in reversible reaction diffusion systems: Monte Carlo simulations **8**

2.1 Introduction 8

2.2 The model and quantities 9

2.3 Simulation results 11

2.3.1 Particle densities 11

2.3.2 Autocorrelation 12

2.3.3 Response functions 13

2.4 Conclusion 15

3 Aging processes in systems with anomalous slow dynamics **17**

3.1 Models and quantities 17

3.2 Aging in the *ABC* model 19

3.2.1 Domain growth 19

3.2.2 Autocorrelation 20

3.3 Aging in the domain model 22

3.3.1 Domain growth 22

3.3.2 Autocorrelation 23

3.3.3 Different responses . . . 24
3.4 Discussion and conclusion . . . 26

4 Dynamics of the cytoskeleton: experiments and theory 30
4.1 Soft glassy rheology . . . 30
4.1.1 Bouchaud's glass model . . . 31
4.1.2 Sollich's soft glassy model . . . 32
4.1.3 Comparison of cytoskeleton and soft glassy rheology . . . 34
4.1.4 Cytoskeleton Soft Glass Rheology (SGR) model out of equilibrium: aging . . . 35
4.2 Experimental studies . . . 36
4.3 Theoretical models . . . 37
4.3.1 Tensegrity based models . . . 38
4.3.2 Polymer based models . . . 41

5 Two-dimensional model of the cytoskeleton 46
5.1 Introduction . . . 46
5.2 Properties of the two-dimensional model . . . 47
5.2.1 Formation probability . . . 47
5.2.2 Stationary values of L_n . . . 49
5.2.3 Dissolution probability as a function of time . . . 50
5.3 Mechanical response to an external perturbation . . . 51
5.3.1 Lattice simulation: Stretching the cell . . . 51
5.3.2 Lattice simulation: Shearing the cell . . . 55
5.3.3 Lattice simulation: Returning to the original cell shape . . . 58
5.3.4 Off-lattice simulation: Stretching the cell . . . 58
5.3.5 Off-lattice simulation: Returning to the original cell shape . . . 60

6 Three-dimensional realistic model of the cytoskeleton 63
6.1 Metropolis algorithm . . . 64
6.2 Creation of a fully connected network . . . 64
6.3 Assignment of polymer length . . . 65

6.4 Energy of the system . . . 68
6.5 Rewiring . . . 69
6.6 Chopping the initial filament . . . 69
6.7 Relabeling and shifting nodes . . . 70
6.7.1 Relabeling . . . 70
6.7.2 Shifting Nodes . . . 71
6.8 Measuring a two-times function . . . 71

7 Two-times functions in the three-dimensional cytoskeleton 73
7.1 Shear perturbation . . . 73
7.2 Coarse-grained length as a function of time . . . 74
7.3 Density two-times function . . . 75
7.4 Euclidean distance two-times function . . . 78

8 Conclusion 83
8.1 Reversible reaction-diffusion system . . . 83
8.2 Coarsening systems with anomalous slow dynamics . . . 84
8.3 A non-equilibrium polymer network: the cytoskeleton . . . 84

List of Figures

1.1 By reducing the temperature, the free volume of the material decreases. When the temperature reaches T_g, the system is in a non-equilibrium state and shows aging behavior. After passing a certain temperature range, the truly glassy state is observed. 1

2.1 (a) Time evolution of the densities of A and C particles in one and two dimensions. The linear sizes of the systems are $L = 10000$ in $d = 1$ and $L = 100$ in $d = 2$, the common rates being $D_a = D_c = 0.1$ and $\mu = \lambda = 0.5$. Initially the systems consist only of C particles that randomly occupy 30% of the lattice sites. (b) The approach to stationarity is governed by a power law with exponent $d/2$, as indicated by the dashed straight segments. The data shown here result from averaging over 400000 independent runs [70]. 12

2.2 The scaling of the autocorrelation function $C_C(t,s)$ for C particles in (a) $d = 1$ and (b) $d = 2$ dimensions. The diffusion rates are $D_a = D_c = 0.05$, whereas the reaction rates are $\mu = \lambda = 0.5$, the initial state being composed only of C particles that randomly occupy 30% of the lattice sites. The red dashed lines show the asymptotic scaling functions obtained for the exactly solvable model studied in [33], see equation (2.11). The data result from averaging over at least 30000 independent runs [70]. 13

2.3 The scaling of the time integrated response $M_K(t,s)$, see equation (2.8), in (a) $d = 1$ and (b) $d = 2$ dimensions. The diffusion rates are $D_a = D_c = 0.5$, whereas the reaction rates are $\mu = \lambda = 0.5$. The rates for injecting C particles and removing pairs of A particles are $r_K = 0.01$ in $d = 1$ and $r_K = 0.05$ in $d = 2$. Initially 14% of the sites are occupied by A particles, whereas C particles are randomly deposited on 23% of the sites. The data shown here have been obtained after averaging over typically one million independent runs [70]. . . 14

2.4 The scaling of the time integrated response $M_C(t,s)$, see equation (2.9), in (a) $d = 1$ and (b) $d = 2$ dimensions. The diffusion rates are $D_a = D_c = 0.05$, whereas the reaction rates are $\mu = \lambda = 0.5$. The injection rates of C particles is $r = 0.0001$ in both cases. Initially 14% of the sites are occupied by A particles, whereas C particles are randomly deposited on 23% of the sites. The data shown here have been obtained after averaging over typically 250000 independent runs. Note that the response is waiting time independent and that the decay is algebraic for large times, with exponent $d/2$, as indicated by the dashed lines [70]. 15

3.1 (Color online) Time-dependent average domain size for the *ABC* model with various values of the rate q. After some initial regime, that lasts longer the larger the value of q, logarithmic growth sets in. The slopes in the log-linear plot increase with q. The data result from averaging over 600 independent runs. (Reprinted figure with permission from [76]. Copyright (2013) by the American Physical Society). 20

3.2 (Color online) Autocorrelation function for the *ABC* model with (a,b) $q = 0.9$ and (c,d) $q = 0.3$. For every waiting time s we compute the autocorrelation function for up to $t = 40\,s$ time steps. Plotting the autocorrelation against the scaling variable $L(t)/L(s)$, see (b) and (d), yields indications for the onset of dynamical scaling for the longest waiting times. The data result from averaging over at least 600 independent run (Reprinted figure with permission from [76]. Copyright (2013) by the American Physical Society.) 21

3.3 (Color online) Time-dependent average domain size for the domain model for various values of the rate q. Logarithmic growth is observed where the slopes in the log-linear plot increase with q. The data result from averaging over at least 100 independent runs. (Reprinted figure with permission from [76]. Copyright (2013) by the American Physical Society.) 23

3.4 (Color online) Autocorrelation function for the *ABC* model with (a,b) $q = 0.9$ and (c,d) $q = 0.7$. Plotting the autocorrelation against the scaling variable $L(t)/L(s)$, see (b) and (d), yields a perfect data collapse. The data result from averaging over 50000 independent runs. (Reprinted figure with permission from [76]. Copyright (2013) by the American Physical Society.) 24

3.5 (Color online) Time evolution of the average growth length when changing after the waiting time s the value of the rate q from 0.9 to 0.8 (upper colored lines) or from 0.7 to 0.8 (lower colored lines). The different waiting times are s=20000 (blue lines), s=60000 (green lines), and $s = 100000$ (red lines). (Reprinted figure with permission from [76]. Copyright (2013) by the American Physical Society.) 26

3.6 (Color online) Response function for the *ABC* model where at the waiting time s the exchange rates are decreased from some initial value q_i to the final value q_f: (a,b) $q_i = 0.9$ and $q_f = 0.85$, (c,d) $q_i = 0.8$ and $q_f = 0.7$. Plotting the response function against the scaling variable $L(t)/L(s)$, see (b) and (d), yields a perfect data collapse. The data result from averaging over 10000 independent runs. (Reprinted figure with permission from [76]. Copyright (2013) by the American Physical Society.) 27

3.7 (Color online) Response function for the *ABC* model where at the waiting time s the exchange rate is increased from the initial value $q_i = 0.8$ to the final value $q_f = 0.9$. The waiting times are the same as in Fig. 3.5. As the different curves intersect, see inset, no data collapse can be achieved by simply multiplying $M(t,s)$ with a waiting time dependent constant. The data result from averaging over 10000 independent runs. (Reprinted figure with permission from [76]. Copyright (2013) by the American Physical Society.) 28

4.1 The energy landscape displays different metastable states in Bouchaud's model. 31

4.2 Elements escape from a metastable trap to another metastable one. 33

4.3 The solid lines represent the experiment data and the dashed lines are the regression fit of the SGR model to the data of the experiment [118]. The fitted local elasticities are given as $14.9, 11.1, 5.5, 3.6$ kPa for the cases of x/x_g, $1.17, 1.20, 1.28, 1.33$ respectively (Reprinted from [87] with permission from ELSEVIER.). 35

4.4 In a MTC experiment a bead is attached to the cell surface. The magnetic field applies torque on the bead. This mechanical perturbation moves the center of mass of the bead connected to the cell surface. 39

4.5 A cable-and-strut tensegrity dome. In this structure, tension in the cables (blue lines) is partly balanced by the compression of the struts (thick black lines) and partly by the attachments to the substrate. At each free node one strut meets several cables. 40

4.6 Six-strut tensegrity model in the round (a) and spread (b) configurations anchored to the substrate. Anchoring nodes A1, A2 and A3 (round) and A1, A2, A3, B1, B2, and B3 (spread) are indicated by solid triangles. Pulling force F (thick arrow) is applied at node D1. 40

4.7 s is the arc parameter along the polymer. $\theta(0)$ is the angle between the tangent line at $s = 0$ and the x axis of the chosen coordinates for the filament whereas $\theta(s)$ is the corresponding angle at arc length s. As the arc length increases, the tangent angles $\theta(0)$ and $\theta(s)$ become uncorrelated. 41

5.1 (a) For small values of s, s=2, lengths of the created links are both short and long. (b) For large values of s, s=7, most of the created links are between nearest neighbors. 48

5.2 The number of nodes are increasing from 5^2 to 60^2. When the number of nodes increases, the time to reach the stationary state increases. 48

5.3 Stationary value, P_l, is plotted as a function of the number of crosslinks, N, in the network. . 49

5.4 For $N = 40$, $s = 0$, $b_0 = b_1 = 0.5$, and $\tau = 10000$, we plot the number of links as a function of time. The black curve is the number of links for constant dissolution probability, $B_{ij} = b_0 = 0.5$. The red curve is the number of links when B_{ij} is a function of time. The system with time dependent B_{ij} takes longer to reach the stationary value. 51

5.5 (a) Initial cell is shown. (b) Cell is stretched with constant area. The horizontal direction (x-direction) is compressed by α and the vertical direction (y-direction) is stretched by $1/\alpha$ ($\alpha < 1$). (c) Cell is sheared with constant area and shear angle β. 52

5.6 At time $t = 30,000$ the cell is stretched. For $\alpha < 0.6$ the number of links increases before reaching a stationary state. For other values of α the number of links is decreasing monotonously. The data result from averaging over 1000 independent runs. 52

5.7 For $N^2 = 20^2$, $s = 2$, $\alpha = 0.8$ and 50 realizations, the number of links in x, y and diagonal directions are shown in the graph. The total number of links L_n (black) is increasing after stretching the system. The number of links in diagonal direction, L_{nd}, (red) decreases after the stretch. The number of links in x direction, L_{nx}, (green) increases, because the cell is compressed in x direction and the distance between nodes becomes shorter. The number of links in y direction, L_{ny}, (blue) is decreasing since the cell is stretched in y direction and the distance between nodes is increasing. The initial jump in the total number of links comes from the non-adjusted number of links in y and diagonal directions. 53

5.8 For a system with $s = 7$, $N = 5$, and $\alpha = 0.2$, the probability distribution of the links as function of the Euclidean distance, r, is shown. At time $t = T - 5$ (black line), the maximum value of the distribution is at $r = 1$. At time $t = T$ (red line), most of the links are at $r = 0.2$ and $r = 5$. At time $t = T + 4$ (green line), more links are created with short length and longer links are dissolved in the system. At large observation time $t = T + 25000$ (blue line), most of the links have short length. 54

5.9 Probability distribution of links as function of distance r for $s = 3$, $N = 20$, $\alpha = 0.2$, and 20 realizations. As s is a small value, the links can have both short and long length as shown for $t = T - 5$ (black color). At time $t = T$ (red color), the cell is stretched with $\alpha = 0.2$. At large observation time $t = T + 25000$ (green color) the number of long links decreases. . . . 55

5.10 The number of links reaches a new stationary value after shearing the cell. Here the data is obtained for $N = 5$, $s = 3$, $\beta = 45$. 56

5.11 For different values of s from 0 to 7 the system reaches different stationary states after shearing the cell.Typically the new stationary state value is characterized by a larger stationary value of L_n. 57

5.12 As the data show for $\beta = 45$, $N = 5$, and $s = 7$, before the shear at time $T - 5$ and after the shear at time $t > T$, most of the links are nearest neighbor links with $r = 1$. 57

5.13 For $N = 5$ and $s = 2$, the number of links is plotted as a function of time for different shear angles. The shear angle β is increasing from 30 to 60. The number of links increases when β increases. 58

5.14 (a) For $N = 10$, $s = 4$, $\alpha = 0.1$ and 100 realization, the total number of links (black) and the number of links in x (red), y (green) and diagonal directions (blue) are shown. By gradually changing the stretching coefficient, α, from 0.1 to 1, L_{nx} is decreasing, whereas L_{ny} and L_{nd} are increasing in time. (b) For $N = 10$, $s = 5$, $\alpha = 0.1$ and 100 realization, the total number of links (black) and the number of links in x (red), y (green) and diagonal directions (blue) are shown. 59

5.15 For $N = 10$, $s = 7$, $\alpha = 1$ and 1000 realizations, the number of links in x, y and diagonal directions have the same stationary value. 59

5.16 In the off-lattice case for $N = 10$, $s = 7$, $\alpha = 0.2$ and 1000 realizations, the number of links in x, y and diagonal directions reach to the same stationary value. 60

5.17 For $N = 10$, $s = 7$, $\alpha_0 = 0.2$, $\alpha = 1$ and 1000 realizations, the numbers of links in *x*, *y* and diagonal directions are changing very slowly when changing α from 0.2 back to 1. Here $T_0 \gg T$, as $T = 50000$ and $T_0 = 5000000$. 61

5.18 For $N = 10$, $s = 7$, $\alpha_0 = 0.2$, $\alpha = 1$ and 1000 realizations, the numbers of links in *x*, *y* and diagonal directions are changing slowly when changing α from 0.2 back to 1. Here $T_0 \sim T$, as $T = 50000$ and $T_0 = 50000$. 61

5.19 For $N = 10$, $s = 7$, $\alpha_0 = 0.2$, $\alpha = 1$ and 1000 realizations, the numbers of links in *x*, *y* and diagonal directions are changing very fast when changing α from 0.2 to 1. ($T \gg T_0$ and $T = 50000$ and $T_0 = 500$) 62

6.1 All the crosslinks are inside the original box. 65

6.2 At each time step the nearest segment, *AC*, to the new node, *B*, is deleted and two new links, *AB* and *BC*, are created. 65

6.3 There are some cases that are not allowed. (a) Old node, *A*, and new node, *B*, should not already be connected. (b) Old node and new node should not be connected to common neighbors, as then one would not have a segment to delete. (c) Segment chosen for deletion should not be connected to any of the segments connected to new node. Here *AC* is the only allowed segment, as its deletion allows us to add two new segments, *BC* and *AC*. 66

6.4 Schematic picture of final network. There are four links connected to each crosslink. 66

6.5 Analytical equation and Monte Carlo simulation of $G(r)$ plotted vs *r*. For different values of $L_c/l_p = 10, 5, 2, 1$, and 0.5 the maximum is shifted from right to left. Solid lines are obtained from Eq. 6.2 for the provided ratio and the dashed lines are Monte Carlo simulation results (Reprinted figure with permission from [123]. Copyright (1996) by the American Physical Society.) 67

6.6 (a) For each segment, a contour length is assigned. (b) At the end there is a long entangled filament. 68

6.7 Two segments *i* and *j* are connected to each crosslink. The angle between segment *i* and *j* is $\theta_{i,j}$, and $L_{c,i}$ and $L_{c,j}$ are contour lengths assigned to segment *i* and segment *j* respectively. 68

6.8 Two old links, *AB* and *CD*, are deleted and two new ones, *AC* and *BD*, are created. 69

6.9 (a) The initial long entangled filament is chopped into smaller filaments until the desired number of filaments is reached. (b) By following the filaments, we can go from each node to every other one. (c) There are some filaments which are not connected anymore. 69

6.10 (a) One-fold-connected crosslinks can be end points or initial points of a filament. (b) A two-fold-connected crosslink is a regular point that is a connection node between two segments of one filament. (c) A three-fold-connected crosslink involves two different filaments. One filament is indicated by a single arrow, and the other one is indicated by a double arrow. For the single arrow filament, the shown crosslink is a regular point and for the double arrow filament it is an end or initial point. (d) A four-fold-connected crosslink is a regular point for two different filaments. 70

6.11 (a) For the energy calculation four segments and three angles are needed. (b) A four-fold-connected crosslink is chosen randomly. The solid line is one filament and the dashed line is another one. *AOB* and *DOC* are the angles for the two filaments. With the Metropolis rate, the two tails of the two filaments are switched. The new assigned filaments'angles are *AOC* and *DOB*. 71

6.12 Node *O* is chosen randomly. The coordinates will change by $0.05l_p$. A new polymer length will be assigned to each of the changed segments. 71

6.13 There are four types of perturbations: bulk, shear, unilateral and uniaxial strains. 72

6.14 Each Euclidean distance can grow or shrink during time. 72

6.15 Crosslinks at time $t = s$ are in the center of a circle with radius $0.1l_p$. At later times, crosslinks moving in the cell can move outside of the assigned circles. At time $t \gg s$, most of the crosslinks are no longer in the initial circles. 72

7.1 The cell is brought out of equilibrium at time $t = 0$ when it is sheared. The shear angle is kept constant when measuring the two-times functions. After the shear the system relaxes to a new equilibrium state. Some polymers, like the blue colored one, are stretched. The red colored polymer is buckled and the green colored polymer does not show any changes. The magenta and pink colored polymers are stretched and buckled in some parts. 73

7.2 For $l_p = 0.1$, $f = 4$, $m = 30$, $\mu = 10$, and $\alpha = 60$, the average Euclidean distance at each time step $< R(t) >$ is plotted vs t. 74

7.3 For $l_p = 1$, $f = 8$, $m = 30$, $\mu = 10$, and $\alpha = 60$, the average Euclidean distance $< R(t) >$ as a function of t displays an initial time regime before algebraic growth sets in. 75

7.4 For $l_p = 10$, $f = 8$, $m = 30$, $\mu = 10$, and $\alpha = 60$, the average Euclidean distance at each time step $< R(t) >$ is plotted vs t. 76

7.5 (a) The density autocorrelation function is plotted vs $t - s$. (b) The same data, but now plotted as a function of $\ln(t - s)$. The data reveal the existence of three distinct regimes. . . . 77

7.6 (a) The density autocorrelation function vs observation time t for the set of data shown in Fig. 7.4. (b) The density autocorrelation function is plotted vs t/s for the same set of data. . 77

7.7 Dynamical scaling of the density autocorrelation function plotted as a function of t/s. The dynamical exponent is $b = -0,107$. 78

7.8 (a) The density autocorrelation function plotted as a function of $< R(t) >$ is showing three parallel curves for three waiting times $s = 50$ (black curve), 100 (red curve), and 200 (green curve). (b) The same data is plotted as a function of $< R(t) > / < R(s) >$. 78

7.9 Dynamical scaling of the density autocorrelation function when plotted as a function of $< R(t) > / < R(s) >$. The data shows simple aging in the system with the exponent $b = -1.72$. 79

7.10 There are some situations where the Euclidean distance two-times function provides additional information on the conformation of the system. (a) Two crosslinks are out of the assigned spheres with radius $0.1l_p$. (b) Only one of the crosslinks is out out of its sphere. (c) Two of the crosslinks change their location but they are still inside the spheres. For this case the density two-times function will not show any change. 79

7.11 For $l_p = 10$, $f = 12$, $m = 30$, $\mu = 10$, and $\alpha = 60$, the average Euclidean distance two-times functions, $C(t,s)/C(s,s)_{ED}$, is plotted vs t/s. 80

7.12 For $l_p = 10$, $f = 12$, $m = 30$, $\mu = 10$, and $\alpha = 60$, the average Euclidean distance two-times functions, $C_{ED}(t,s)$ is plotted vs $< R(t) >$. 81

7.13 For $l_p = 0.1$, $f = 8$, $m = 30$, $\mu = 10$, and $\alpha = 60$, the average Euclidean distance two-times functions, $C_{ED}(t,s)$, is plotted vs $< R(t) >$. 81

7.14 (a) $C(t,s)_{ED}$ vs $< R(t) >$ for $l_p = 0.1$, $f = 4$, $m = 30$, $\mu = 10$, and $\alpha = 60$. (b) $[C(t,s)/C(s,s)]_{ED}$ vs $< R(t) > / < R(s) >$. 82

List of Tables

5.1 For N=40 and different s values, the time to reach to stationary value, T_1, is changing. T_1 increases when $s \leq 2$, but decreases for larger values of s. 48

5.2 When the exponent, s, increases from 0 to 7, the exponent q decreases from almost 4 to 2. . . 50

5.3 For $s < 3$, the typical time constant, T', is increasing. For larger values of s the time constant of the system is decreasing. 51

5.4 For different number of nodes $N = 5, 10, 20$ and $s = 1, 2, 3, 4, 5, 6, 7$, the total number of links, L_n, is changing as a power law of time with the exponent listed here. 55

5.5 For different number of nodes $N = 5, 10, 20$ and $s = 1, 2, 3, 4, 5, 6, 7$, the number of links in y direction, L_{ny}, is changing as a power law of time with the exponent listed here. 55

5.6 For different number of nodes $N = 5, 10, 20$ and $s = 1, 2, 3, 4, 5, 6, 7$, the number of links in diagonal direction, L_{nd}, is changing as a power law of time with the exponent listed here. . . 56

Chapter 1

Introduction

1.1 Physical aging

Physical aging is an important phenomenon observed in many materials, ranging from organic and inorganic glasses to some of the metals[1]. Fig. 1 illustrates aging in the context of glasses. When cooling down a glass, the system passes from the equilibrium behavior to the aging regime after passing the glass transition temperature T_g. After reaching even lower temperature, the system displays the truly glassy state.

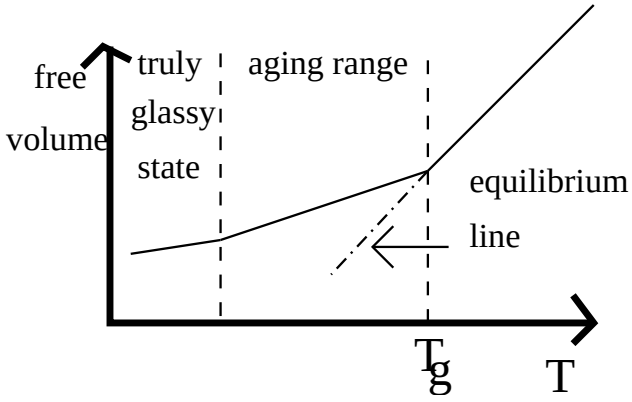

Figure 1.1: By reducing the temperature, the free volume of the material decreases. When the temperature reaches T_g, the system is in a non-equilibrium state and shows aging behavior. After passing a certain temperature range, the truly glassy state is observed.

This behavior has been seen in most of the materials studied by Struik [1]. Later theoretical studies have investigated in more detail non-equilibrium relaxation and aging in materials far from equilibrium. Aging in general refers to slow dynamics out of equilibrium that changes the properties of the material without presence of an external perturbation. Aging relaxation is displayed in a system brought out of equilibrium by a rapid change of a thermodynamic state variable. Additionally, fluctuation effects are large enough in the system to prevent the system from returning rapidly to the stationary state. In early studies physical

aging has mainly been studied in glassy systems. In our study we are focusing on non-glassy systems with aging behavior.

The first systematic study of physical aging dates back to 1978 and was done by Struik [2]. This experiment studies the slow dynamics inside a certain type of glass forming system, the so-called PVC. After quenching the system below the glass transition temperature, T_g, Struik observed that the dynamics slowed down and the system fell out of equilibrium. In Struik's study mechanical stress was added to the system and the mechanical response of the system was measured after the waiting times s. The data showed that the longer the waiting time was, the slower the system reacted to changes. Additionally, the data showed dynamical scaling for various waiting times s.

In general, the following protocol is used for studying aging in different systems [3],

1. Prepare the system in a high temperature state.
2. Quench the system rapidly to a low temperature where several equilibrium states exist.
3. Fix the temperature and measure the response of the system to an external perturbation.

Often the relaxation process towards a stationary state obeys the following properties [3]:

1. Slow dynamics.
2. Breaking of time-translation-invariance.
3. Dynamical scaling.

In the aging regime where the waiting time and the observation time are larger than any microscopic time scale in the system, a single dynamical length $L(t)$ emerges. The dynamics of the system in that regime is dominated by this length. This length changes as a function of time. Commonly encountered growth laws are $t^{1/z}$, where z is called dynamic exponent, or $L(t) \sim (\ln t)^{1/\psi}$ with $\psi > 0$.

Typical two-times quantities used to study physical aging of a system are the autocorrelation and autoresponse functions. The autocorrelation function, $C(t,s)$, shows the correlation of the two configurations of the system at times s and $t > s$. Here s is the waiting time and t is the observation time. The response function, $R(t,s)$, measures the response of the system to an external perturbation. For systems with a growth law $L \sim t^{1/z}$, the following scaling behavior is expected:

$$C(t,s) = s^{-b} f_c(t/s), \quad R(t,s) = s^{-1-a} f_R(t/s) \tag{1.1}$$

with the asymptotic behavior of the scaling functions,

$$f_C(y) \sim y^{-\lambda_C/z}, \quad f_R(y) \sim y^{-\lambda_R/z} \, . \tag{1.2}$$

The exponents a, b, λ_C, and λ_R are non-equilibrium exponents that govern the scaling properties of the two-time quantities. However, in some systems the typical length is growing as $L \sim (\ln t)^{1/\psi}$. In the aging regime, one then expects for these systems the following generalized scaling forms for the correlation and the response functions,

$$C(t,s) = (L(s))^{-b} f_C\left(\frac{L(t)}{L(s)}\right) \tag{1.3}$$

$$R(t,s) = (L(s))^{-1-a} f_R\left(\frac{L(t)}{L(s)}\right) \tag{1.4}$$

with the scaling functions $f_C(y)$ and $f_R(y)$ and the non-equilibrium exponents a and b. Here times are expressed through the time-dependent growth length $L(t)$.

In my PhD work, I have focused on three different systems with slow dynamics: reaction-diffusion systems, driven diffusive systems, and biological protein network, e.g. the cytoskeleton of living cells, using computational modeling and non-equilibrium statistical mechanics techniques. Reaction-diffusion systems with reversible reactions display power-law relaxation toward equilibrium. In our model we investigate the aging processes of systems with single occupancy of each site. The two-time functions of the system display dynamical scaling similar to the results discovered previously in an exactly solvable version with no restrictions on the occupation numbers. The second systems I studied are driven-diffusive systems. Previous numerical studies of coarsening in disordered systems have shown a crossover from an initial, transient, power-law domain growth to a slower, presumably logarithmic, growth. Due to the slow dynamics, the asymptotic regime can usually not be accessed in the disordered systems. We study two simple driven systems, the one-dimensional ABC model and a related domain model with simplified dynamics, that are known to exhibit anomalous slow relaxation where the asymptotic logarithmic growth regime is readily accessible. We study the aging in the systems via two-times functions in the logarithmic regime. The asymptotic behavior of these systems is expected to share common features with the asymptotic regime of disordered ferromagnets and spin glasses. The last system I focused on is a semiflexible protein network inside eukaryotic cells, the so-called cytoskeleton. This organelle inside the cell is responsible for the cell motility. In this context we study the response of a Worm-Like-Chain model through Monte Carlo simulations. After preparing the system in a relaxed state, different perturbations, e.g. shear strain, bulk strain, unilateral strain, or uniaxial strain, are applied and the relaxation processes are monitored. We measure two-times functions of various quantities. The results show the existence of slow relaxation and aging in this system.

The following subsections briefly discuss these systems, whereas a detailed discussion is done in the following chapters. In chapter 2 we study reversible reaction diffusion systems, whereas in chapter 3 we focus on aging in driven diffusive systems. In chapters $4, 5, 6,$ and 7 we study two-and three-dimensional models that have been proposed to describe the dynamic properties of non-equilibrium polymer networks like the cytoskeleton.

1.2 Reversible reaction diffusion systems

Slow dynamics and aging processes are encountered in a huge variety of systems. The best known examples can of course be found in glassy systems, i.e. structural glasses and spin glasses, but intensive research in the last decade has revealed that these processes are ubiquitous and can be found in magnetic systems, in non-equilibrium growth or in diffusion-limited reaction systems. Slow dynamics in non-glassy systems is often much easier to understand than in the more complex glassy systems, and much progress in our

understanding of the general properties of aging processes has been achieved through the study of rather simple model systems with slow dynamics. Reaction-diffusion systems have greatly contributed to our current understanding of the physics far from equilibrium. This is especially true for non-equilibrium phase transitions as encountered in systems with irreversible reactions and absorbing states [4, 6]. In this context, the study of relaxation and aging phenomena remains in its early stages. Still, some interesting results have been found recently. As is well known, power-law relaxation, the hallmark of slow dynamics, is observed in diffusion-limited irreversible reactions at their (non-equilibrium) phase transition points. Consequently, the first studies of aging in reaction-diffusion systems were restricted to these non-equilibrium critical points that are characterized by the absence of detailed balance [7, 8, 9, 10, 11, 12, 13, 14, 35, 16, 17, 18]. The analysis of two-time correlators $C(t,s)$ and responses $R(t,s)$ at an absorbing phase transition revealed a phenomenology similar to that observed at an equilibrium critical point. Both quantities exhibit the standard scaling forms (1.2) and the scaling functions display a simple power-law behavior for large arguments, $y = t/s \gg 1$, see equation (1.3). These studies also revealed some remarkable differences to the aging properties of systems relaxing towards an equilibrium steady state. Most notably, the exponents a and b, which for a system relaxing towards equilibrium are identical and related to a static critical exponent [3], can be different when detailed balance is broken. In some cases this difference can be understood through symmetry properties of the model, as for example for the contact process [13], in other cases no simple explication seems to exist.

In order to observe slow dynamics at an absorbing phase transition, a fine-tuning of the system parameters is obligatory. This is, however, different for systems with reversible reactions, as these systems generically display power-law relaxation, independent of the values of the reaction and diffusion rates [19, 20, 21, 22, 23, 24, 25, 26, 27, 28, 29]. Studies of excited-state proton transfer reactions provided experimental verifications of this theoretically predicted behavior [30, 31, 32]. This of course makes the diffusion-limited systems with reversible reactions very attractive for a study of aging processes.

In [33] a first step was undertaken in that direction where the non-equilibrium dynamical properties of some exactly solvable models were studied. This study indeed revealed the presence of the standard scaling forms (1.2) for correlation and response functions, and this for any values of the system parameters. Surprisingly, however, the scaling of the response function was found to strongly depend on whether or not some specific quantity was kept constant when perturbing the system. This is an interesting result, as it highlights the importance of conserved quantities during non-equilibrium relaxation.

The models studied in [33] are to some extend specialized in order to be exactly solvable. It is therefore of interest to understand which of the properties found in [33] are generic to systems with reversible reactions and which depend on special features of the studied models. Thus, in order to be soluble, it was assumed that the possible number of particles at every lattice site was unrestricted. In addition, as initial condition an uncorrelated Poisson distribution on each lattice site and for each particle species was assumed. In chapter 2 we study a system composed of two types of particles that undergo reversible reactions while diffusing on a lattice. We thereby only allow single site occupation and prepare the system by randomly distributing on the lattice a given number of particles of every type. During the relaxation process we study the two-time autocorrelation function as well as different two-time response functions.

1.3 Driven diffusive systems

Growth laws can be much more complicated than simple power laws, as discussed recently in disordered ferromagnets quenched below their critical temperature. Thus, convincing evidence for a dynamic crossover between a transient regime, characterized by a power-law growth with an effective dynamical exponent that depends on the disorder, and the asymptotic regime, where the growth is logarithmic in time, has been found in recent studies of the dynamics of elastic lines in a random potential [37, 38, 39, 40] as well as in numerical simulations of disordered Ising models [41, 43, 44, 45]. These indications are compatible with the classical (droplet) theory of activated dynamics that, under the assumption of energy barriers growing as a power of L, predicts a slow logarithmic increase [46] of this length:

$$L \sim (\ln t)^{1/\psi}, \tag{1.5}$$

with the barrier exponent $\psi > 0$. However, none of the recent numerical studies was able to fully access the asymptotic regime when following the time evolution of the system, and therefore a systematic study of aging processes in this regime with logarithmic growth has not yet been done.

In chapter 3, we study two one-dimensional models that exhibit anomalous slow dynamics and that are known to display coarsening where the length of the domains increases logarithmically with time [47]. Even though these models are in no way related to disordered ferromagnets and spin glasses, their studies should allow us to gain a better understanding of the generic properties of an aging system with a logarithmic growth law.

The models discussed in chapter 3 are the so-called *ABC* model [48], a driven diffusive system composed of three different types of particles that swap places asymmetrically, and a related domain model [49] whose simplified dynamics is supposed to capture the dynamics of the *ABC* model at the later stages of the coarsening process. The *ABC* model has recently yielded a flurry of interesting studies [50, 51, 52, 53, 54, 55, 56, 57, 58, 59, 60, 61, 62, 63] that helped establishing it as a paradigm for systems far from equilibrium. Not only is the *ABC* model characterized by its anomalous slow dynamics, making it a representative for a larger class of systems with a similar coarsening process [64, 65, 66, 67, 68], it also exhibits a variety of interesting non-equilibrium phase transitions whose properties change dramatically when breaking certain conservation laws. The domain model has been proposed as a simplified version of the *ABC* model where only movements of particles between domains of the some species are considered. This simplified dynamics accelerates the coarsening process and allows to enter the purely logarithmic growth regime faster [49]. We use the *ABC* model in order to investigate the onset of dynamical scaling, whereas the domain model is used to characterize aging scaling deep inside the logarithmic growth regime.

1.4 The cytoskeleton

We here briefly summarize some of the main characteristics of the cytoskeleton as well as some of the properties of the main types of filaments forming the cytoskeleton. The cytoskeleton is a protein network inside eukaryotic cells that provides mechanical structure to the cell. Hence this organelle is responsible for cell motility and exerts forces inside and outside of the cell. There are many processes involving the cytoskeleton. These processes are establishing the cell shape and structure, and are responsible for the mechanical

strength of the cell, locomotion, chromosome separation in mitoses and meiosis, cellular division, and intracellular transport of organelles. This protein network consists of three different types of protein filaments: actin filaments, intermediate filaments and microtubules. The different filaments have different properties and play different roles in the cell.

Actin filaments, which helps strengthening the cell, play a central role in the cell. Actin can show up in various forms inside the cell, as actin monomers, actin bundles, or actin gel. Actin is mainly located under the membrane of the cell, in a region called the actin cortex. The actin cortex helps moving the membrane through the polymerization and depolymerization of filaments. Actin filaments are formed by globular monomers or G-actin. The persistence length of actin depends on the decoration of the filaments. The reported length is between $9 \pm 0.5 \mu$m for bare actin and 20μm for actin in skeletal muscle cells [107]. The actin filament has two ends with two types of behaviors. One end is called ”plus end”, ”fast growing end”, or ”barbed end” where mostly ATP-bound (adenosine triphosphate) monomers are located. The other end, called ”minus end” or ”slow growing end”, has a high concentration of ADP-bound (adenosine diphosphate) monomers. The two different ends are involved in ”the treadmilling phenomenon” [107] : adding monomers from one end and removing monomers from the other end. This process moves the center of mass of the filament with a velocity of the order of a few micrometers per hour [107]. The presence of some binding proteins helps to increase the speed of the center of mass. This is the reason that actin plays an important role in cell motility. Actin monomers are also the most concentrated monomers inside the cytoplasm [107]. They also appear in various structures such as linear bundles, two-dimensional network and three-dimensional gel. Two vital structures that help cell motility are the two-dimensional actin networks in lamellipodia and linear bundles in filopodia that extend out from the lamellipodia.

A second type of protein filaments is formed by intermediate filaments (IF). As the name shows, the radius of these filaments is between those of microtubules and actin filaments. Intermediate filaments help to shape and strengthen the cell. They are formed by two stranded helical polymers. The radius of the filaments ranges from $r = 7$ nm to 12 nm [107]. Intermediate filaments are the most flexible filaments inside the cell, with persistence lengths ranging from 0.3 to 1μm. Different types of intermediate filaments form different families. The most important shared property between all intermediate filaments is that they are not polar and that they do not treadmill like actin or microtubules. They mainly participate in the structural and elastic properties of the cell and are rarely involved in the cell motility. Intermediate filaments are more stable in comparison to the two other main filaments and usually are involved in transcellular junctions and in the attachment to the extra cellular matrix [81].

Microtubules are hollow cylinders and are the thickest polymers in the network. They originate from cytosol, the organelle near the nucleus, and usually grow in one direction, but can shrink as well. Microtubles participate in cell division and in the intracellular or vesicle transport [81]. Microtubules have an outer diameter of 25 nm and a persistence length of 100μm to 6 mm [107]. This hollow cylinder is formed from building blocks called heterogeneous tubuline subunits. These subunits bind to guanosine triphosphate (GTP) or guanosine diphosphate (GDP). The tubuline is a heterodimer of α-subunits and β-subunits [107]. Microtubules are polar polymers and they treadmill and exert forces on the surrounding.

There are a number of motor proteins that play many roles in the cytoskeleton inside cell. These motor proteins are involved in processes such as the crosslinking between two filaments, the creation of bundles of actin filaments, the chopping of long filaments into smaller ones, or the capping the filaments that stops their growth.

The cytoskeleton dynamics has been studied experimentally [117]. The empirical data can be described using the Soft Glass Rheology model of Sollich for the cytoskeleton. This description is successful as long as there is small strain on the system and the linear properties are observed in the dynamical moduli. For more complicated situations, with large strain on the cytoskeleton and in nonlinear regime, further theoretical studies need to be done.

Chapter 2

Aging processes in reversible reaction diffusion systems: Monte Carlo simulations

N. Afzal, J. Waugh, and M. Pleimling, J. Stat. Mech. (2011) P06006.

2.1 Introduction

Reaction-diffusion systems with reversible reactions generically display power-law relaxation towards chemical equilibrium. In this chapter which closely follows my paper [70] we investigate through numerical simulations aging processes that characterize the non-equilibrium relaxation. Studying a model which excludes multiple occupancy of a site, we find that the scaling behavior of the two-time correlation and response functions are similar to that discovered previously in an exactly solvable version [33] with no restrictions on the occupation numbers. Especially, we find that the scaling of the response depends on whether the perturbation conserves a certain quantity or not. Our results point to a high degree of universality in relaxation processes taking place in diffusion-limited systems with reversible reactions [70].

Reaction-diffusion systems have greatly contributed to our current understanding of the physics far from equilibrium. This is especially true for non-equilibrium phase transitions as encountered in systems with irreversible reactions and absorbing states [4, 6]. In this context, the study of relaxation and aging phenomena remains in its early stages. Still, some interesting results have been found recently. As is well known, power-law relaxation, the hallmark of slow dynamics, is observed in diffusion-limited irreversible reactions at their (non-equilibrium) phase transition points. Consequently, the first studies of aging in reaction-diffusion systems were restricted to these non-equilibrium critical points that are characterized by the absence of detailed balance [7, 8, 9, 10, 11, 12, 13, 14, 35, 16, 17, 18]. The analysis of two-time correlators $C(t,s)$ and responses $R(t,s)$ at an absorbing phase transition revealed a phenomenology similar to that observed at an equilibrium critical point. Both quantities exhibit standard scaling forms,

$$C(t,s) = s^{-b} f_c(t/s), \quad R(t,s) = s^{-1-a} f_R(t/s) \tag{2.1}$$

where the scaling functions display a simple power-law behavior for large arguments, $y = t/s \gg 1$:

$$f_C(y) \sim y^{-\lambda_C/z}, \quad f_R(y) \sim y^{-\lambda_R/z} \, . \tag{2.2}$$

Here s and $t > s$ are two different times called waiting and observation times, and z is the dynamical exponent. The exponents a, b, λ_C, and λ_R are non-equilibrium exponents that govern the scaling properties of the two-time quantities. However, these studies also revealed some remarkable differences to the aging properties of systems relaxing towards an equilibrium steady state. Most notably, the exponents a and b, which for a system relaxing towards equilibrium are identical and related to a static critical exponent [3], can be different when detailed balance is broken. In some cases this difference can be understood through symmetry properties of the model, as for example for the contact process [13], in other cases no simple explication seems to exist.

In [33] a first step was undertaken in that direction where the non-equilibrium dynamical properties of some exactly solvable models were studied. This study indeed revealed the presence of the standard scaling forms (2.1) and (2.2) for correlation and response functions, and this for any values of the system parameters. Surprisingly, however, the scaling of the response function was found to strongly depend on whether or not some specific quantity was kept constant when perturbing the system. This is an interesting result, as it highlights the importance of conserved quantities during non-equilibrium relaxation.

The models studied in [33] are to some extend specialized in order to be exactly solvable. It is therefore of interest to understand which of the properties found in [33] are generic to systems with reversible reactions and which depend on special features of the studied models. Thus, in order to be soluble, it was assumed that the possible number of particles at every lattice site was unrestricted. In addition, as initial condition an uncorrelated Poisson distribution on each lattice site and for each particle species was assumed. In this chapter we study a system composed of two types of particles that undergo reversible reactions while diffusing on a lattice. We thereby only allow single site occupation and prepare the system by randomly distributing on the lattice a given number of particles of every type. During the relaxation process we study the two-time autocorrelation function as well as different two-time response functions.

2.2 The model and quantities

We consider one- and two-dimensional lattices on which particles of different types, called A and C, diffuse and interact. The data discussed in the following have mainly been obtained for systems of linear extend of $L = 10000$ in $d = 1$ and $L = 100$ in $d = 2$. We carefully checked that no finite-size effects show up in our quantities for these sizes. The diffusion of particles is realized by jumping to unoccupied nearest neighbor sites with rate D_a for an A particle and rate D_c for a C particle. The reaction scheme considered here is given by

$$A + A \rightleftarrows C \tag{2.3}$$

where two neighboring A particles coalesce with rate λ to form a C particle, whereas a C particle can decompose into two A particles with rate μ, provided that one of the neighboring sites is empty. In the simulations, we realize this scheme in the following way. We first select randomly a site and a direction. If the selected site is occupied by a C particle and if the neighboring site in the selected direction is empty, then the C particle is hopping in that direction with probability D_c or it is replaced by two neighboring A

particles with probability μ. If, on the other hand, an A particle sits on the selected site, the possible action will depend on whether the neighboring site in the selected direction is either empty or occupied by an A particle. In the first case we move the particle with probability D_a, in the second case the two A particles are replaced with probability λ by a C particle that we put on the initially selected site. For all other cases, no action takes place.

We prepare our system at time $t = 0$ "microcanonically" by distributing $N_A(0)$ A particles and $N_C(0)$ C particles randomly on our lattice. Preparing the system in this strict way is in fact very important as the quantity

$$K = N_A(0) + 2N_C(0) = N_A(t) + 2N_C(t) \tag{2.4}$$

is independent of time, making it a conserved quantity [26]. Here $N_A(t)$ and $N_C(t)$ are the numbers of A and C particles at time t. It follows from the presence of this conserved quantity that the steady-state particle densities $\rho_{A,S} = N_A(t \longrightarrow \infty)/N$ and $\rho_{C,S} = N_C(t \longrightarrow \infty)/N$, with $N = L$ in one dimension and $N = L \times L$ in two dimensions, depend on the initial preparation of the system.

In our simulations we monitor both the particle density as well as the two-time correlation function. Defining the time dependent occupation number $n_C^i(t)$ of site i as having the value 1 when that site is occupied at time t by a C particle and zero otherwise, the particle density of C particles is given by

$$\rho_C(t) = \sum_i n_C^i(t)/N \ . \tag{2.5}$$

Due to the conserved quantity K, the particle density of A particles is obtained directly through the relation

$$\rho_A(t) = K/N - 2\rho_C(t) \ . \tag{2.6}$$

Insights into the scaling properties during the relaxation process can be gained by studying the two-time connected autocorrelation function for C particles,

$$C_C(t,s) = \langle \frac{1}{N} \sum_i n_C^i(t) n_C^i(s) \rangle - \langle \rho_C(t) \rangle \langle \rho_C(s) \rangle \tag{2.7}$$

where the notation $\langle \cdots \rangle$ indicates averages over both initial conditions and realizations of the noise. In a similar way we define the two-time connected autocorrelation function for A particles, $C_A(t,s)$.

For the two-time response function different cases can be distinguished. Firstly, one can perturb the system in such a way that the quantity K does not change its value. This can be achieved, for example, by adding with rate r_K additional C particles to the system, while removing at the same time pairs of A particles. Obviously, we do not think that this is a realistic scenario that can be easily achieved in an experiment. Still, this scenario can be studied theoretically and might yield important insights into the role played by conserved quantities during relaxation processes. Secondly, one can also perturb the system such that K is no longer conserved. An obvious way of doing that is to inject additional particles of only one type (say, C particles) with some rate r. This will change the value of K, and the system will relax to a steady state whose particle densities differ from those of the unperturbed system.

In our simulations we have implemented the calculation of the responses in the following way. Initially, we prepare the system in a random state with fixed numbers of A and C particles, $N_A(0)$ and $N_C(0)$. This fixes the value of K at time $t = 0$. Calling $M_K(t,s)$ the response of the system to a perturbation that keeps K constant, we compute the difference between the average densities with and without perturbation:

$$M_K(t,s) = \langle \rho_C^p(t,s) \rangle - \langle \rho_C(t) \rangle \ . \tag{2.8}$$

Here $\rho_C^p(t,s)$ is the density of C particles at time t when the perturbation is removed at time $s < t$. Alternatively, we could define the response through the change in density of A particles. We carefully checked that our conclusions do not depend on our choice of the particle density. For that reason we will restrict ourselves in the next section to a discussion of the change in the density of C particles.

We proceed slightly differently for the calculation of the response to the injection of particles of a single type. We still prepare the system as before and inject additional particles until time s. After removing the perturbation we determine the particle densities $\rho_C^p(s,s)$ and $\rho_A^p(s,s)$ as well as the new value of K which will remain constant for the remainder of the simulation. Having determined K, we then do a second, unperturbed run, where we start with a disordered initial state with particle densities $\rho_C(0) = \rho_C^p(s,s)$ and $\rho_A(0) = \rho_A^p(s,s)$. The response to the injection of C particles is then calculated as the difference between the average densities with and without perturbation:

$$M_C(t,s) = \langle \rho_C^p(t,s) \rangle - \langle \rho_C(t) \rangle_K \, . \tag{2.9}$$

Here $\langle \rho_C(t) \rangle_K$ is the time-dependent particle density for the new value of K.

2.3 Simulation results

In the following we discuss the relaxation and aging processes that take place in our system. In our systematic study we considered diffusion rates D_a and D_c between 0.05 and 0.5, whereas the reaction rates λ and μ were varied between 0.1 and 0.7. We also considered a vast range of initial conditions in order to study the dependence of our results on the value of K. In addition, for a fixed value of K we typically considered three sets of initial conditions that differ by the number of A and C particles deposited on the lattice. Our main results for the time-dependent particle densities as well as for the two-time autocorrelation and response functions are summarized in the following subsections. These results are confronted with the analytical calculations obtained for the related model studied in [26, 33].

2.3.1 Particle densities

As discussed in many theoretical studies [19, 20, 21, 22, 23, 24, 25, 26, 27, 28, 29] and as verified in some experiments [30, 31, 32], systems with reversible chemical reactions are characterized by slow dynamics such that the particle densities approach their steady-state values with a power-law in time. More specifically, for the exactly solvable models without site restriction studied in [26, 33] one finds that particle densities asymptotically behave like

$$\rho(t) - \rho_S \sim t^{-d/2} \tag{2.10}$$

for any dimension d. Explicit expressions have been found for the stationary particle densities which reveal a dependence only on the value of the conserved quantity K and the ratio μ/λ of the reaction rates [26].

In Figure 2.1 we show the typical time evolution of the particle densities for our system. After an initial fast change, the particle densities rapidly evolve towards a regime where the approach to the steady state is algebraic. Figure 1 shows two cases with identical reaction and diffusion rates as well as with identical initial densities, the only difference being the dimensionality of the lattice. In both cases, the asymptotic

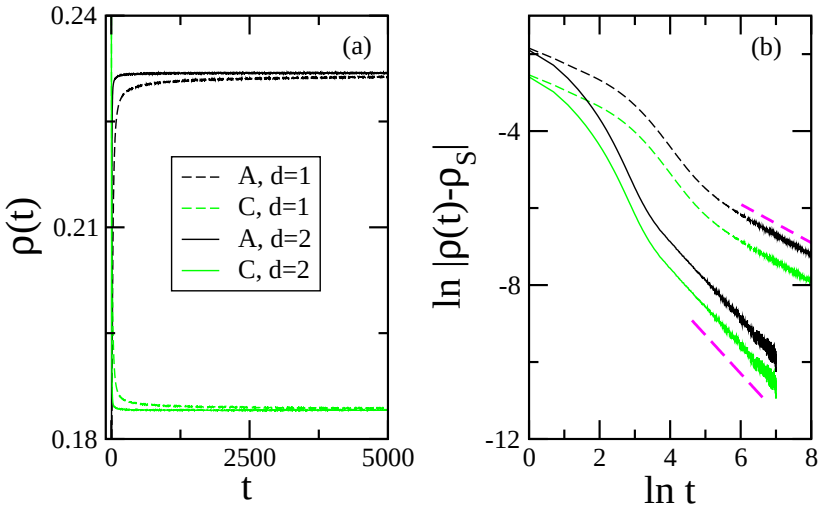

Figure 2.1: (a) Time evolution of the densities of A and C particles in one and two dimensions. The linear sizes of the systems are $L = 10000$ in $d = 1$ and $L = 100$ in $d = 2$, the common rates being $D_a = D_c = 0.1$ and $\mu = \lambda = 0.5$. Initially the systems consist only of C particles that randomly occupy 30% of the lattice sites. (b) The approach to stationarity is governed by a power law with exponent $d/2$, as indicated by the dashed straight segments. The data shown here result from averaging over 400000 independent runs [70].

particle densities are found to be identical and independent of whether a line or a square lattice is considered. Changing the diffusion and reaction rates in a systematic way, we find that the stationary particle densities remain unchanged when the values of the diffusion rates are changed. In fact, and this is in agreement with the expressions obtained for the exactly solvable case in [26], the steady-state values of the particle densities are completely fixed by the values of K and of the ratio μ/λ. Furthermore, see Figure 2.1b, the approach to stationarity is governed by the exponent $d/2$, as it is the case for the corresponding exactly solvable model [26].

2.3.2 Autocorrelation

The scaling of the two-time autocorrelation function in one and two dimensions is shown in Figure 2.2 for the C particles (similar results are obtained when looking at A particles). In all cases we obtain the standard aging scaling (2.1) and (2.2) with exponents $a = d/2$ and $\lambda_C/z = d/2$. Comparing the scaling functions for different values of the rates and different initial densities but fixed dimensionality, one observes that small differences, present for small values of t/s, rapidly vanish when t/s increases. Disregarding these finite time corrections, one recovers for a fixed value of d a common scaling function for all rates and initial states.

It is tempting to compare our scaling functions with those obtained when site restriction is not imposed. As shown in [33] the scaling function is then given in leading order by

$$C_C(t,s) = As^{-d/2}\,(t/s+1)^{-d/2} \tag{2.11}$$

where the amplitude A depends on reaction rates as well as on initial conditions and the steady-state particle

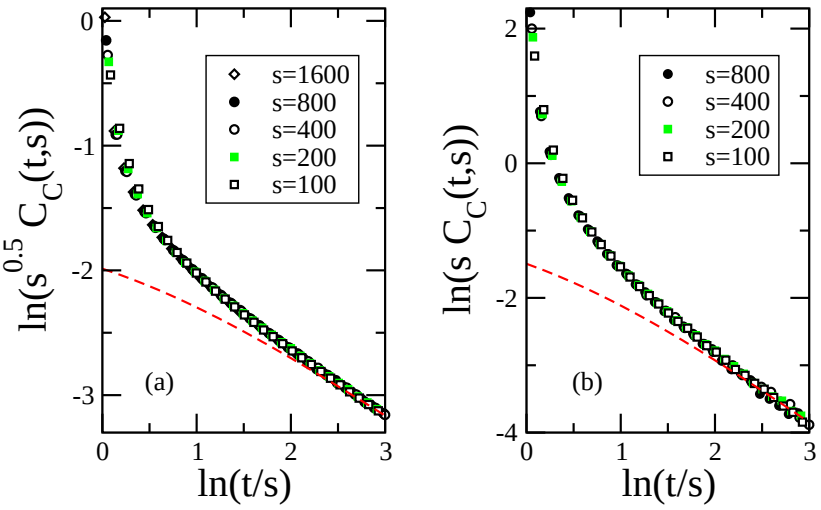

Figure 2.2: The scaling of the autocorrelation function $C_C(t,s)$ for C particles in (a) $d=1$ and (b) $d=2$ dimensions. The diffusion rates are $D_a = D_c = 0.05$, whereas the reaction rates are $\mu = \lambda = 0.5$, the initial state being composed only of C particles that randomly occupy 30% of the lattice sites. The red dashed lines show the asymptotic scaling functions obtained for the exactly solvable model studied in [33], see equation (2.11). The data result from averaging over at least 30000 independent runs [70].

densities. One therefore obtains for both models the same values of the exponents a and λ_C/z. The expression (2.11) however only slowly approaches the scaling function obtained in the present study, as shown in Figure 2.2. In fact, equation (2.11) only gives the asymptotic scaling function, valid in the limit $t/s \gg 1$. Subleading correction terms, the most important being proportional to $s^{-d/2}t^{-d/2}$ [33], can not be neglected on the time scale of our simulations.

2.3.3 Response functions

Our main motivation for the present study was the surprising observation in [33] that the scaling function of the autoresponse strongly depends on how the system is perturbed. As already mentioned in the introduction, one obtains for the exactly solvable models studied in [33] expressions for the responses that depend on whether or not certain quantities are conserved during the perturbation. Our main aim in the following is to verify whether this is a generic behavior or whether this follows from the special properties of these exactly solvable models.

Before discussing our data we remark that we are in fact computing time integrated response functions. Indeed, our responses result from summing up all the effects due to the perturbation of the system during a time interval of length s. As a result our integrated responses, see equations (2.8) and (2.9), are related to the response functions in the usual way [3] through an integration in time:

$$M(t,s) = \int_0^s du R(t,u) \tag{2.12}$$

which yields under the assumption of simple aging for the response, see equation (2.1), the following scaling form for the integrated response in leading order:

$$M(t,s) = s^{-a} f_M(t/s) \tag{2.13}$$

with $f_M(y) \sim y^{-\lambda_R/z}$ for $y \gg 1$.

We start by showing in Figure 2.3 the time-integrated response (2.8) where the injection of a C particle is accompanied by the removal of two A particles such that K remains constant. We recover a simple aging behavior, with exponents $a = d/2$ and $\lambda_R/z = d/2$, similar to what is obtained for this response when studying the model without site restriction. [1] This scaling behavior of the integrated response is therefore similar to that observed in many systems relaxing toward their steady state while being characterized by a single time-dependent length scale that increases algebraically with time [3].

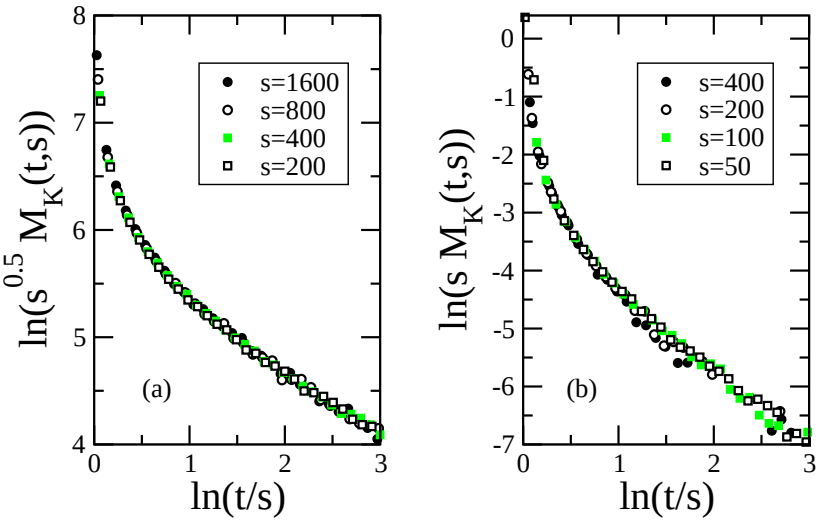

Figure 2.3: The scaling of the time integrated response $M_K(t,s)$, see equation (2.8), in (a) $d = 1$ and (b) $d = 2$ dimensions. The diffusion rates are $D_a = D_c = 0.5$, whereas the reaction rates are $\mu = \lambda = 0.5$. The rates for injecting C particles and removing pairs of A particles are $r_K = 0.01$ in $d = 1$ and $r_K = 0.05$ in $d = 2$. Initially 14% of the sites are occupied by A particles, whereas C particles are randomly deposited on 23% of the sites. The data shown here have been obtained after averaging over typically one million independent runs [70].

The scaling of $M_K(t,s)$ has to be contrasted with the scaling of $M_C(t,s)$ where the perturbation consists in injecting additional C particles. As shown in Figure **??** $M_C(t,s)$ is *independent* of the waiting time and, after some initial faster decay, rapidly exhibits a power-law behavior,

$$M_C(t,s) \sim t^{-d/2} , \tag{2.14}$$

as indicated by the dashed lines in the figure. Comparing this to the results obtained for the model without site restriction, we notice here a difference in behavior. Indeed, for the model studied in [33] the time

[1] Note that in [33] it is also the time integrated response that is investigated. This is not correctly stated in that paper.

integrated response to the injections of only C particles is the sum of two terms, one proportional to $t^{-d/2}$ and one proportional to $(t-s)^{-d/2}$, see equation (41) in [33]. This difference can be understood in the following way. In the model studied in [33] a newly injected C particle can immediately decompose into two A particles, as there is no restriction on the number of particles at any given site. In our model, however, a newly injected C particle needs to have an empty neighboring site in order to decompose into two A particles. It is immediately clear that the injection of additional particles yields a reduction of the number of unoccupied sites. Consequently, the decomposition of C particles is retarded as more and more diffusion steps are needed in order to bring the C particles close to empty sites. Therefore, it is the hopping of particles that dominates and that gives rise to the waiting time independent response.

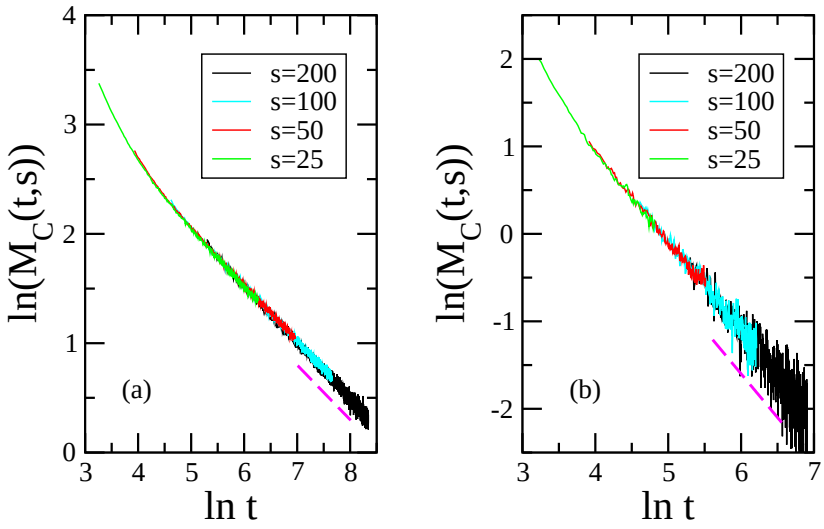

Figure 2.4: The scaling of the time integrated response $M_C(t,s)$, see equation (2.9), in (a) $d=1$ and (b) $d=2$ dimensions. The diffusion rates are $D_a = D_c = 0.05$, whereas the reaction rates are $\mu = \lambda = 0.5$. The injection rates of C particles is $r = 0.0001$ in both cases. Initially 14% of the sites are occupied by A particles, whereas C particles are randomly deposited on 23% of the sites. The data shown here have been obtained after averaging over typically 250000 independent runs. Note that the response is waiting time independent and that the decay is algebraic for large times, with exponent $d/2$, as indicated by the dashed lines [70].

Even so the scaling behavior for this response is different in our site restricted model, the main conclusion drawn in [33] is still valid: the scaling properties of responses change when otherwise conserved quantities are changed due to the perturbation. This effect is therefore not only restricted to the model discussed in [33], but seems to be a generic property of aging processes that take place in systems with conserved quantities.

2.4 Conclusion

We have discussed in this section the non-equilibrium relaxation in a reaction-diffusion model characterized by reversible reactions. In contrast to systems with irreversible reactions, systems with reversible reactions

generically display slow dynamics and simple aging, independent of the values of the reaction and diffusion probabilities. Comparing our results with those obtained previously for a model with site restriction, we note that the approach to stationarity is governed by the same exponents in both cases, as revealed through the study of the time-dependent particle densities or the two-time autocorrelation. The same conclusion can be drawn when looking at the response to a perturbation that conserves the quantity K; see equation (2.4). It also remains true that the scaling properties of responses are found to depend on whether the perturbation conserves the value of K or not. Of course, other responses need to be studied in the future in order to further probe the universality of this statement. All this points to a high degree of universality, suggesting that systems with reversible reactions are excellent candidates for use in the experimental study of aging properties in reaction-diffusion systems. No fine-tuning of the system parameters is needed in order to have slow dynamics, as demonstrated in experimental studies of excited-state proton transfer reactions [27,29]. As our theoretical findings point to a high robustness of the reported results, a future experimental verification of our predictions can be envisaged. Our present study can readily be generalized to other reaction-diffusion systems. In this chapter we considered one of the simplest reversible reaction schemes where two A particles coalesce to form a C particle which then can again decompose into two A particles. Other reaction schemes that can be studied are given by

$$A + B \rightleftarrows C \tag{2.15}$$

and by

$$A + B \rightleftarrows C + D. \tag{2.16}$$

The second reaction scheme is of particular interest, as it not only is realized readily in experiments (a well known example is provided by ethanoic acid dissolved in water, that forms ethanoate and hydronium ions following the reactions $CH_3CO_2H + H_2O \rightleftarrows CH_3CO_2^- + H_3O^+$), but also has the interesting property that three different quantities are conserved [30]. It would be interesting to study the different responses in these systems in order to see how the scaling properties change when the conservation of some or all quantities is destroyed by the perturbation.

Chapter 3

Aging processes in systems with anomalous slow dynamics

N. Afzal and M. Pleimling, Phys. Rev. E **87**, 012114 (2013).

Recently, different numerical studies of coarsening in disordered systems have shown the existence of a crossover from an initial, transient, power-law domain growth to a slower, presumably logarithmic, growth. However, due to the very slow dynamics and the long lasting transient regime, one is usually not able to fully enter the asymptotic regime when investigating the relaxation of these systems toward equilibrium. We study two simple driven systems, the one-dimensional *ABC* model and a related domain model with simplified dynamics, that are known to exhibit anomalous slow relaxation where the asymptotic logarithmic growth regime is readily accessible. Studying two-times correlation and response functions, we focus on aging processes and dynamical scaling during logarithmic growth. Using the time-dependent growth length as the scaling variable, a simple aging picture emerges that is expected to also prevail in the asymptotic regime of disordered ferromagnets and spin glasses. The results discussed in the following are the subject of my paper [76].

3.1 Models and quantities

In the *ABC* model particles of three different species live on a one-dimensional ring [48]. Every lattice site is occupied by exactly one particle, which can swap places with its left and right neighbors. In the symmetric case, where all exchanges happen with the same rate, every particle undergoes a random walk, and nothing interesting takes place. However, this changes dramatically as soon as one introduces a bias which makes the particles diffuse asymmetrically around the ring. This is achieved by randomly selecting a

pair of neighboring sites and updating them using the following rates:

$$\begin{aligned} AB &\underset{1}{\overset{q}{\rightleftarrows}} BA \\ BC &\underset{1}{\overset{q}{\rightleftarrows}} CB \\ CA &\underset{1}{\overset{q}{\rightleftarrows}} AC \end{aligned} \tag{3.1}$$

with $q < 1$. As a result of these rules, phase separation takes place in such a way that the ordered domains arrange themselves in repetitions of the sequence *ABC*, where *A* indicates a domain of *A* particles, followed by a domain of *B* particles, which itself is followed by a *C* domain. Once this arrangement has been achieved, the domains coarsen whereby the typical domain size increases logarithmically with time.

Obviously these exchanges keep constant the total number of particles of each species. We consider in our study only lattice sizes divisible by three and initially populate one third of the lattice sites by particles of each species. In that case detailed balance is fulfilled and the system evolves toward an equilibrium steady state [48].

In the domain model one focuses on the later stages of the coarsening process where well-defined, compact domains have already formed. One then defines a simplified dynamics where only events are taken into account that change the sizes of two neighboring domains of the same species. For example, consider the case where two such *A* domains are selected, called A_l and A_r, that are separated by one *B* and one *C* domain, yielding the sequence $\cdots A_l BCA_r \cdots$. Calling a_l respectively a_r the domain size of the domain A_l respectively A_r, these domain sizes are then modified in one of the following two ways [49]:

$$\begin{aligned} a_l \longrightarrow a_l - 1 \ , \ a_r = a_r + 1 \quad \text{with rate } q^b \\ a_l \longrightarrow a_l + 1 \ , \ a_r = a_r - 1 \quad \text{with rate } q^c \end{aligned}$$

where *b* respectively *c* are the number of sites of the *B* respectively *C* domain separating our two *A* domains. These rates follow from the observation that in order to go from one domain to the other an *A* particle has to cross one of the two intermediate domains in the 'wrong' direction.

Two-times quantities are well suited to study relaxation processes far from equilibrium [5]. We here briefly recall the expected behavior of such quantities, without entering into the details on how these quantities are computed for our driven diffusive systems. This will be done in the following sections when we discuss our numerical results.

The two-times quantities usually at the center of aging studies are the autocorrelation function $C(t,s)$ and the autoresponse function $R(t,s)$. The autocorrelation function measures the extend to which configurations taken at two different times s and $t > s$ are correlated. Here s is the waiting time, whereas t is called the observation time. The autoresponse function, on the other hand, allows us to investigate how the system reacts during the relaxation process to a instantaneous perturbation (as for many other studies, we will focus below on the time integrated response to a longer lasting perturbation which is much easier to measure). In the aging regime, where the observation and waiting times are large compared to any microscopic time scale, the single growth length L dominates the properties of the system, so that the different quantities should depend on time only through this length L. Thus one expects the following (very general) scaling

forms, using standard notation [5]:

$$C(t,s) = (L(s))^{-b} f_C\left(\frac{L(t)}{L(s)}\right) \tag{3.2}$$

$$R(t,s) = (L(s))^{-1-a} f_R\left(\frac{L(t)}{L(s)}\right) \tag{3.3}$$

with the scaling functions $f_C(y)$ and $f_R(y)$ and the non-equilibrium exponents a and b. In systems undergoing coarsening one usually has $b = 0$ and $a \neq 0$, but this can be different in other situations, as for example during non-equilibrium relaxation at a critical point [69]. In cases with an algebraic growth law $L(t) \sim t^{1/z}$, as observed in critical systems or coarsening systems without disorder, one usually uses t/s as scaling variable and as an example refer to section 2.3.2. However, for more complicated cases with subleading contributions to the growth and/or crossover between an initial algebraic growth and the true asymptotic behavior, this approach is too simplistic and $L(t)/L(s)$ has to be used as variable in order to achieve the expected scaling [41, 45].

3.2 Aging in the *ABC* model

In our simulations of the original *ABC* model we focus on the early time regime where coarsening slowly sets in. We thereby always prepare the system in a disordered initial state with every species occupying one third of the lattice sites chosen at random. The data presented below have been obtained for rings with $N = 9000$ sites. This is large enough so that no finite size effects show up for the times accessed in our simulations, as we checked by making additional runs for other system sizes. We define one time step as N proposed updates. For every proposed update we select a pair of neighboring sites at random and then exchange them with the rates given in (3.1).

3.2.1 Domain growth

We start by having a look at the average domain size. Fig. 3.1 shows $L(t)$ for a large range of q values. We note that in all cases an initial regime is observed during which domains are formed and arranged in the correct sequence, so that a C domain follows a B domain that follows an A domain. This initial regime lasts longer for larger values of q as it gets increasingly difficult to form these initial domains the closer q gets to 1.

Once these initial domains are formed, they then coarsen, and the system size increases logarithmically with time: $L(t) \sim \ln t$. Obviously, this is a very slow process and even after 10^8 time steps the average domain size does not reach twenty lattice spacings. This coarsening proceeds faster for larger values of q. Indeed, the slopes in the log-linear plot decrease when decreasing q. Thus, in the interval between $t = 10^6$ and $t = 10^8$ we obtain that the slope continuously decreases from 1.05 for $q = 0.9$ to 0.86 for $q = 0.2$. Whereas at short times the domain size is the largest for the smallest q value, we expect the order to be reversed for very long times, due to the difference in slopes. In fact, indications of this are already seen in Fig. 3.1, see the two curves for $q = 0.2$ and $q = 0.3$ that start to be below some of the curves obtained for larger q values.

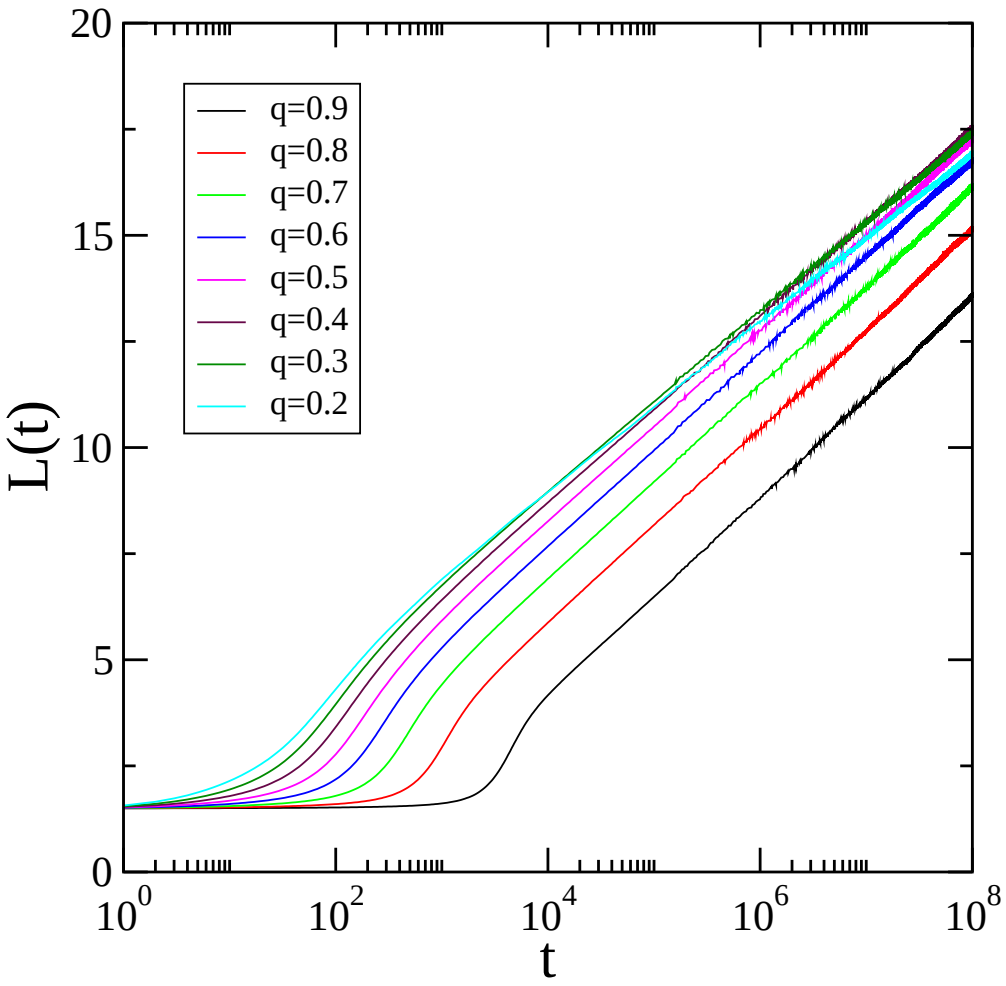

Figure 3.1: (Color online) Time-dependent average domain size for the *ABC* model with various values of the rate q. After some initial regime, that lasts longer the larger the value of q, logarithmic growth sets in. The slopes in the log-linear plot increase with q. The data result from averaging over 600 independent runs. (Reprinted figure with permission from [76]. Copyright (2013) by the American Physical Society).

A closer inspection of the curves in Fig. 3.1 reveals that their slopes change slightly with time. Even after $t = 10^8$ time steps we are not yet completely inside the asymptotic regime where corrections to the logarithmic growth law should be completely absent.

3.2.2 Autocorrelation

As mentioned in the introduction, valuable insights into relaxation far from equilibrium can be gained through the study of two-times quantities. In this subsection we discuss the autocorrelation $C(t,s)$. For our three species system we characterize lattice site i by a time-dependent Potts variable $p_i(t)$(alternatively

we could use a species dependent occupation number [70, 71] which has been used in chapter 6) that can take on the three different values 0, 1, or 2, depending on whether at time t the site is occupied by an A, B, or C particle. The autocorrelation function $C(t,s)$ is then defined as

$$C(t,s) = \left\langle \frac{1}{N}\sum_{i=1}^{N} \delta_{p_i(t),p_i(s)} \right\rangle - \frac{1}{3} \tag{3.4}$$

where $\delta_{\alpha,\beta}$ is the Kronecker delta. In that equation $\langle \cdots \rangle$ indicates an average over both initial conditions and noise as realized through different random number sequences. We subtract from this average the value 1/3 that one has for two completely uncorrelated configurations, thus making sure that $C(t,s)$ approaches zero when t gets very large.

In our simulations we averaged over a large number of realizations, ranging from 600 for the longest waiting times to 20000 for the shortest waiting times. In all cases we let the system evolve for $t = 40\ s$ time steps where s is the waiting time.

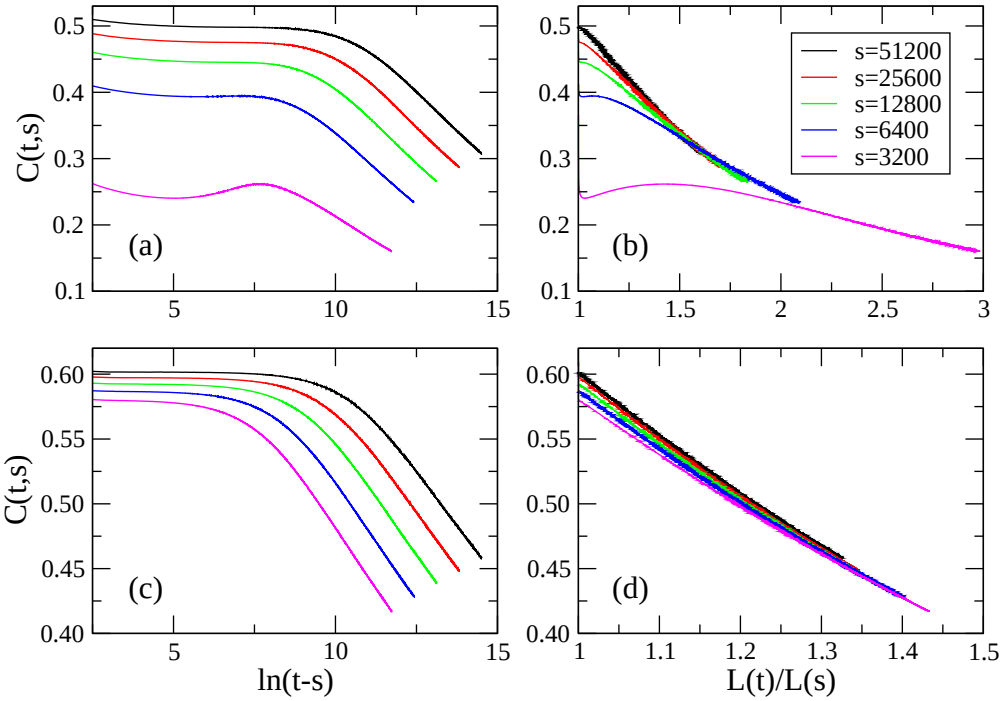

Figure 3.2: (Color online) Autocorrelation function for the *ABC* model with (a,b) $q = 0.9$ and (c,d) $q = 0.3$. For every waiting time s we compute the autocorrelation function for up to $t = 40\ s$ time steps. Plotting the autocorrelation against the scaling variable $L(t)/L(s)$, see (b) and (d), yields indications for the onset of dynamical scaling for the longest waiting times. The data result from averaging over at least 600 independent run (Reprinted figure with permission from [76]. Copyright (2013) by the American Physical Society.)

The data shown in Fig. 3.2 for $q = 0.9$ and $q = 0.3$ are representative for all studied values of q. Comparing data for different waiting times reveal the expected physical aging where the two-times quantity is not simply

a function of the time difference, see Fig. 3.2a and 3.2b. For $q = 0.9$ the behavior for the shortest waiting time shown in Fig. 3.2a clearly differs from that observed for the larger waiting times. In fact, inspection of Fig. 3.1 reveals that $s = 3200$ lies in the time regime where the initial domains are forming and where coarsening starts to set in. As a result correlations dramatically change in the system, which is revealed by the non-monotonous behavior of the autocorrelation function.

In Fig. 3.2b and 3.2d we test dynamical scaling by plotting the data as a function of $L(t)/L(s)$. Clear deviations are observed for the smaller waiting times, but these deviations get less and less important the larger s gets, yielding for $q = 0.3$ already a good data collapse for the largest waiting times. All this indicates that for very large s we start to be in the aging scaling regime. In agreement with Fig. 3.1 the scaling regime is accessed more rapidly for the smaller q values. We also note that even for $t/s = 40$, the ratio of the corresponding lengths $L(t)/L(s)$ remains rather small. Obviously, the regime $L(t)/L(s) \gg 1$ remains out of reach in systems displaying logarithmic growth.

3.3 Aging in the domain model

It follows from the discussion in the previous section that it is extremely difficult to fully enter the asymptotic growth regime for the *ABC* model. We therefore focus in the following on the domain model with simplified dynamics that captures the essential properties of the *ABC* model deep inside the coarsening regime while speeding up the dynamics [49].

For the domain model we consider systems with $N = 27000$ sites, thereby checking carefully that no finite-size effects affect our data for the times accessed in our simulations. As the dynamics assumes the existence of domains that coarsen, we prepare our system in an initial state where we have 3000 sequences of *ABC* domains, with every domain extending over three lattice sites. We then start the system with the chosen value of q. During the simulations smaller domains tend to disappear as larger domains keep growing. If, say, an *A* domain vanishes in the original *ABC* model, this yields a sequence *ABCBCA*, which rapidly evolves into a sequence *ABCA* as for two neighboring sites *CB* is replaced by *BC* with rate 1. The resulting *B* respectively *C* domains have then sizes that are identical to the sums of the sizes of the two *B* respectively *C* domains at the moment of the dismissal of the *A* domain. In the domain model this merging is done immediately whenever a domain vanishes [49]. For simplicity we increase in our simulations time t by one unit when the number of proposed updates is equal to the number of domains that are in the system at time t.

3.3.1 Domain growth

In Fig. 3.3 we verify that we are indeed deep inside the logarithmic growth regime for all studied values of q. As already observed in [49], the logarithmic growth sets in very rapidly when using the simplified dynamics. We note that the growth proceeds faster for larger values of q. This is of course in agreement with our observation in Fig. 3.1 that for the system with the full dynamics the prefactor in the equation (which corresponds to the slope in the log-linear plot)

$$L(t) = \gamma \ln t \tag{3.5}$$

is decreasing when q decreases. In [49] it has been proposed that the length should grow as

$$L(t) = p \ln t / |\ln q| \tag{3.6}$$

for the domain model. We indeed obtain consistently a value of $p \approx 2.0$ for all q values. This value is slightly smaller than the value of 2.6 found in [49]. This difference should be due to the different definitions of a time step in both studies.

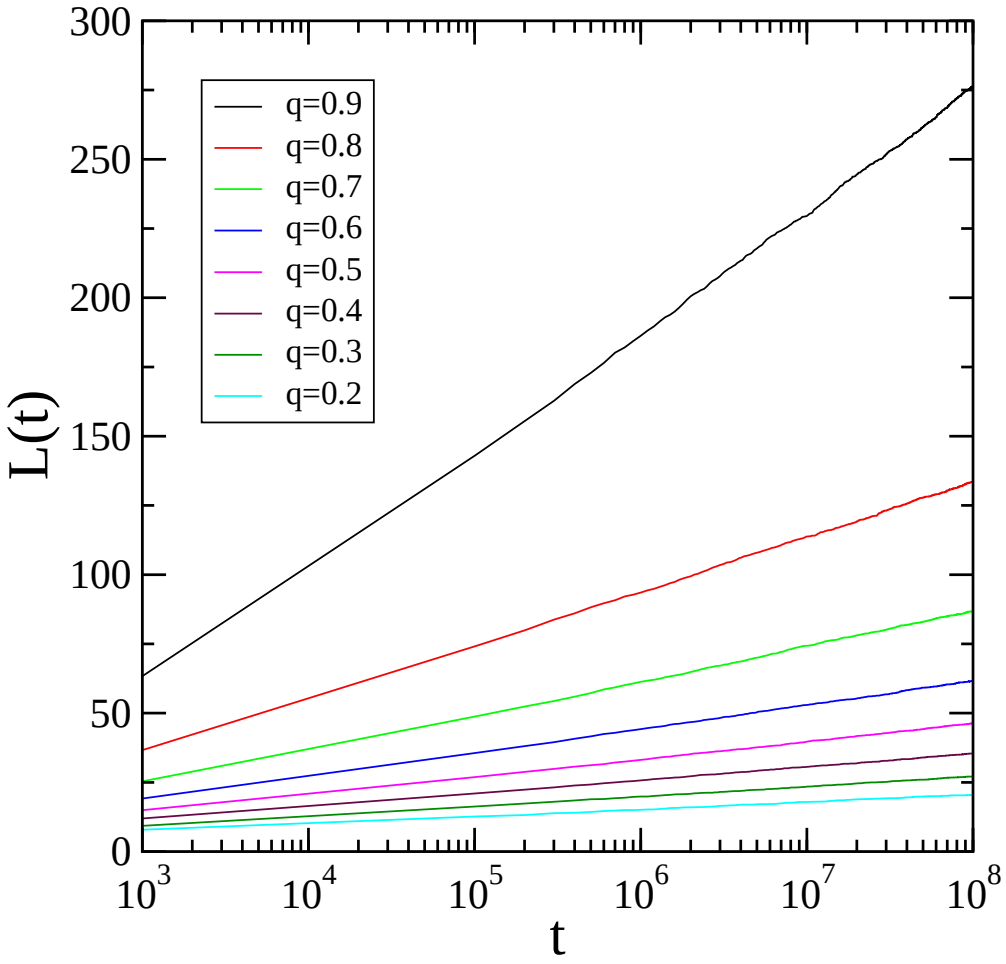

Figure 3.3: (Color online) Time-dependent average domain size for the domain model for various values of the rate q. Logarithmic growth is observed where the slopes in the log-linear plot increase with q. The data result from averaging over at least 100 independent runs. (Reprinted figure with permission from [76]. Copyright (2013) by the American Physical Society.)

3.3.2 Autocorrelation

For the autocorrelation we proceed as for the original *ABC* model. Using Eq. (3.4) we compute $C(t,s)$ for various waiting times s and plot the data as a function of $L(t)/L(s)$. The result is shown in Fig. 3.4 for two

values of q. In all cases we achieve perfect data collapse when plotting the data in this way, see Fig. 3.4b and 3.4d. This vindicates the simple aging scaling form (3.2) also for systems with anomalous slow dynamics. As for the autocorrelation only configurations at different stages of the time evolution are compared, we expect to encounter for that quantity the same scaling in other systems characterized by a single length scale that grows logarithmically with time, including disordered ferromagnets and spin glasses in their asymptotic regime.

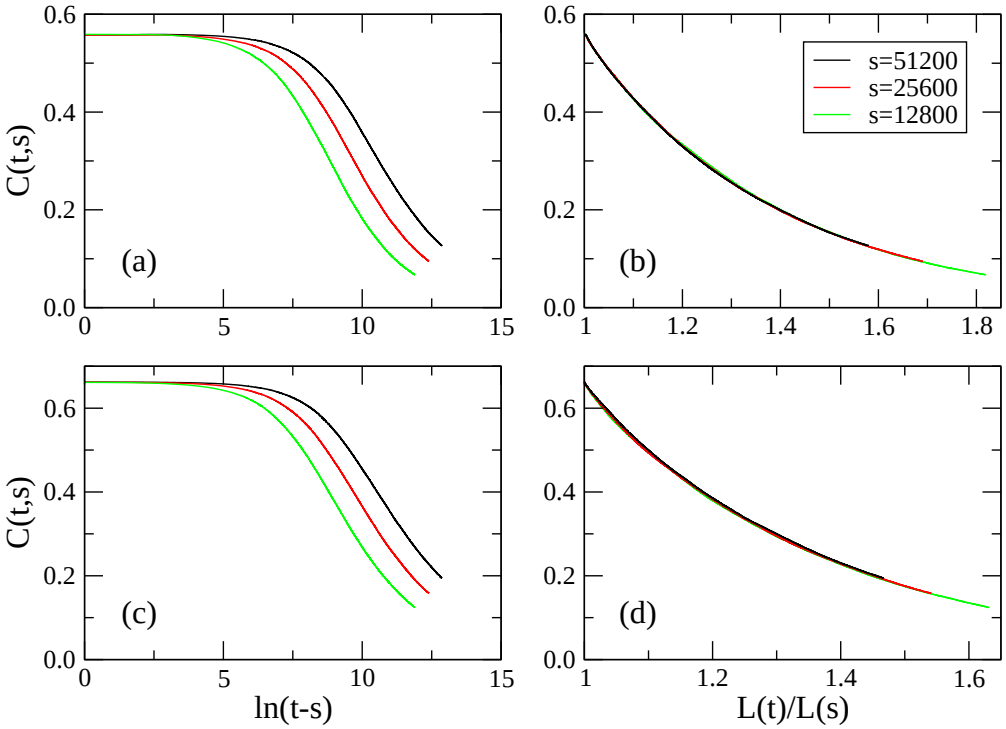

Figure 3.4: (Color online) Autocorrelation function for the *ABC* model with (a,b) $q = 0.9$ and (c,d) $q = 0.7$. Plotting the autocorrelation against the scaling variable $L(t)/L(s)$, see (b) and (d), yields a perfect data collapse. The data result from averaging over 50000 independent runs. (Reprinted figure with permission from [76]. Copyright (2013) by the American Physical Society.)

3.3.3 Different responses

Changes in the relaxation process due to external perturbations are best captured through the study of two-times response functions. For spin systems, as for example ferromagnets or spin glasses, one of the often used protocols, both in theoretical [5] and experimental [72, 73] studies, consists of applying a (random) magnetic field at the moment of a temperature quench. This field is then removed after the waiting time and the relaxation of the system is monitored.

For the domain model we employ a similar scheme for the computation of the response. Preparing the system in the same way as for the calculation of the autocorrelation, we let the system initially evolve with a given exchange rate $q = q_i$. At time $t = s$ we change the exchange rate to its final value $q = q_f$ that is

kept constant until the end of the run. Due to the initial value of q, the average domain size at the waiting time s differs from the typical domain size encountered in a system that evolves at the fixed value $q = q_f$. Consequently we choose as our observable the difference in system sizes between the perturbed system, where we switch from q_i to q_f, and the unperturbed system, where $q = q_f$ for the whole run:

$$M(t,s) = |L_p(t,s) - L(t)| \ . \tag{3.7}$$

Here $L_p(t,s)$ is the actual domain size of the perturbed system, whereas $L(t)$ is the average domain size without a perturbation. As in the long time limit $L_p(t,s) \longrightarrow L(t)$, this quantity vanishes for long observation times. The absolute values are used in Eq. (3.7) as we can have either that $L_p(s,s) > L(s)$ or that $L_p(s,s) < L(s)$, depending on whether $q_i > q_f$ or $q_i < q_f$. In our study we considered multiple cases with various combinations of q_i and q_f. In doing so, we restricted ourselves to values of $q_i \geq 0.7$ as well as to not too large changes in q, such that $\left|q_i - q_f\right| \leq 0.1$.

Let us mention that the response $M(t,s)$ is a time integrated global response as (a) it sums up all the changes that accumulate over the time during which the perturbation is switched on and (b) it gives the global response of the system to a perturbation that affects all parts of the system in the same way. As such it is related in a rather complicated way to the response $R(t,s)$ discussed previously, which is the local response to an instantaneous perturbation. It is not clear *a priori* whether a scaling form like that given in (3.3) remains valid for the more complicated response studied here.

Let us start with a discussion of the time evolution of the domain length $L_p(t,s)$ after changing the value of the rate q. As we see in Fig. 3.5 for two cases with $q_f = 0.8$, the behavior of $L_p(t,s)$ is remarkably different depending on whether q is decreased or increased. When decreasing q after the waiting time, see the upper colored curves in Fig. 3.5, the domain size is at the moment of the change much larger than the average domain size in the unperturbed system that evolves at the constant value $q = q_f$. As a result domains grow extremely slowly after the change and it takes a very long time for $L_p(t,s)$ to approach the unperturbed curve $L(t)$. In fact, a closer inspection reveals that the difference between the curves $L_p(t,s) - L(s)$ varies logarithmically with time, $L_p(t,s) - L(s) = \mu \ln t + \nu$, where μ is found to be independent of the waiting time s, see Fig. 3.6a and 3.6c for two examples. The situation is very different for cases where q is increased, see the lower colored curves in Fig. 3.5. In these cases accelerated growth sets in and the perturbed curve approaches the unperturbed curve very rapidly. Indeed, after an initial short time regime, the difference between the two lengths vanishes in an approximately algebraic way, with an effective exponent whose value is between 1.7 and 1.9, depending on the waiting time s.

We investigate the possible scaling behavior of the response $M(t,s)$, see Eq. (3.7), in Figures 3.6 and 3.7. The case $q_i > q_f$ is illustrated in Fig. 3.6 by two examples: a change from $q_i = 0.9$ to $q_f = 0.85$ as well as a change from $q_i = 0.8$ to $q_f = 0.7$. We first remark, see Fig. 3.6a and 3.6c, that $M(t,s)$ indeed varies linearly with $\ln t$, independent of the waiting time s. This observation already suggests that the time integrated response also exhibits a scaling behavior where the time dependence is completely captured through the dynamic correlation length $L(t)$:

$$M(t,s) = (L(s))^{-\alpha} \, f_M\left(\frac{L(t)}{L(s)}\right) \tag{3.8}$$

with the scaling variable $\frac{L(t)}{L(s)}$. As shown in Fig. 3.6b and 3.6d this indeed yields a data collapse of the time integrated response, with an exponent α that depends on the rates q_i and q_f. It therefore follows that for the case $q_i > q_f$ the response shows a standard aging scaling, similar to the autocorrelation, provided that the time-dependent length $L(t)$ is used.

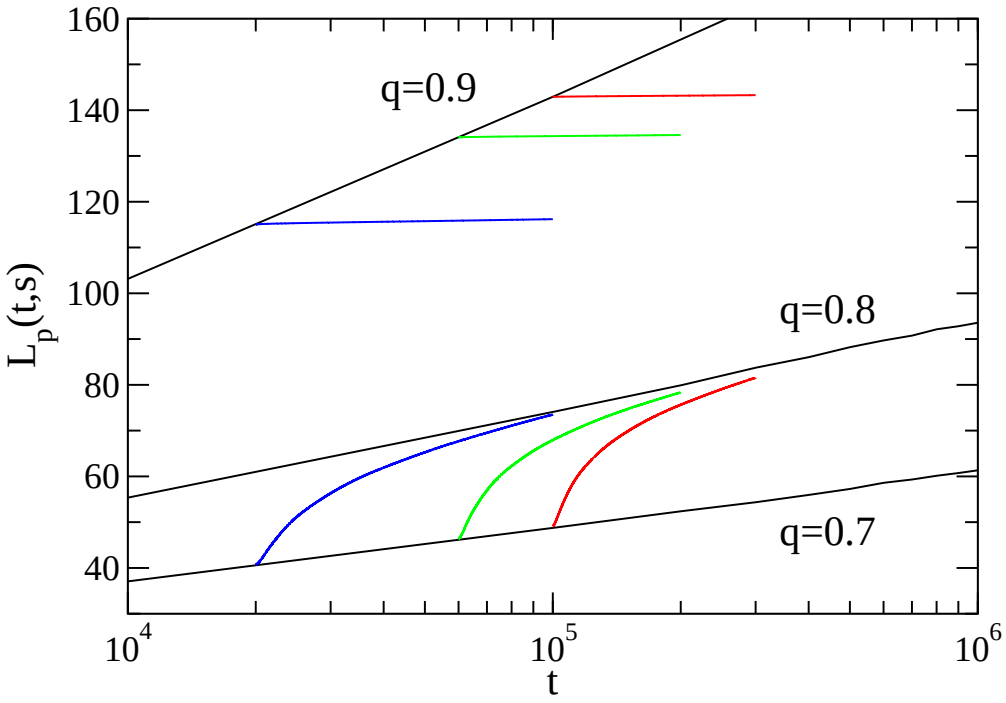

Figure 3.5: (Color online) Time evolution of the average growth length when changing after the waiting time s the value of the rate q from 0.9 to 0.8 (upper colored lines) or from 0.7 to 0.8 (lower colored lines). The different waiting times are s=20000 (blue lines), s=60000 (green lines), and $s = 100000$ (red lines). (Reprinted figure with permission from [76]. Copyright (2013) by the American Physical Society.)

This is completely different for the case $q_i < q_f$, see Fig. 3.7. As already discussed, the domains at the moment of the change of the rate are smaller than those encountered in the unperturbed system with the same number of time steps, and the larger rate q_f yields a much higher probability for a particle to jump from one domain to another. Consequently, the domain growth proceeds very fast. As shown in Fig. 3.7 for the case with $q_i = 0.8$ and $q_f = 0.9$, no good data collapse is observed when using as scaling variable $L(t)/L(s)$. In fact, see the inset, the curves for different waiting times always cross, which of course renders a data collapse impossible. Clearly, when the approach of $L_p(t,s)$ to $L(t)$ is faster than logarithmic, then a scaling behavior like that observed for $q_i > q_f$ can not be expected. As mentioned before, $L(t) - L_p(t,s)$ displays in a certain regime an effective algebraic dependence on t. This might suggest that we could choose as scaling variable t/s. However, as this effective exponent displays a dependence on the waiting time, this also does not yield a data collapse.

3.4 Discussion and conclusion

In recent years numerous studies have yielded a rather good understanding of aging processes governed by an algebraic growth of the unique relevant length scale. This is especially true for systems with compet-

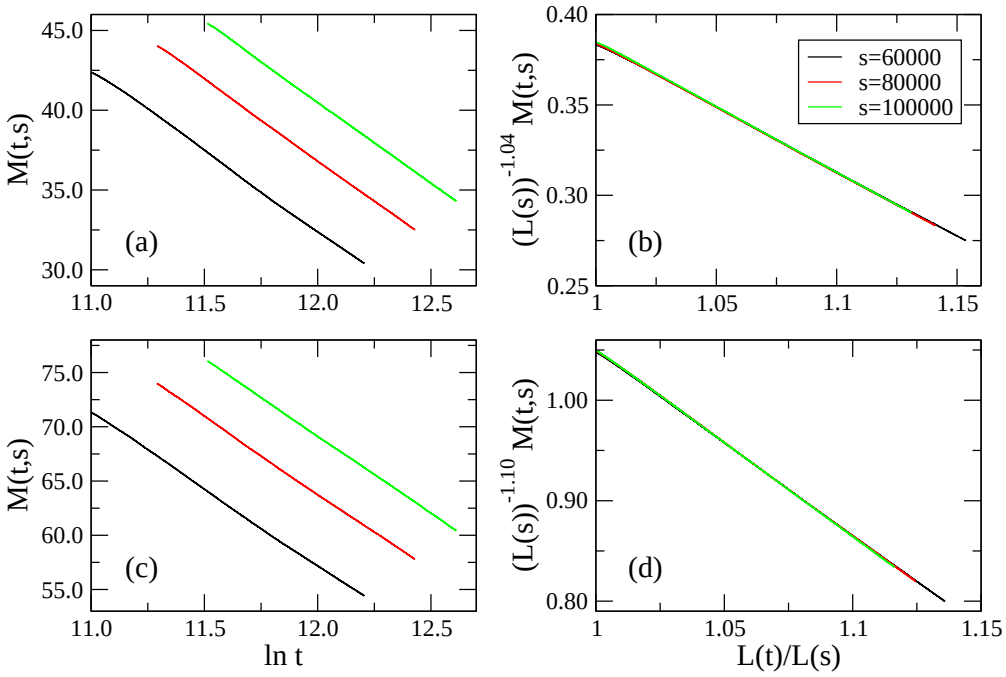

Figure 3.6: (Color online) Response function for the *ABC* model where at the waiting time s the exchange rates are decreased from some initial value q_i to the final value q_f: (a,b) $q_i = 0.9$ and $q_f = 0.85$, (c,d) $q_i = 0.8$ and $q_f = 0.7$. Plotting the response function against the scaling variable $L(t)/L(s)$, see (b) and (d), yields a perfect data collapse. The data result from averaging over 10000 independent runs. (Reprinted figure with permission from [76]. Copyright (2013) by the American Physical Society.)

ing ground states where phase coarsening dominates the out of equilibrium behavior in the ordered phase, thereby yielding a typical domain size that increases as a power-law of time. Perfect magnets, as embodied by the Ising or Potts models, are well studied examples. However, as soon as one adds disorder and/or frustration effects, the dynamics slows down. A series of recent numerical studies [41, 43, 44, 45] have confirmed the existence of a crossover from an initial power-law like regime to an asymptotic regime where the relevant length scale increases much slower with time. Even though it is expected that this long time regime is characterized by logarithmic growth, none of the studies in which the time evolution of the system was followed where able to fully enter this asymptotic regime. Consequently, most of the non-equilibrium properties in such a regime have not yet been explored.

Motivated by the absence of systematic studies of aging in system with logarithmic growth, we propose to follow a different route and to focus on model systems for which it is possible to access the logarithmic regime. Even though these models are not related to disordered magnetic systems, their study should allow us to gain a better understanding of the more universal properties encountered in this regime.

In this chapter we have studied the *ABC* model and a related domain model with a simplified dynamics. The *ABC* model allows us to study the crossover from an early time regime to the logarithmic regime. The domain model, on the other hand, very rapidly displays a logarithmic growth of the domains. Therefore,

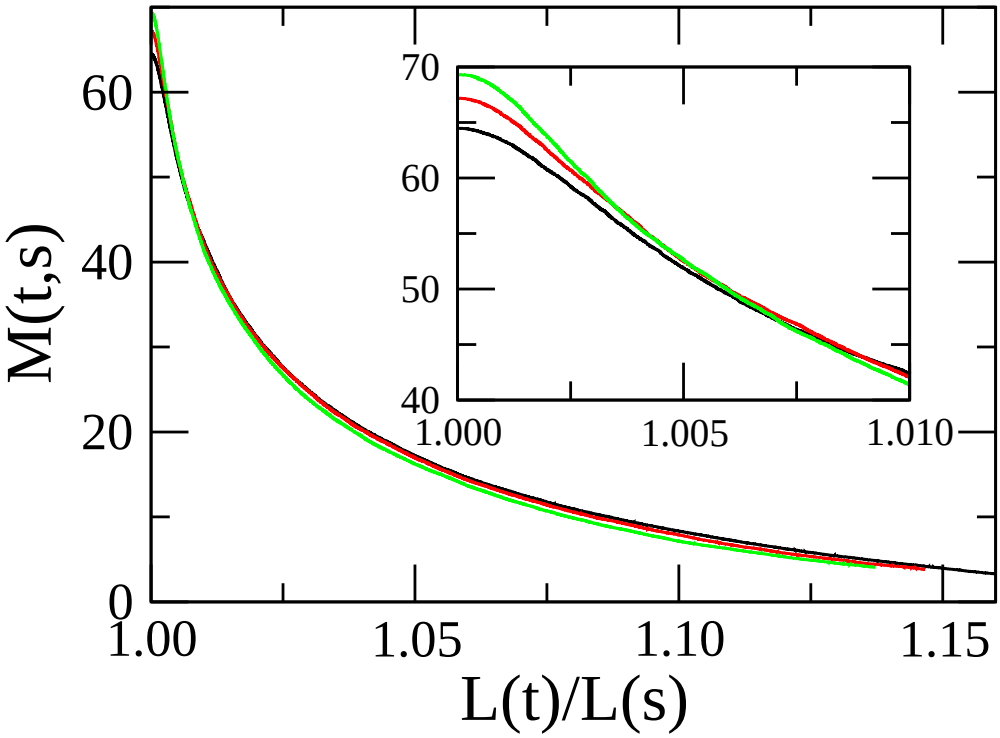

Figure 3.7: (Color online) Response function for the *ABC* model where at the waiting time s the exchange rate is increased from the initial value $q_i = 0.8$ to the final value $q_f = 0.9$. The waiting times are the same as in Fig. 3.5. As the different curves intersect, see inset, no data collapse can be achieved by simply multiplying $M(t,s)$ with a waiting time dependent constant. The data result from averaging over 10000 independent runs. (Reprinted figure with permission from [76]. Copyright (2013) by the American Physical Society.)

using this model we can test the scaling behavior of two-times quantities like correlation and response functions.

Our study shows that in the crossover regime the correlation function can be rather complicated. Once the domains are formed and coarsening proceeds, one enters the logarithmic regime where for waiting times large enough the two-time autocorrelation starts to exhibit a scaling behavior. This scaling behavior is fully elucidated when studying the domain model. In that case we find for the autocorrelation function a standard aging scaling, provided that the time dependence is expressed through the length scale $L(t)$ that increases logarithmically with time.

In order to study the response of the system to a perturbation, we keep the swapping rate q, the only parameter in the model, at some initial value q_i up to the waiting time s, where we then change this rate and set it equal to the final value q_f. We then compare the time evolution of the domains formed using this protocol with that of the domains that are formed when from the start the rate is set equal to q_f. The response function is then a time integrated global response to a global change in the system. Interestingly, we find different types of behavior, depending on whether the rate is decreased or increased at the waiting time. If the rate is decreased, then the difference between the domain sizes of the perturbed and unperturbed systems

decreases logarithmically with time. This then yields again a simple aging scaling with the typical length $L(t)$ as scaling variable, in complete analogy to the behavior of the autocorrelation function. This is completely different when considering the case where q is increased. In that case the domains of the perturbed system grow very fast and rapidly approach the size of the unperturbed system, yielding a regime where the approach to the unperturbed regime displays an effective power-law behavior, with effective exponents that depend on the waiting time. Consequently, no dynamical scaling is observed in that case.

We view the present study as a first step in the systematic study of aging properties of systems undergoing logarithmic growth. We expect additional important insights through the study of space-time quantities, like the two-times space-time correlation function. Also, up to now we restricted ourselves to the global response to a global change. In future, this should be extended to the investigation of the local response to a local perturbation.

The two models studied here have of course no direct relation with the magnetic systems that motivated our study. Still, we expect that some of the results obtained in our study should also remain valid for magnetic systems with logarithmic growth. This is especially true for the simple aging scaling with the scaling variable $L(t)/L(s)$ that is found for the autocorrelation. We expect that this is a general feature of systems undergoing anomalous slow dynamics that is characterized by a logarithmic growth of the typical domain size, including the disordered ferromagnets. Future studies of other systems displaying this type of growth should be able to substantiate this statement. Less obvious for us is whether the intriguing behavior encountered for the global response function is also a generic property. For the disordered ferromagnet the corresponding protocol would consist in letting the system relax in the presence of a magnetic field H, whose value is then changed after the waiting time (this final value could of course be $H = 0$). We then should again have that the domains at the waiting time have a different typical length when compared with the domain size at constant magnetic field. The situation therefore seems rather similar to what is discussed in this chapter. Still, the domains in two- and three-dimensional ferromagnets are very different to the pure domains encountered in the domain model. It therefore remains an intriguing question for the future whether responses in other systems with anomalous slow dynamics behave in a similar way to what has been found in our study.

Chapter 4

Dynamics of the cytoskeleton: experiments and theory

4.1 Soft glassy rheology

Soft glass materials (SGM) encompass materials as diverse as pastes, foams, slurries and emulsions. The dynamical and rheological properties of this class of materials are studied in the linear viscoelastic regime by measuring loss and storage moduli over a certain frequency range. Some of the generic properties of these materials are listed in the following [87]:

1) Their mechanical moduli are in the range of Pa to kPa, while other materials' moduli are in the GPa range. Therefore the Young's modulus of this class of material is less than that of any man-made polymers.
2) The loss tangent $\tan(\delta) = G''(\omega)/G'(\omega)$ [1] is constant in a wide frequency range.
3) The moduli are weak power laws of the frequency of the applied load [2].
4) This class of materials displays aging behavior under defined conditions.

Below the glass transition temperature, T_g, a SGM is in a metastable non-equilibrium state. This metastability and the structural disorder of the material are key concepts in understanding the SGM rheology [112]. The study of SGM shows that molecular mobility is not suppressed even below the glass transition temperature. The resulting slow evolution affects many properties of the system [87] and yields physical aging. Based on observation from the experiments [88, 89], Sollich developed an often used SGM model by making some modifications to Bouchaud's trap and glass phenomenological model [110, 111].

Comparing experimental data for CSK [117] and SGM, one observes that CSK can be described as a soft glassy material. There are three empirical characteristics about a soft glassy material [109]. First, the Young's modulus of these materials is smaller than any man-made polymers. That means this group of material is very soft. The second characteristic is the scale-free dynamics showing no specific frequency, molecular relaxation time, or resonant frequency. The third characteristic is the origin of the frictional stress.

[1] Storage modulus, G', and loss modulus, G'', measure the stored energy in viscoelastic material, representing respectively the elastic energy and viscous and dissipated heat energy in the system.

[2] An external load imposed upon a reacting structure or a required force for opposing, supporting and/or reacting.

In this type of material the frictional stress mainly comes from elastic stress and is not of viscous-like origin.

The original glass rheology model proposed by Bouchaud (1992) [110] studied the general phenomenology of glassy systems. Bouchaud's article [110] mainly focused on disordered structure and metastable configurations in spin-glass systems, see also the 1996 article by Monthus and Bouchaud [111]. These two papers provide the starting point for the soft glassy rheology (SGR) model published in 1997 by Sollich [112]. This theory has pros and cons and there are still some properties of soft glasses that have not been fully explained. Therefore in spite of using this type of material for long time, there is still not a comprehensive theory that allows to explain the characteristic behavior of SGM [129]. Bouchaud's glass model is one of the first analytical models that helped to understand glassy dynamics better.

4.1.1 Bouchaud's glass model

The energy landscape of glassy systems has many local minima surrounded by high energy barriers [87]. These metastable states trap the system in a certain energy configuration for an extended amount of time. The energy landscape is a rough landscape. Under certain energy level f_0, the energy landscape of the system is disconnected and the energy state of the system is hopping between many configurations as shown in figure 4.1,

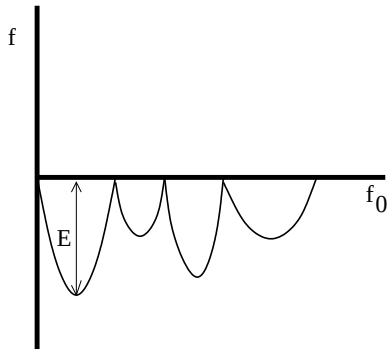

Figure 4.1: The energy landscape displays different metastable states in Bouchaud's model.

The probability of finding a system between two metastable states is negligible. The probability density function to find a system in energy state E is $\rho(E)$. The system is in the canonical ensemble at the temperature $T = \beta^{-1}, k_B = 1$. The system travels from a state with energy E and probability $\rho(E)$ to another state with energy E' and probability $\rho(E')$. Therefore the probability to find a system in time t at the particular energy depth E, $P(E,t)$, evolves with time according to the master equation,

$$\frac{\partial P(E,t)}{\partial t} = -\Gamma_0 e^{-\beta E} P(E,t) + \Gamma_0 \Gamma(t) \rho(E), \tag{4.1}$$

Γ_0 is the attempt rate. The first term on the right hand side is the rate to escape from a trap with depth E at temperature T. The second term gives the probability to hop into the trap with depth E where $\Gamma(t) = \int_0^\infty e^{-\beta E} P(E,t) dE$.

The asymptotic behavior of the distribution of traps plays an important role in the normalization of the stationary distribution. If

$$\Gamma_{eq} = \frac{1}{\int_0^\infty e^{\beta E}\rho(E)dE} > 0 \tag{4.2}$$

then the normalized stationary state of the system $P_{eq}(E)$ is given,

$$P_{eq}(E) = \Gamma_{eq}(\beta)e^{\beta E}\rho(E). \tag{4.3}$$

The asymptotic behavior of the distribution of traps is characterized by the glass transition temperature,

$$\frac{1}{T_g} = \beta_g = \lim_{E\to\infty} -\frac{\log(\rho(E))}{E} \tag{4.4}$$

We conclude from Bouchaud's model [110, 111]:

1. If $\rho(E)$ decays faster than exponentially for large E, then $T_g = 0$ and a normalizable stationary distribution always exists.
2. If $\rho(E)$ decays slower than exponential for large E, then $T_g = \infty$ and a normalizable stationary distribution does not exist.
3. If $\rho(E)$ decays exponentially as $e^{-\beta_g E}$ for large E, then T_g is finite and a normalizable stationary distribution exists above T_g.

These are the main ideas from Bouchaud's model for glassy systems. Sollich modified the spin glass model to some extent and explained the soft glass materials' properties in equilibrium or near equilibrium. The main changes were on the existence of the normalizable stationary distribution. In Sollich's model, the normalized distribution vanishes below T_g.

4.1.2 Sollich's soft glassy model

Sollich formalized the Soft Glass Rheology (SGR) model by picturing a material consisting of a number of elements trapped inside the cages formed by their neighbors. Each individual element can hop in the energy landscape into or out of traps of various depths E, see Fig. 4.2. In Bouchaud's glass model these hopping processes are due to thermal fluctuations, whereas in Sollich's model the interaction and rearrangement of the elements play a more important role than the temperature effect. This coupling between elements, in a mean-field spirit, is represented by an effective temperature x.

There are a couple of modifications in comparison to Bouchaud's glass model. The first one is that the thermal energy must be very small in comparison to the depth of each energy trap. The second one is that the rearrangement of the material in one place affects the material in another place, that means there is coupling between elements of the material. The coupling between elements are unspecified in the model and the only parameter describing these two facts is called the noise temperature x. The last change to Bouchaud's model is to add a new degree of freedom to the system, called strain degree of freedom. This new degree of freedom helps to describe flow and deformation of the material. The model is a one-dimensional model where the strain variable per element is called l. Each element deforms elastically from a local equilibrium

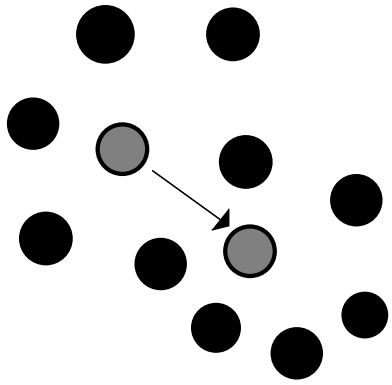

Figure 4.2: Elements escape from a metastable trap to another metastable one.

configuration in order to relax the stress in the element, so that the local strain will be zero. The element deformation continues until it reaches to the yielding point, the maximum deformation length called l_y. The yielding point does not have a single value, instead it has a distribution. Each element deforms elastically. If the perturbation is linear with an elastic constant k, the stress is kl and the maximal elastic stored energy of each element is $\frac{1}{2}kl_y^2$. In this model it is not necessary to know the microscopic details as long as the requirement for the ratio of energy of the trap to the temperature is fulfilled. As macroscopic strain, γ, is increasing, l shows a sawtooth-like behavior.

The time evolution of the system in a given state with energy E, local strain l, and macroscopic strain rate $\dot{\gamma}$ for each element can be found from the equation,

$$\frac{\partial P(E,l,t)}{\partial t} = -\dot{\gamma}\frac{\partial P}{\partial l} - \Gamma_0 e^{-\frac{E-\frac{1}{2}kl^2}{x}} P + \Gamma_0 \Gamma(t)\rho(E)\delta(l), \tag{4.5}$$

where

$$\Gamma(t) = \int\int e^{-\frac{E-\frac{1}{2}kl^2}{x}} P(E,l,t)\,dl\,dE \tag{4.6}$$

The first term on r.h.s of (4.5), which shows the variation in the probability caused by the movement in the same energy trap, can be viewed as describing the flow of the material. The second and the third terms represent the probability to hop into the state with energy E and hop out of the state with energy E. $\Gamma(t)$ is the dimensionless total yielding rate of the system.

On the macroscopic scale, the rheological response of the material is measured by the macroscopic stress

$$\sigma = \int\int klP(E,l,t)\,dl\,dE \tag{4.7}$$

To summarize, Sollich's model is almost the same as Bouchaud's model except for the substitution of β with $\frac{1}{x}$ in the related equations. The normalized probability distribution is discussed for the same three cases as in Bouchaud's model, with x_g being zero, infinite or finite. As long as x is more than x_g, the stationary probability distribution exists. The interesting assumption in Sollich's model is that the noise temperature x can not be tuned from outside. Instead it is self determined by the evolution of the system.

By calculating the integral in Eq. (4.7), one can obtain the nonlinear viscoelastic response of the material where the viscous relaxation depends on the linear strain near equilibrium. The model can also be simplified to get the linear viscous model as well. The main point in this model is that the system is near equilibrium, and the equilibrium probability distribution exists above x_g with small strain. Then from the equation (4.7), one can obtain the complex modulus,

$$G(t) = k\Gamma_0(\frac{x}{x_g} - 1)\int_{1/\Gamma_0}^{\infty} e^{-t/\tau}(\Gamma_0\tau)^{-x/x_g}d\tau \tag{4.8}$$

τ is the average trapping time in a well with depth E, with $\tau = (1/\Gamma_0)\exp(E/x)$.

The dependency on frequencies, ω, of the complex dynamic modulus, the loss modulus G'' and storage modulus G' are given by,

$$G^*(\omega) = G'(\omega) + iG''(\omega) = i\omega \times \int_0^{\infty} e^{-i\omega t}kG_0(\Gamma_0 t)dt = k\Gamma_0(\frac{x}{x_g} - 1) \times \int_{\frac{1}{\Gamma_0}}^{\infty} \frac{i\omega\tau}{1+i\omega\tau}(\Gamma_0\tau)^{-x/x_g}d\tau. \tag{4.9}$$

G_0 is the shear modulus where the strain is zero. This equation is a very general result. If we compare the experimental result in [117, 118] with the SGR model result, we find very good agreement for the storage modulus G' for most of the frequency range in the form of a power law behavior. But for the loss modulus, G'', the agreement between experimental data and the SGR model is poor for some frequency ranges. However, it is still showing power law behavior for some small ranges of frequency.

4.1.3 Comparison of cytoskeleton and soft glassy rheology

From an experiment by Fabry et. al., [117] follows that the cytoskeleton possesses the properties of a SGM. Therefore there is the possibility of modeling the cytoskeleton by using the SGR model of Sollich. The data of the experiments [117, 118] fit quite well with the SGR model. These data show that only drug interactions change the effective noise parameter [87]. By comparing the SGR model and the experimental data, the authors could determine for the cytoskeleton the values of x/x_g, k and Γ_0 [87]. This analysis shows that the drug treatment affects more than one parameter, unlike the results expected from the empirical model. In the experiment, the storage modulus, G', and the loss modulus, G'', have been extracted from the pure data, whereas in the SGR model, these moduli have been calculated from equation (4.9). As can be seen from the figure 4.3, the storage modulus fits quite well the expected linear log-log relaxation-time spectrum. But for the loss modulus the spectrum is showing deviations between the model and the experiment for larger values of frequency $\omega > 10$ Hz.

This comparison focuses on the cytoskeleton properties in a regime where small strain perturbs the system and the cytoskeleton is near equilibrium. If the system is not near equilibrium, it is problematic to use the SGR model. The properties of the cytoskeleton out of equilibrium can be found in [116] where there is a good agreement between SGR model and the data.

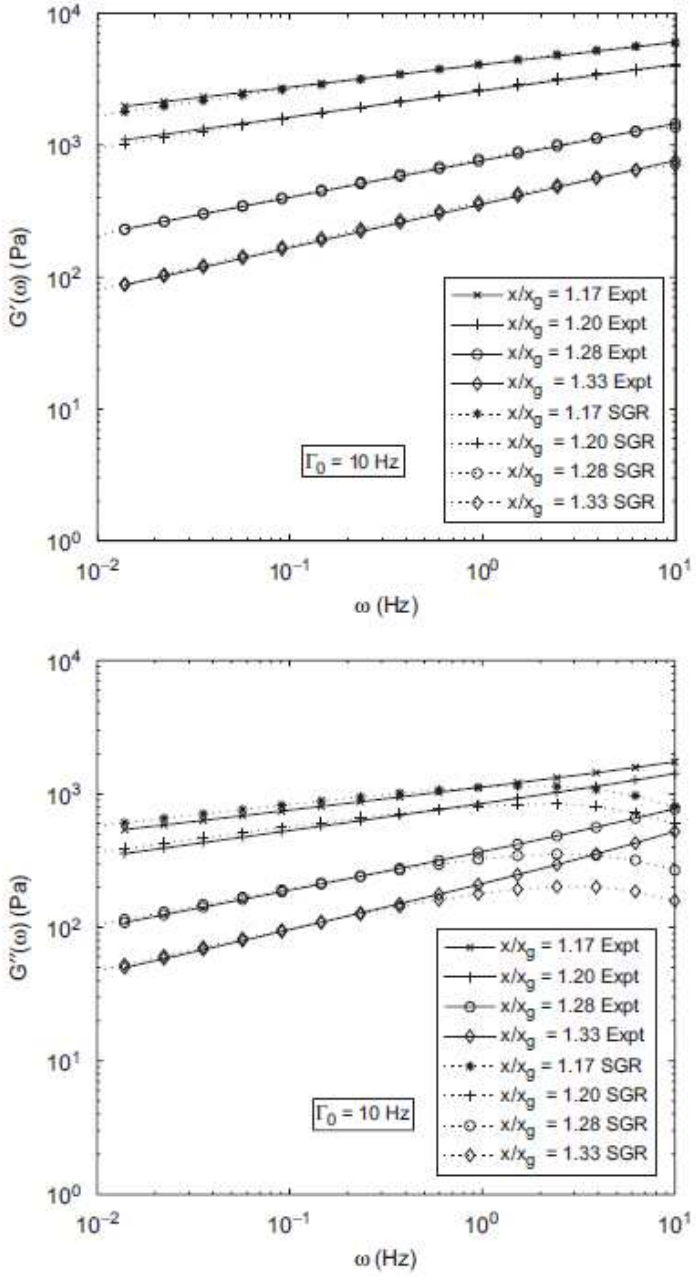

Figure 4.3: The solid lines represent the experiment data and the dashed lines are the regression fit of the SGR model to the data of the experiment [118]. The fitted local elasticities are given as $14.9, 11.1, 5.5, 3.6$ kPa for the cases of x/x_g, $1.17, 1.20, 1.28, 1.33$ respectively (Reprinted from [87] with permission from ELSEVIER.).

4.1.4 Cytoskeleton Soft Glass Rheology (SGR) model out of equilibrium: aging

There are two types of aging in the SGR model [87]:

1. The aging/rejuvenation behavior when the noise temperature is $x > x_g$. This type of aging happens when the far from equilibrium system relaxes to equilibrium. To observe this type of aging, the time interval of the experiment should be large enough in comparison to the microscopic time scale of the system.

2. The aging/rejuvenation below x_g is a second type of aging behavior in this soft glass rheology model. Below x_g, the normalized probability distribution of the system does not exist. Therefore the system ages with time and never reaches a stationary state.

There are many experiments showing the aging behavior in CSK such as Bursac et al (2005) [113], Reese and Govindjee (1998) [114], Govindjee and Reese (1997) [115], and Trepat et al (2007) [116]. To some extend these papers follow the SGR model irrespective of whether the material is above or below x_g.

The study of the cytoskeleton is a very challenging subject. Various types of data are available for this system such as (1) frequency measurements of loss and storage moduli of the system, (2) measurement of local Brownian motion of the system and (3) the relaxation measurements of the system after a large perturbation [87]. All the data show a good agreement with the behavior of the system.

4.2 Experimental studies

Cytoskeleton is one of the organelles inside the cell responsible for the cell's behavior. To study the cytoskeleton experimentally, there are two types of methods that allow to produce a picture of the network, one is fiber-level imaging and the second is indirect or population-level imaging [81]. In addition there are certain experiments that allow to study the dynamics of the cytoskeleton. We will discuss these methods briefly in the following.

The fiber-level imaging techniques are also called light level histology. In this method, the different parts of the tissue are colored and the different matrix components are visualized. This methods are labor intensive, with poor resolution in two dimensions. To visualize the fiber in three dimensions, different imaging techniques, like magnetic resonance imaging (MRI), are used. These techniques have limited resolution in three dimensions.

In the indirect-imaging techniques, one of the used techniques is small-angle light scattering [91]. In this method, the scattering pattern of laser passing through the sample is studied. This pattern reveals the distribution of the fibers in the system [92]. The bulk methods have some pros and cons like other techniques. These methods are easy to implement because the cells can be detected from different angles. But the resolution is not good in comparison to other methods, and the tissue must be transparent (sufficiently thin). In addition to that this method is unable to distinguish between different fiber populations [81].

Other experiments are used to study cell dynamics, as for example optical traps, magnetic beads, glass needles, and atomic force microscope cantilevers. Optical traps are used in order to apply forces of the order of piconewton to nanonewton that allow the detection of the motion on the scale of nanometer to micrometer. Other measurements exploit the thermal motion of the refractive particles. In one of them micron size beads are embedded in the surface of a cell culture. Here we focus on a method that uses magnetic beads since our motivation for this study comes from Fabry's experiment done in 2001 [117].

Magnetic beads were first used in 1922 by Freundlich and Seifriz [80]. They used a manipulator mounted

near the microscope objective in order to insert magnetic particles on the cell surface, after which a magnetic field gradient was applied and a microscope was used. The bead is a paramagnetic particle that allows to detect small forces. One disadvantage of the method was the use of a homogeneous field gradient. This method was further developed by Crick and Hughes (1950) [80]. Their first modification was to magnetize the bead with a large magnetic field before adding a small probing magnetic field: The magnetic beads then twist on the cell surface. Their second modification was to use phagocytic cells. This type of cell prevents damages to the membrane. One of the difficulties in this method is that there is not any control on the connection between the cytoskeleton and the micron-sized beads. In spite of all the challenges, these experimental methods are still used successfully today.

Another widely used method is called Magnetic Twisting Cytometry (MTC). In this method, cells are studied at the tissue and culture level. Magnetic micro-beads [3] are coated with Arg-Gly-Asp (RGD) [4] to be able to connect to specific receptors on the cell surface, that is, they connect via integrin to the cytoskeleton. First, the RGD-coated magnetic beads are magnetized with a strong and short magnetic pulse in horizontal direction. In order to create torque on the beads, a homogeneous magnetic twisting field is used in vertical direction. Magnetic field applies torque on the bead. When the beads are twisted, the mechanical properties of the cells, such as storage modulus (stiffness, G') and loss modulus (friction, G") are measured for each cycle. As cells are attached to the bead, the cytoskeleton deforms because of the bead rotation. Consequently, the created mechanical stresses will oppose the bead rotation. The mechanical stress will disturb the cell more if the elastic modulus is high [108][5]. In order to apply torque on the magnetic beads two pairs of magnetizing and twisting coils were mounted on the microscope stage [6]. The beads were magnetized horizontally with a brief and short magnetic field and twisted vertically by a homogeneous magnetic field [108]. The displacement of the center of mass of each bead was detected and the dynamic moduli were measured as a function of time.

4.3 Theoretical models

Various numerical models are used for the study of bio-polymer networks. Each individual model studies different properties of the cytoskeleton. The simplest models use an idealized geometrical shape, like triangular or hexagonal cell shape. In two dimensions the Mikado model [7] has been used where the positions and angles of the rigid filaments are chosen randomly. The intersection of two filaments are called crosslinks [93, 94, 95, 96]. Often periodic boundary conditions are used. Three-dimensional models are helpful to extract the structure of the network. One important model for our study is the Worm-Like-Chain model for

[3] Magnetic micro-beads, 4.5 μm of diameter, are coated with ligands for specific cell surface receptors.

[4] Arginylglycylaspartic acid

[5] In the experiment, human tracheal smooth muscle cells were harvested and placed in plastic wells at a density of $\sim 20,000$ cells/ well. The beads were coated with RGD peptide and suspended in serum-free medium. Then all of them were added to the culture and stayed for $15-20$ min for incubation at 37^0C to make binding of the beads to integrins on the cell surface. To remove the unbound beads from the cell culture, the well was washed twice with serum-free medium.

[6] Then the system was heated up to 37^0C.

[7] Mikado is a pick-up sticks game originating in Europe. In 1936 it was brought from Hungary to the USA and was mostly called pick-up sticks. This term is not very specific in respect to existing stick game variations. Probably the "Mikado" name was not used because it was a brand name of a game producer.

semiflexible polymers that we present in 6.3. There is another group of models based on tensegrity (tensional integrity). These models are simple and capture the essence of the static network. In the following the tensegrity models and polymer based models are explained in detail.

4.3.1 Tensegrity based models

Tensegrity architecture was studied for the first time by Fuller 1961 [79]. In this model there are some structural members that stabilize the system, called architecture tensional integrity or tensegrity for short. The tensegrity models can be categorized in two classes: continuum models and discrete models [80]. Tensegrity models are often used as static models for the cytoskeleton even though this organelle is a dynamic network. This approach was introduced for the first time by Ingber in 1993 [78]. Ingber's model is based on the network structure and provides the stability for the network through an agency or cable-like structural members called prestress[8].

Continuum models range from simple to complicated, covering the whole range from elastic to viscous behavior. In the continuum models the stress bearing element is small compared to the length of the cell. Also, the stress bearing elements are distributed homogeneously inside the cell's body. This type of structure provides continuous patterns of stress and strain inside the cell [80].

Discrete models study the structure by utilizing the agency of the stress bearing elements that are widely separated inside the cell. In the discrete models, unlike in the continuum models, the stress bearing elements do not cover the whole space of the cell. There is a subclass of discrete models called stress supported or prestress structure models. To maintain structural integrity inside this subclass even before adding external load, these types of structures need tensile elements. One of the models that are based on the architecture of the cytoskeleton and that consider prestress agencies has been proposed by Donald Ingber [80].

There are three general types of models based on tensegrity that are used for the description of the cytoskeleton: the cortical membrane model, the tensed cable net model, and the cable and strut model. The major differences between these models are the topology, the architecture of the network and the way to balance the prestress.

The cortical membrane model is based on cortical layer(s) as bearing tension elements. The model has been applied successfully in various suspended cells[9] but has limited success in adherent cells[10]. This group of models are successful in studying the static properties of the cytoskeleton. Since the cytoskeleton is a dynamic system, dynamics needs to be included in the theoretical model. Therefore tensegrity models are not appropriate for studying dynamical properties, even so they can be used successfully for the description of static properties.

One of the experiments that partially supports this types of model is magnetic twisting cytometry (MTC). The main idea in the experiment is that the beads are attached to the surface of the cell cytoskeleton via integrin. By applying magnetic field on the beads, the restoring forces inside the cell resist the cell move-

[8] Prestress introduces internal stresses into a body.

[9] Suspended cells remain floating in the medium when grown in liquid culture and will not attach to the cell culture vessel.

[10] Adherent cells from most of the body's solid tissues will only grow in culture if they are in contact with a solid surface and other cells.

ment. By using the cortical membrane model, the stiffness of the cell cytoskeleton in MTC can be analyzed. Figure 4.4 shows the details.

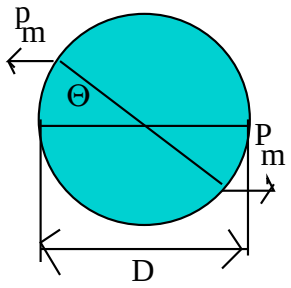

Figure 4.4: In a MTC experiment a bead is attached to the cell surface. The magnetic field applies torque on the bead. This mechanical perturbation moves the center of mass of the bead connected to the cell surface.

There are certain common points between the experiment and the model, but there are also some discrepancies. There is a good agreement between the model and the experiment in the measurement of the linear shear modulus, G. But the first discrepancy is that G decreases in the model when the bead angle, θ, is increasing. But there are some experiments where the magnetic twisting cytometry shows stress hardening [82] or constant stiffness [117] when θ is increasing. The second discrepancy is that by increasing the diameter of the bead, G decreases while the experiment actually shows the opposite result [128]. The main reason for these discrepancies is the shape of the prestress element in the model. It would be better to have a shell-like rather than membrane-like structure. The model is still good enough for suspended cells where the cytoskeleton is in a thin cortical membrane [83, 80].

The second model that is worth mentioning is the tensed cable model [80]. This model makes several assumptions, such as affine approximation (local strain behaves like the macroscopic (continuum) strain field [80]), equally probable orientation of the cables in the network, and homogeneous prestress distribution inside the cytoskeleton (in real cells, prestress increases near the cell edges, decreases through the nuclear region [80] and only involves actin network inside the cytoskeleton). Additionally the cytoskeleton is considered as a static and elastic network, when in reality it is a dynamic and inelastic structure. Some two-dimensional models of the cytoskeleton consider the network building blocks as triangles [84] and hexagons [85]. Actin cortical models show pretty good agreement with experimental data for suspended cells; however they have moderate success for adherent cells.

The last tensegrity model to be discussed is the cable-and-strut model [80]. An image of the structure is shown in Figure 4.5,

At each node in the model one strut and several cables meet. The tension in this model is balanced through the struts (thick black lines) and cables (white lines). It can also be balanced by attaching it to a substrate. This is the first tensegrity model that includes microtubules as separate entities in the network. In addition, it shows good agreement with experiments.

One famous models in these last group of tensegrity models is called the six-strut model and is shown in the Figure 4.6 [80].

This model is used widely for the cytoskeleton and studies the cell deformability. In this model there are

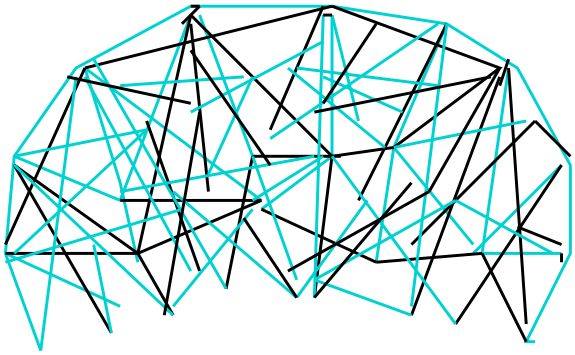

Figure 4.5: A cable-and-strut tensegrity dome. In this structure, tension in the cables (blue lines) is partly balanced by the compression of the struts (thick black lines) and partly by the attachments to the substrate. At each free node one strut meets several cables.

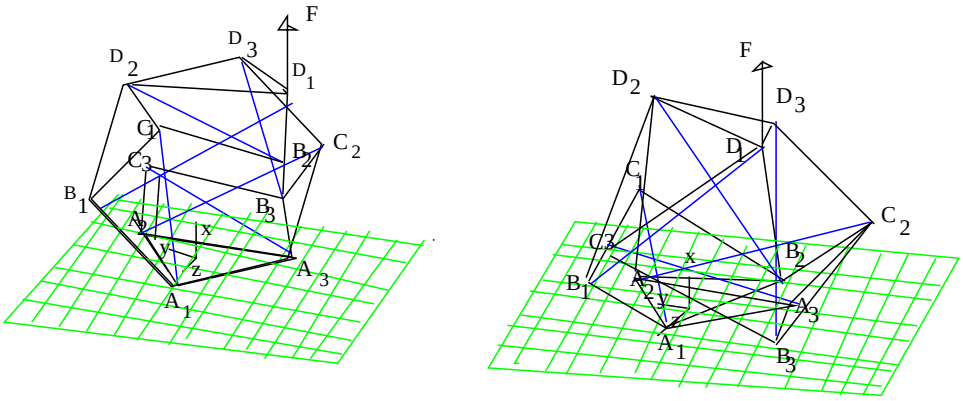

Figure 4.6: Six-strut tensegrity model in the round (a) and spread (b) configurations anchored to the substrate. Anchoring nodes A1, A2 and A3 (round) and A1, A2, A3, B1, B2, and B3 (spread) are indicated by solid triangles. Pulling force F (thick arrow) is applied at node D1.

six struts and 24 cables. As mentioned before, at each node one strut and several cables meet. The struts can be slender bars that maintain the cell balance. There are two types of configurations in this model. One is the so-called round configuration, where the system is balanced via struts compression. The system also can be attached to a substrate to balance the system. Another configuration is spread configuration. In this configuration, more nodes anchor to the substrate, which increases the cell stiffness [86]. In this model the cell is balanced through the strut's compression. When the cell is spreading, the force distribution is balanced partly through the struts and partly through the cables. If anchoring of the nodes to the substrate continues, the role of the struts will be eliminated, and the substrate plays a vital role in the balance.

To summarize, all three tensegrity models reveal how the cell balances prestress. In each model the cell balance is maintained by changing the spacing, orientation and length of the structural members of the cytoskeleton [80]. Furthermore, the relation between stiffness and structure is common to all structural models [80].

4.3.2 Polymer based models

The coarse grained biopolymer network models consider interconnected filaments with interaction points that are called nodes. The nodes can be of two types, one called entanglement nodes and the other one called crosslinks. The entanglement points are close enough to make a new connection and change the network structure. The crosslinks are chemical bonds between two points in the network. The polymer length between two points is called l_s. The different types of polymer networks are defined through the flexibility of the polymers which is summarized by the persistence length l_p. The persistent length of the polymer is thereby defined as [81],

$$< \cos[\theta(s) - \theta(0)] >= \exp[-s/l_p] \tag{4.10}$$

where $\theta(s)$ is the tangent angle with respect to the filament axis [97] as shown in the figure,

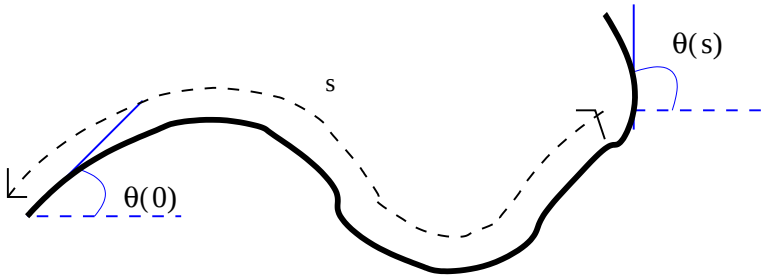

Figure 4.7: s is the arc parameter along the polymer. $\theta(0)$ is the angle between the tangent line at $s = 0$ and the x axis of the chosen coordinates for the filament whereas $\theta(s)$ is the corresponding angle at arc length s. As the arc length increases, the tangent angles $\theta(0)$ and $\theta(s)$ become uncorrelated.

The persistence length l_p depends on the bending stiffness K_b through $l_p = K_b/kT$. Here k is the Boltzmann constant and T is the temperature. If $l_s \gg l_p$, the polymer belongs to the flexible polymer group with properties that are dominated by entropic effects. For semiflexible polymers we have that $l_p \approx l_s$. Their dynamics is complex, and their mechanical and entropic behavior depends on the situation in the system. In the other limit when $l_p \gg l_s$, we deal with stiff polymers, whose mechanical properties play important roles in the dynamics of the network. Hence, the entropic properties are not involved in the stiff network dynamics.

In general, the polymer based models belong to two groups. One is composed of affine models and the other is formed by non-affine models. In affine models the co-linearity of the nodes and the ratio between distances are conserved [81].

Affine Models

A typical deformation in an affine model is the simple shear where the volume is conserved:

$$(x,y) \rightarrow (x+\gamma * y, y) \tag{4.11}$$

where $\gamma = \tan\theta$ and θ is the shear angle. It follows from equation (4.11) that under this transformation nodes are moving in a rapid pre-described way without considering the interactions between them. Still, affine deformations describe many experimental facts. Affine theory successfully explains the strain stiffening of biopolymer gels [127] and the negative normal stress during shear [98]. In addition, it has been implemented successfully for flexible gels. The elastic modulus in the gel, G', depends on the cube of the mesh size [99]. The mesh size is the average diameter of a sphere that fits inside the network without touching points. For semiflexible polymers with affine deformation the mesh size is of the same order as the persistence length [100]. The affine theory is helpful to understand experiments at the bulk level whereas there are still unclear properties at the fiber level. To understand the properties of the system in detail, non-affine deformations are very useful, as they also show some agreement at the level of the fibers, as described in the following.

Nonaffine Models

There are three initial steps in creating a nonaffine model. The first one is choosing the structure of the network and the degrees of freedom in the model. The second is setting up the interaction between nodes that include crosslinks and entanglement points. The last one is organizing the segments in the network. In this type of models each segment is considered as a linear or a non-linear spring or it can be a beam or worm-like-chain that resists bending and torsion. The crosslinks are chemically bonded nodes that behave as freely rotating pin joints, welded joints of fix angles, or linear or torsional spring [81]. There are three models that we discuss in the following which belong to the subgroup of nonaffine models, e.g. the Spring Models, the Beam Models, and the Entropic Beam Models.

The idea of the Spring Models has been used in papers by Kellomaki [96], Chandran and Barocas [101], Wyart [102], and Palmer and Boyce [103]. In Kellomaki's model, the springs are randomly oriented inside the network. Under small deformations the network is floppy, and without changing the spring lengths the crosslinks reorganize the network and relief the tension. Therefore the shear modulus is zero which is unrealistic in biopolymers. Chandran and Barocas studied the spring network in order to discuss collagen gels. They found that the affine deformation can not support the bipolymers deformation on the fiber level while in the bulk level there is consistency with affine model. Their result was similar to what Kellomaki obtained from the random spring model. There are couple of other models, such as Mikado model, that study the biopolymers broadly, but the result of zero shear modulus obtained in all these studies is unrealistic. In addition to all the floppy spring models, Wyart considered a rigid spring network in order to study the strain stiffening properties of the network, but the model does not allow to explain properties of biopolymers [81]. The last spring network model that we discuss here is the eight-chain network by Palmer and Boyce for actin networks. In this model, each cell consists of eight springs connected from the center to each corner of the cell. This network is considered to be stiff with incompressibility constraint, but the elements forming the network are floppy. This very simple model is unrealistic [81].

The second group of nonaffine models are Beam Models. As it is obvious from the Spring Models, the study of biopolymers should consider bending of the filament in addition to stretching. Therefore the spring random model is not sufficient. In order to add bending to the system, one needs to consider a Worm-Like-Model [104] or a finite element algorithm [106, 105].

In the third group of models, called the entropic beam models, the entropic component of the stretching stiffness of an individual filament is added. In this model, the stretching stiffness k_s of a segment is modeled as two springs connected in series with elastic stiffness $k_{el} = EA/l_c$ and entropic stiffness $k_{en} = k_b^2/k_B T l_c^4$, where E is Young's modulus, $A = \pi r^2$ and r is the radius of the cross-section of the beam. k_b is Boltzmann constant and T is the temperature. The total stretching stiffness is given by $k_s^{-1} = k_{el}^{-1} + k_{en}^{-1}$. Entropic stiffness is the weakest spring, $k_s \sim l_c^{-4}$, whereas for the purely mechanical network $k_s \sim l_c^{-1}$. In this system the critical average segment length, l_{crit}, characterizes the behavior of the system. When $l_c < l_{crit}$ the network deformation is affine, when $l_c > l_{crit}$ the deformation is nonaffine [81].

The closest model to our model used in the following is the model of a multiply crosslinked semiflexible polymer network studied in [125] using Monte Carlo simulation. This model creates a three-dimensional realistic network of F-actin polymers. First, N crosslinks are placed inside a cell with periodic boundary conditions in three dimensions. Then a four fold connected network is created by adapting a method initially introduced in [122] where it has been used to create random networks [121] for the study of amorphous solids [122]. This step creates a connected filament formed by $2N$ segments and by following the filament from one side of the cell we reach to the other side. For each segment between two crosslinks, a contour length obtained from the radial distribution function of the end-to-end segment is assigned [123]. The detail of the model will be given in chapter 6. The free energy assigned to each filament is given by

$$E_{fil} = \int_0^{lc} (\frac{\kappa}{2} |\frac{d\hat{t}(s)}{ds}|^2 + \frac{f}{2} |\hat{t}(s)|^2) ds \tag{4.12}$$

where s is the arclength coordinate, κ is the bending stiffness, that is $\kappa = l_p \beta$, with $\beta = \frac{1}{k_B T}$, $\hat{t}(s)$ is the tangent vector along the filament, and f is the force that is acting on each crosslink.

The free energy has two terms, one internal segment part called F_2, whereas the other one is the intersegment part E_3. The internal degree of freedom for each segment is integrated out. In the model, two separate cases for positive and negative forces are considered. For the positive force, the analogy of Marko-Siggia [120] interpolation formula is applied to semiflexible polymers. Adapting the Worm-Like-Chain (WLC) model [90] for semiflexible polymer does not give an accurate description. The main reason is that the transverse and longitudinal behavior of this type of polymers is not symmetric. For the negative forces, the authors of [125] used the classical Euler buckling forces. The final expressions are

$$\beta F_2 = \begin{cases} -\frac{9g(r_{ij})^2[5+6g(r_{ij})]}{-1+6g(r_{ij})} & f > 0 \\ |(-\frac{1}{90} - 1 + exp[90g(r_{ij}/\pi^2)]\pi^4 + \pi^2)| & f < 0 \end{cases} \tag{4.13}$$

$$g(r_{ij}) = -l_p/l_{c,ij} + 1/6 + l_p r_{ij}/l_{c,ij}^2$$

where r_{ij} is the Euclidean distance between node i and node j.

If the applied force is positive, the bending energy or intersegment energy is

$$\beta E_3 = \frac{l_p \theta_{ijk}^2}{l_{c,ij} + l_{c,jk}} \tag{4.14}$$

$l_{c,ij}$, $l_{c,jk}$ are the contour lengths of the segments connected to the cross links i, j and j, k, respectively,

whereas θ_{ijk} is the angle between the two segments represented by vectors. The total energy of the network is the sum of the contribution of each individual filament.

There are certain simplifying assumptions in this model such as extremely small crosslinks (one dot), inextensible filaments that completely ignore the backbone stretching, no dangling ends, and excluded volume and steric avoidance.

The system is then relaxed using three different Monte Carlo moves. First, in an initial relaxation step the long entangled filament is rewired. After the energy of the initial long filament has been minimized, this filament is chopped in order to reach the desired number of filaments. A list of crosslinks' positions $\vec{x}_i$, contour lengths $l_{c,ij}$ and a connectivity matrix, that shows the connection between crosslinks, are kept. Then two other topological moves are used to create a homogeneous and isotropic network. These moves are called relabeling and shifting nodes. Details on these topological moves will be given in chapter 6.

The authors of [125] looked at the mechanical response of the network to a shear. They mainly focused on the role played by the structural architecture in the mechanical properties of the network. Mainly the strain stiffness and the nonaffine behavior of the network were studied. The best agreement between the model and the experiment was found for the modulus of the semiflexible polymer network for small shear. As stated in the Ref. [127] the modulus of the network collapse on a master curve by dividing the actual stiffness by the initial stiffness K_0 (K/K_0) and the shear by four times the initial shear (γ/γ_4) with $\gamma_4 = 4\gamma$. They also found a scaling of stiffness as a function of stress that is in agreement with the experiment [127]. In this model, the reorientation of the segments is nonaffine. They monitor the nonaffinity correlation function of the system. It is mentioned in the paper that the results are in general in good agreement with the experiment, but that the quantitative agreement with the experiment is hard to catch. In this paper they could make a connection between microscopy and macroscopy of the network. Like most of the other papers, their network contained a single filament type.

Some additional work has been done by E. M. Huisman et al. [126], which considered a three-dimensional realistic model of F-Actin network in order to check the importance of physical quantities such as actin concentration, crosslink density, and the architecture of the network. This model presents some constraints such as fixed crosslink. In addition, there is no supporting experiment to show how the structure of the actin network depends on architecture.

In Huisman's model, the segments with length L_0 are placed randomly inside a periodic cell with length W. Each filament is divided into different segments that are able to twist (stiffness ω), bend (stiffness κ), and stretch (stiffness μ). The attraction force between segments is varying with the distance like $1/r^2$. When the distance between end points of the two segments reaches the cutoff distance, a rigid crosslink with fixed length is created. At each crosslink maximum four segments meet. Once the network has been built, internal stretch keeps the system highly stressed.

The energy is composed of two parts: bending and stretching energy. The torsional energy is negligible in all the regimes, while in small strain the bending energy is dominant. By changing the strain stiffening constant, γ, three different regimes are encountered. The first one is the small strain coefficient regime where the bending energy is dominant. The second regime is the turning point of the network, which is the medium strain regime. The last regime is the axial energy (stretching energy) dominated regime with high stress values.

There are no experiments to support this model, but still the three-dimensional model exhibits interesting

properties. The study shows that the response of the system highly depends on the structure of the network. One of the physical quantities that have been monitored is the initial stiffness of the network $G_0 = d\tau/d\Gamma$. The study shows that stiffness increases when filament length increases. The authors also fixed the length L_0 (filament length) and varied l_c (distance between crosslinks) and c_a (crosslink concentration). The study shows that

$$G_0 \propto l_c^q \qquad q = -4.0$$

$$G_0 \propto c_a^p \qquad p = 2.0$$

This study also revealed the behavior resulting from affine transformations. To show that, the cell is sheared with shear strain γ in the xy plane. The three-dimensional cell then exhibits nonaffine motion normal to the shear plane. The two nonaffine quantities,

$$A = < |\Delta u|^2/|u^{aff}|^2 > \qquad \text{and} \qquad S = < |\Delta r|^2/|\Gamma|^2 >$$

where Δr is the mean deviation from the affine position of each individual crosslink for each strain and Δu is the difference in the crosslink displacement u, quantify the deviations from affine behavior as a function of strain Γ.

In three-dimensional models the constraints are reduced in comparison with two-dimensional models, while showing nonaffinity very well. The stiffness of the network thereby highly depends on the local geometry around each crosslink.

Chapter 5

Two-dimensional model of the cytoskeleton

5.1 Introduction

In the following we discuss a two-dimensional crosslinked model for the cytoskeleton (CSK). We follow ref. [131] where a rectangular cell was used for the airway smooth muscle cell, whereas crosslinks represent the contractile apparatus. In this model, we study the evolution of the link numbers both for a lattice model and an off-lattice model. In addition, the effects of perturbations are studied. The evolution of the network proceeds in two steps, one involving link formation, the other link dissolution.There are two important factors in the link formation: the fraction of available contractile units and the distances between nodes. At any given time step, the probability to connect two crosslinks i and j is,

$$P_{ij}(t) = \frac{L_t - L_n(t)}{L_t} \frac{1}{d_{ij}^s} \tag{5.1}$$

L_t is the maximum number of links in a network with a fixed number of nodes and $L_n(t)$ is the number of links at each time step. Then the ratio of $(L_t - L_n(t))/L_t$ shows the fraction of available contractile units at each time. The second part is $\frac{1}{d_{ij}^s}$. If $s = 0$, short and long links are created with the same probability. For nonzero values of s the probability to create a long link between nodes i and j decreases when the distance d_{ij} increases. The second important feature of the model is dissolution of links. By adding a probability to remove links, the model becomes a version of the birth-death model [132]. The assigned probability has two parts:

$$B_{ij} = b_0 + b(t). \tag{5.2}$$

One is a constant probability, b_0, and the other one is a time dependent part, $b(t)$. The time dependent probability is related to the dynamics inside the cell. The dynamics inside the CSK is influenced by many proteins and their mutual interactions [131]. In a phenomenological description this complex dynamics can be described by an effective temperature, x, as stated in chapter 4. The effective temperature describes the trapping and hopping related to the deep energy wells of non-thermal origins. As it is discussed in

section 4.1, Sollich's model of Soft Glassy Materials (SGM) [112] provides a good description for SGM. The molecular interaction in this type of material is of intermediate strength, not as strong as in solids and not as weak as in liquids or gases. Therefore the evolution over time is complicated, due to the existence of local cages that provide local minima energy. In the real system the physics is very complex due to many interactions inside the cell such as hydrolysis of ATP, internal cell friction, shortening velocity and the rate of the network turn over [131]. Including all the factors, the dissolution probability can be written as [131]

$$B_{ij} = b_0 + b_1 \exp(-rt). \tag{5.3}$$

where b_0 and b_1 are constants, t is time and r is a rate that we keep constant in our simulation: $r = 1/\tau$ and $\tau = 10000$. When $t = 0$, the dissolution rate is at the maximum value of $b_0 + b_1$. As a function of time the probability then decreases exponentially to b_0.

This chapter address two main points. First we study properties of the two-dimensional model and then we monitor the network in the presence of a perturbation.

5.2 Properties of the two-dimensional model

5.2.1 Formation probability

Let us start with the lattice model. In this model, there are N^2 nodes or crosslinks in a square cell with fixed side length L. As mentioned in the introduction, the probability of creating a link between nodes i and j is,

$$P_{ij}(t) = \frac{L_t - L_n(t)}{L_t} \frac{1}{d_{ij}^s} \tag{5.4}$$

To understand the creation probability, a schematic picture of the lattice for two different values of the exponent s and $N^2 = 100$ is shown in Fig. 5.1. For small values of s we have both short distance and long distance links, but for large values of s most of the links are between nearest neighbors. The number of links in the network, L_n, is evolving. The typical behavior of L_n over time is shown in Fig. 5.2 when $s = 2$.

According to Fig.5.2, the number of links at each time step, $L_n(t)$, increases in the short time regime. In the long time regime, the system reaches a stationary state. The typical behavior of the network depends on the number of crosslinks, N, and the exponent, s. For each case, we find the following time dependency of L_n:

$$L_n = P_l - b * \exp(-at), \;\; a > 0, \;\; b > 0 \tag{5.5}$$

P_l is the stationary value of each graph at $t = \infty$ and $\frac{1}{a} = T_1$ is the typical time constant in the lattice. For different values of N and $s = 0, ..., 7$, T_1 increases when $s \leq 2$. For larger values of s, it is decreasing as seen in the table 5.1 for $N = 40$.

For different values of N and s, we measure T_1. For the studied systems the largest and smallest values of T_1 are obtained for $s = 2$, $N = 60$ and $s = 0$, $N = 5$ respectively. So the time range is:

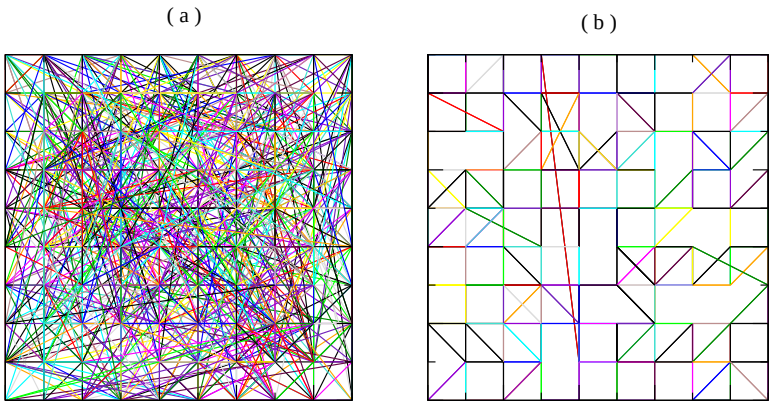

Figure 5.1: (a) For small values of s, s=2, lengths of the created links are both short and long. (b) For large values of s, s=7, most of the created links are between nearest neighbors.

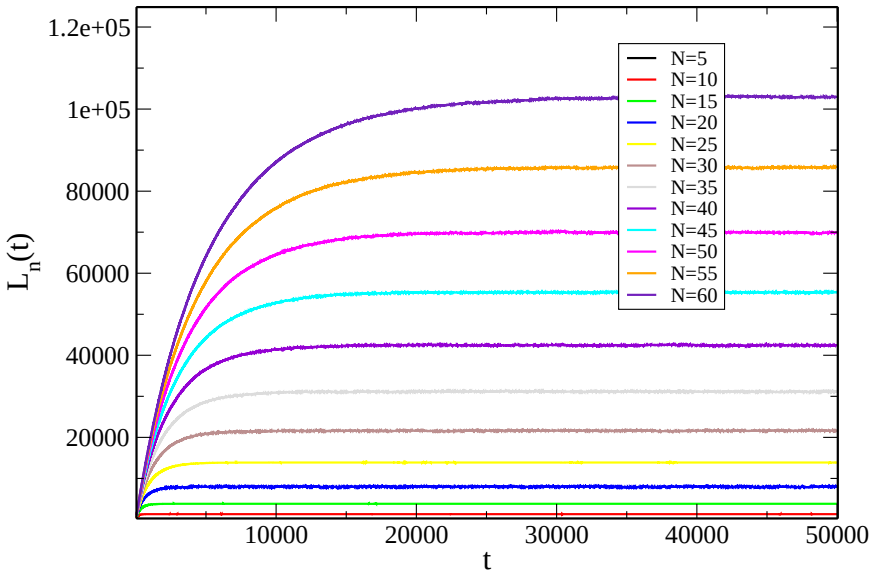

Figure 5.2: The number of nodes are increasing from 5^2 to 60^2. When the number of nodes increases, the time to reach the stationary state increases.

s	0	1	2	3	4	5	6	7
T_1	428.02	1931.2	2480.03	2003.5	1752	1458.8	1345.35	1301.5

Table 5.1: For N=40 and different s values, the time to reach to stationary value, T_1, is changing. T_1 increases when $s \leq 2$, but decreases for larger values of s.

$$16.44 < \frac{1}{a} = T_1 < 5368 \tag{5.6}$$

When $s = 0$, there is no constrain on link formation. Therefore, the system reaches the stationary state much faster than for any other system with $s > 0$.

5.2.2 Stationary values of L_n

As Fig. 5.3 is showing, the stationary values of the number of links in the lattice, p_l, strongly depends on the number of nodes, N. The data shows the power law behavior for P_l vs N.

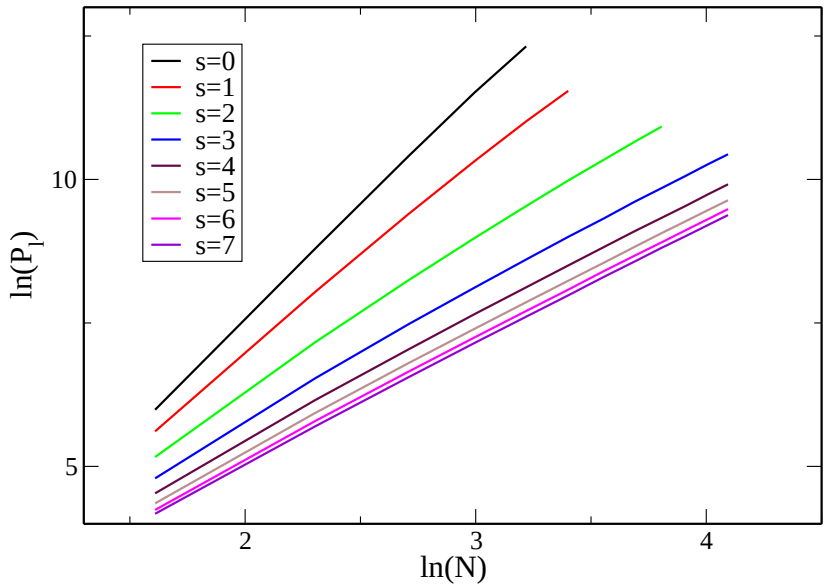

Figure 5.3: Stationary value, P_l, is plotted as a function of the number of crosslinks, N, in the network.

From the data, we propose the following relation between P_l and N,

$$P_l = kN^q \tag{5.7}$$

The values of the exponent q can be read off from the data plotted in a log-log plot,

$$\ln P_l = q \ln N + \ln k \tag{5.8}$$

The slop of each line in Fig. 5.3 gives the value of the exponent q. The table 5.2 shows the data for different values of s and q .

It follows from table 5.2 that the slope of the line, q, changes from 4 for $s = 0$ to 2 for $s = 7$. This result shows that for $s = 0$, when there is no restriction on the distance between nodes, we get the result $C(N^2, 2)$ where we choose 2 nodes out of N^2 nodes,

s	0	1	2	3	4	5	6	7
q	3.9523	3.3289	2.5419	2.2478	2.1466	2.1103	2.0958	2.0862

Table 5.2: When the exponent, s, increases from 0 to 7, the exponent q decreases from almost 4 to 2.

$$P_l \propto N^2 * (N^2 - 1) \tag{5.9}$$

so that the stationary value is proportional to N^4. However, for large values of s most of the links are between nearest neighbors. If there are N^2 nodes, the number of links will be $2N^2$. So the power is changing from $q = 4$ to $q = 2$ when s increases.

5.2.3 Dissolution probability as a function of time

In the next step the dissolution of crosslinks is added. As it is mentioned in the introduction, the dissolution probability B_{ij} is:

$$B_{ij} = b_0 + b(t) \tag{5.10}$$

The first term of Eq. 5.10 is a constant. The second term, $b(t)$, which is a function of time, has been suggested by Gunst and Fredberg in order to explain some experiments [130]. $b(t)$ is assumed to be an exponential function [131]:

$$b(t) = b_1 e^{(-t/\tau)} \tag{5.11}$$

τ is the typical time constant for the dissolution probability, and $\tau = 10000$ is larger than the typical time constant T' that describes the relaxation of the system [1] [2] [3]. In our simulations we measure the time constant, T', which is a measure of the time needed to reach the stationary state. Comparing systems with $B_{ij} = b_0$ and with $B_{ij} = b_0 + b(t)$, we expect that the relaxation time is larger in the case with a time-dependent B_{ij}. This is shown in Fig. 5.4 for $N = 40$ and $s = 0$.

For different values of s and $N = 40$, the time T' is shown in the table 5.3 for $\tau \gg T_1$. τ is a time constant for the dissolution probability in equation 5.3.

For constant N^2 there is a maximum value of T' for $s = 2$ and a minimum value for $s = 0$. This is the same behavior that we observed in the system without link dissolution.

[1] T' is the time constant of the system with formation and dissolution of links.
[2] T_1 is the time constant related to the formation of links.
[3] τ is a time constant for the dissolution probability in equation 5.3.

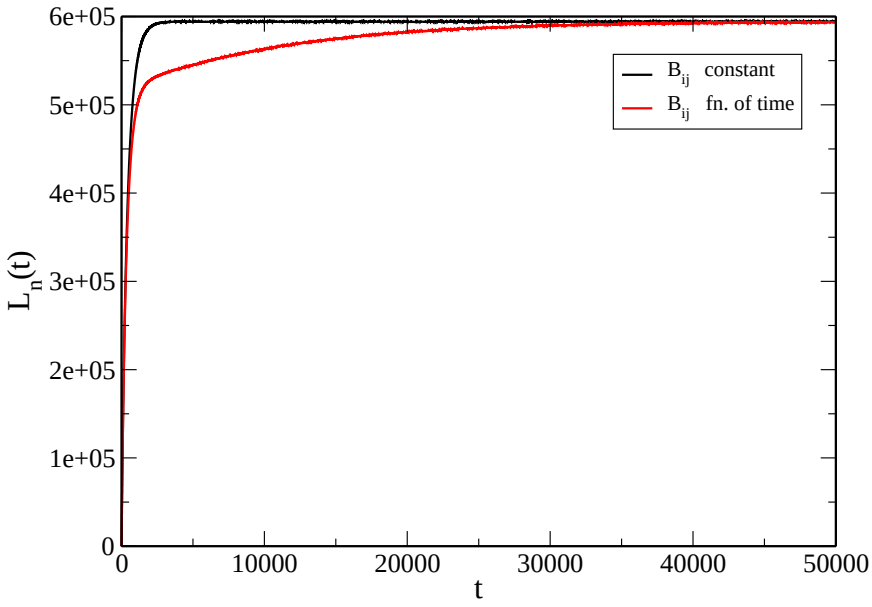

Figure 5.4: For $N = 40$, $s = 0$, $b_0 = b_1 = 0.5$, and $\tau = 10000$, we plot the number of links as a function of time. The black curve is the number of links for constant dissolution probability, $B_{ij} = b_0 = 0.5$. The red curve is the number of links when B_{ij} is a function of time. The system with time dependent B_{ij} takes longer to reach the stationary value.

S	0	1	2	3	4	5	6	7
T'	548.8	2101.28	2692.80	2313.1	1784.79	1729.7	1696.38	1660.63

Table 5.3: For $s < 3$, the typical time constant, T', is increasing. For larger values of s the time constant of the system is decreasing.

5.3 Mechanical response to an external perturbation

To study the mechanical response of the cell to an external perturbation, we add shear or tension to the system. The stretching coefficient is α and the shear angle is β. Pictures of the stretched and sheared cells can be found in Fig. 5.5.

5.3.1 Lattice simulation: Stretching the cell

The original cell is stretched in y direction. To keep the area constant, the side in x direction is compressed. In Fig. 5.6 we show as an example the time evolution of the number of links when a system with $s = 3$, $N = 20$ is stretched at time $t = 30,000$.

After adding external perturbation to the system, the number of links, L_n, will reach a new plateau value, P_l, see Fig. 5.6. For $\alpha = 0.1$ and $\alpha = 0.2$, the new stationary state values are higher than the values

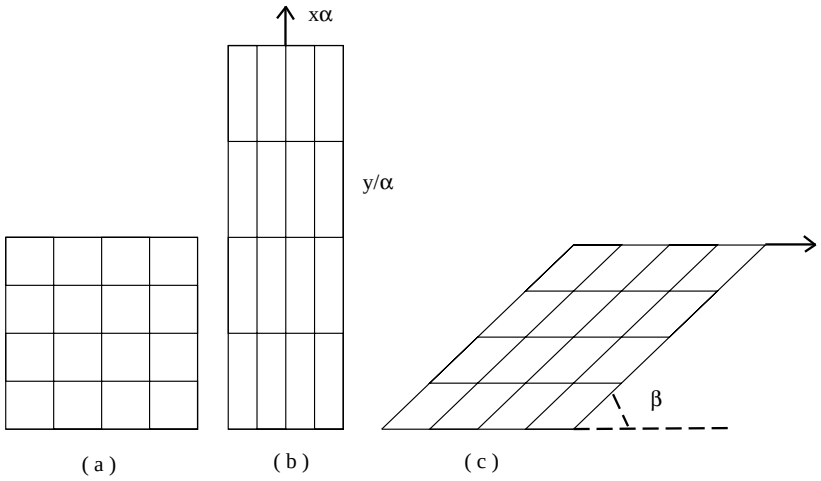

Figure 5.5: (a) Initial cell is shown. (b) Cell is stretched with constant area. The horizontal direction (x-direction) is compressed by α and the vertical direction (y-direction) is stretched by $1/\alpha$ ($\alpha < 1$). (c) Cell is sheared with constant area and shear angle β.

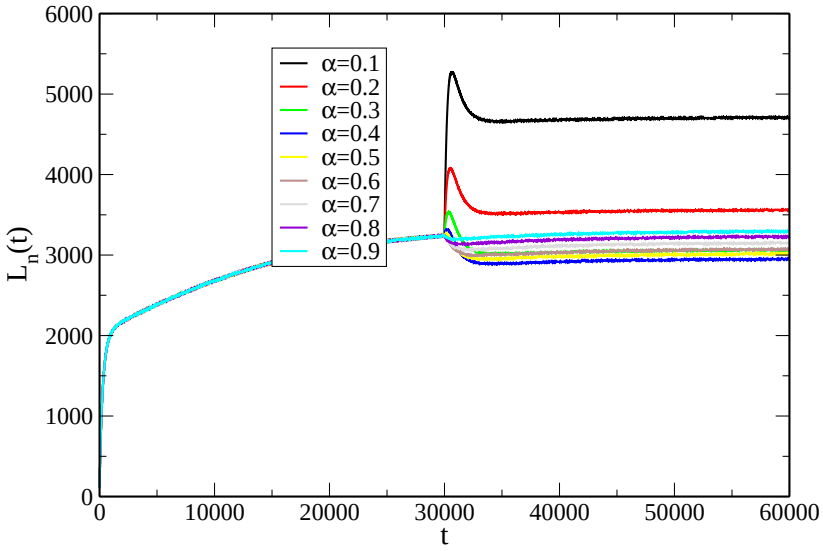

Figure 5.6: At time $t = 30,000$ the cell is stretched. For $\alpha < 0.6$ the number of links increases before reaching a stationary state. For other values of α the number of links is decreasing monotonously. The data result from averaging over 1000 independent runs.

before stretching the cell. When the value of α increases from 0.3 to 0.5, the new stationary state value, P_l, decreases. When α varies from 0.6 to 0.9, the plateau values will be almost the same as before the stretching, because for α values close to 1 there is only a small change of the cell. For α values less than 0.6, we observe an overshooting when we add tension to the system. This shows that previous links still exist right after the stretching, and it takes time to reach the new stationary state. The stationary number of links are very close for some α values such as 0.6 and 0.3.

To understand the general behavior of the system when it is stretched, we count the number of links in three directions, namely x, y and d (diagonal). For $s = 2$, $N = 20$, $\alpha = 0.8$, the number of links in each direction is plotted in Figure 5.7.

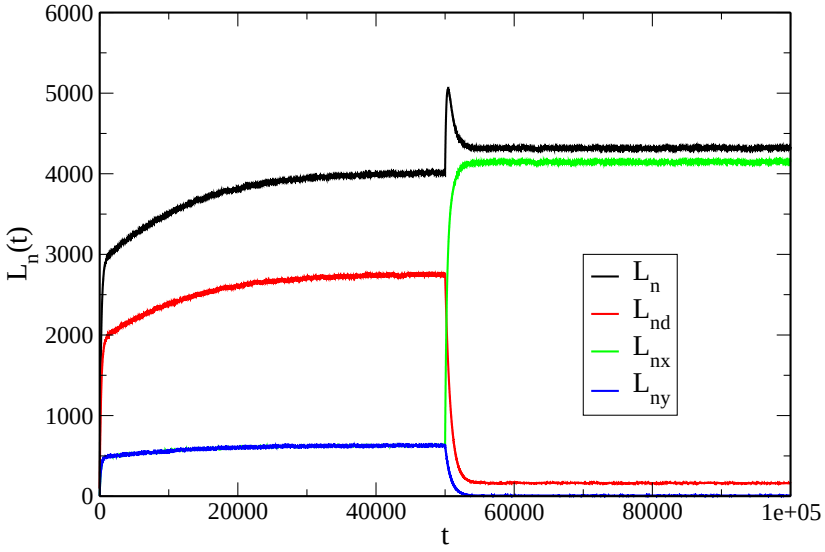

Figure 5.7: For $N^2 = 20^2$, $s = 2$, $\alpha = 0.8$ and 50 realizations, the number of links in x, y and diagonal directions are shown in the graph. The total number of links L_n (black) is increasing after stretching the system. The number of links in diagonal direction, L_{nd}, (red) decreases after the stretch. The number of links in x direction, L_{nx}, (green) increases, because the cell is compressed in x direction and the distance between nodes becomes shorter. The number of links in y direction, L_{ny}, (blue) is decreasing since the cell is stretched in y direction and the distance between nodes is increasing. The initial jump in the total number of links comes from the non-adjusted number of links in y and diagonal directions.

As shown in Figure 5.7, before stretching the cell, there is no difference between L_{nx} and L_{ny} since there is no preference between x and y directions. When the system is stretched, L_{nx} increases and L_{ny} decreases. Because in x direction the distance between nodes decreases, the probability for link creation increases in that direction. So the number of links in x direction increases. In y direction we have the opposite effect. According to Fig. 5.7, right after stretching the cell the total number of links, L_n, is increasing before reaching the new stationary value. This behavior is due to the number of links in y and diagonal directions. These links stay in the system after having stretched the system, and a peak in the total number of links shows up right after the stretch.

The next quantity that has been measured is the distribution of the number of links as a function of the Euclidean distance between two crosslinks. The system is studied before and after stretching the cell. The behavior of this quantity is shown in Fig. 5.8 for $s = 7$ and $N = 5$, $\alpha = 0.2$.

At time $t = T$ the cell is stretched. Before stretching the cell, at time $T - 5$, most of the links are between nearest neighbors due to the large values of s. After stretching the cell, which happens instantaneously, most of the links are distributed between two Euclidean distances. One of them is the distance between nearest neighbors, $r = 0.2$, and the another one is due to long links in y direction with $r = 5$, that are still in the

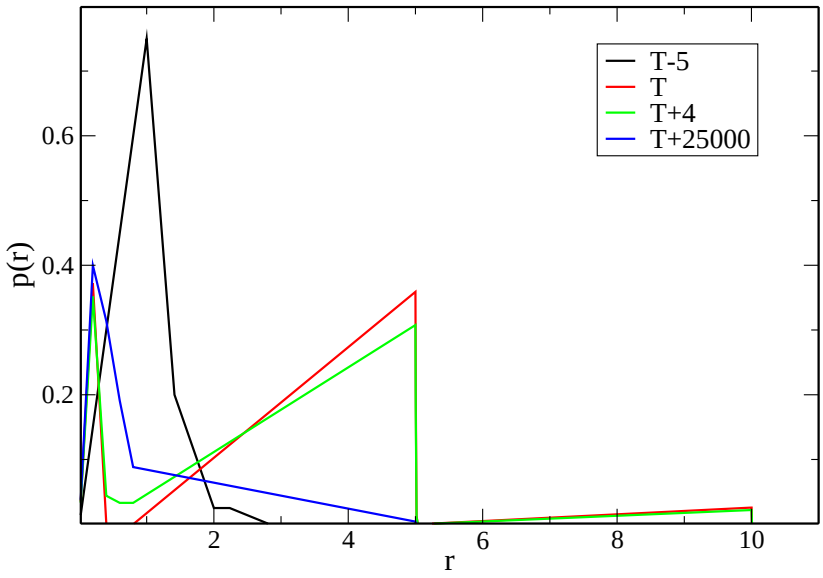

Figure 5.8: For a system with $s = 7$, $N = 5$, and $\alpha = 0.2$, the probability distribution of the links as function of the Euclidean distance, r, is shown. At time $t = T - 5$ (black line), the maximum value of the distribution is at $r = 1$. At time $t = T$ (red line), most of the links are at $r = 0.2$ and $r = 5$. At time $t = T + 4$ (green line), more links are created with short length and longer links are dissolved in the system. At large observation time $t = T + 25000$ (blue line), most of the links have short length.

system immediately after the stretch. As time evolves, the system gets rid of the long links in the diagonal and y directions.Therefore the second peak disappears. In the new stationary state at time $T + 25000$, most of the links are nearest neighbor bonds in the x direction with a length $r = 0.2$.

As seen in Fig. 5.9, for $N = 20$, $s = 3$ and 20 realizations, distribution probabilities look smoother but the general behavior is the same as in Fig. 5.8 [4].

The behavior shown in Fig. 5.8 and 5.9 is very general and is also observed for other values of α. In all cases the very long links in y and diagonal directions are removed and the number of links with length $r = \alpha$ increases.

In tables 5.4, 5.5, and 5.6, we have a closer look at the stationary values for the total number of links, L_n, the number of links in y direction, L_{ny}, and the number of links in diagonal direction, L_{nd}, as functions of time for different values of s and N. Our study shows that the number of links in either of the directions displays a power law behavior before reaching the stationary value. The exponents vary between 2 and 6.

[4] s is small, therefore long and short links co-exist.

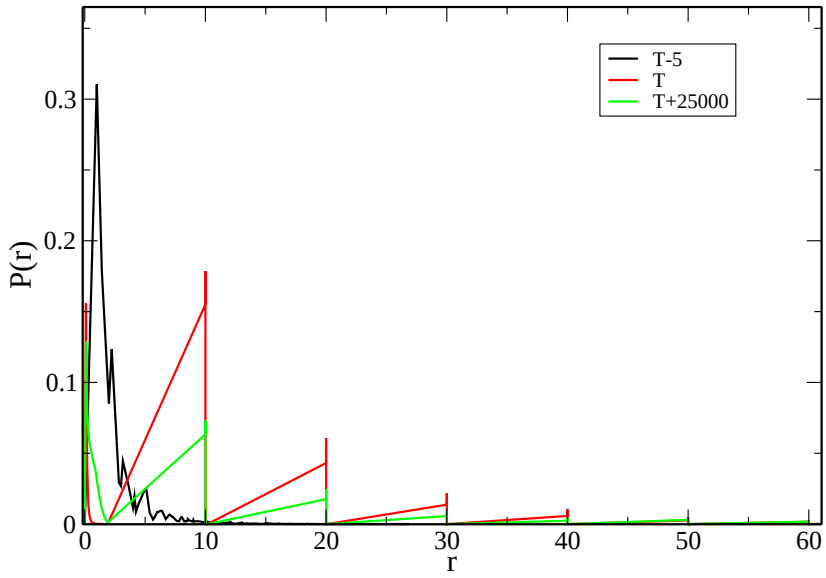

Figure 5.9: Probability distribution of links as function of distance r for $s = 3$, $N = 20$, $\alpha = 0.2$, and 20 realizations. As s is a small value, the links can have both short and long length as shown for $t = T - 5$ (black color). At time $t = T$ (red color), the cell is stretched with $\alpha = 0.2$. At large observation time $t = T + 25000$ (green color) the number of long links decreases.

N/ S	1	2	3	4	5	6	7
5	3.93	3.26	2.94	2.42	2.75	3.01	3.48
10	4.41	4.04	2.68	2.93	3.01	3.35	3.38
20	4.68	4.43	6.26	5.67	4.05	4.4	

Table 5.4: For different number of nodes $N = 5, 10, 20$ and $s = 1, 2, 3, 4, 5, 6, 7$, the total number of links, L_n, is changing as a power law of time with the exponent listed here.

N/ S	1	2	3	4	5	6	7
5	2.42	3.26	2.36	2.45	2.84	2.82	2.94
10	2.73	3.04	2.83	2.81	2.71	2.78	3.2
20	2.03	2.27	2.54	3.24	2.95	3.65	

Table 5.5: For different number of nodes $N = 5, 10, 20$ and $s = 1, 2, 3, 4, 5, 6, 7$, the number of links in y direction, L_{ny}, is changing as a power law of time with the exponent listed here.

5.3.2 Lattice simulation: Shearing the cell

The cell is sheared according to the equation,

$$x' = x + y/\tan(\beta) \qquad y' = y \tag{5.12}$$

N/ S	1	2	3	4	5	6	7
5	3.5	4.01	3.96	4.12	3.87	3.57	3.88
10	4.61	5	4.58	4.13	4.5	4.93	4.06
20	4.93	5.02	5.32	5.29	5.79	5.99	

Table 5.6: For different number of nodes $N = 5, 10, 20$ and $s = 1, 2, 3, 4, 5, 6, 7$, the number of links in diagonal direction, L_{nd}, is changing as a power law of time with the exponent listed here.

x and y are the positions of a node before the shearing, and x' and y' are the positions after the shearing, whereas β is the shear angle with respect to the positive x direction. Here we look at the time evolution of the number of links for $s = 3$, $N = 5$, see Fig. 5.10,

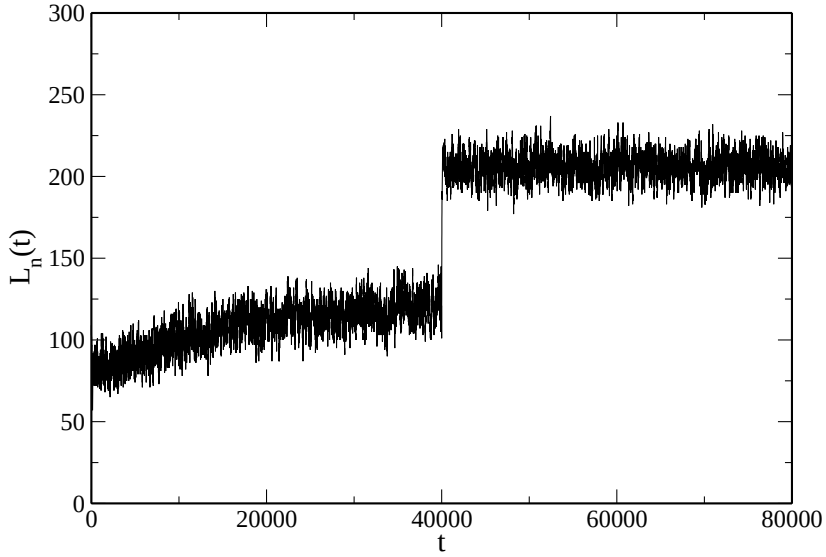

Figure 5.10: The number of links reaches a new stationary value after shearing the cell. Here the data is obtained for $N = 5$, $s = 3$, $\beta = 45$.

The system reaches a new stationary state when the cell is sheared instantaneously at some time. This is generic behavior and does not depend on the specific value of s or N. For various values of s from 0 to 7, the time evolution of L_n is shown in Fig. 5.11, after the system has been sheared at $T = 40000$.

This new stationary values of the number of links is reached very fast, as shown in Fig. 5.11. We measure the probability distribution of the Euclidean distance when shear is applied, see Fig. 5.12 for $N = 5, s = 7, \beta = 45$,

At time $t = T = 40000$, the cell is sheared. Before the shear, most of the links are at Euclidean distance $r = 1$. Right at the shear at time $t = T$, the number of links with $r > 1$ is increasing because of the instantaneous shear. At times $t > T$, the number of links with $r = 1$ is increasing, whereas the number of links at large Euclidean distances decreases. In the new stationary state, links are concentrated at the shortest possible distance. The new stationary values for the number of links depends on the values of the shear angle β, see

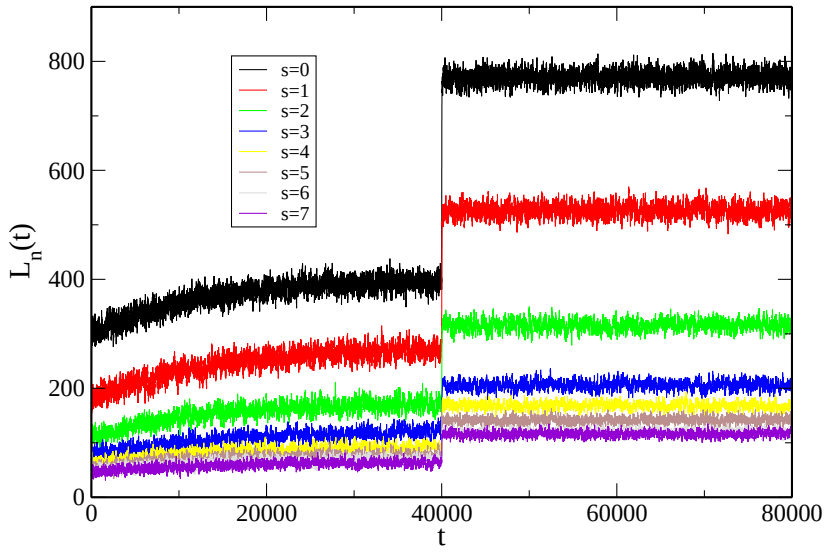

Figure 5.11: For different values of s from 0 to 7 the system reaches different stationary states after shearing the cell.Typically the new stationary state value is characterized by a larger stationary value of L_n.

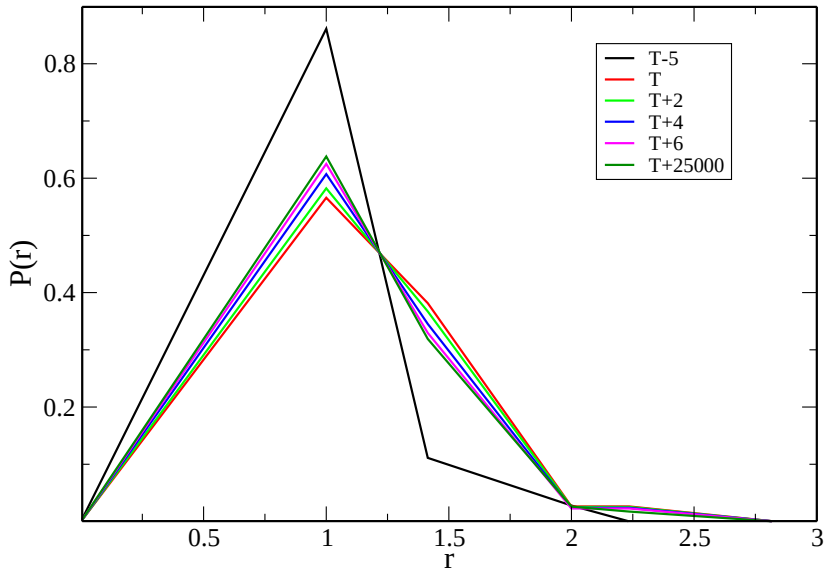

Figure 5.12: As the data show for $\beta = 45$, $N = 5$, and $s = 7$, before the shear at time $T - 5$ and after the shear at time $t > T$, most of the links are nearest neighbor links with $r = 1$.

Fig. 5.13.

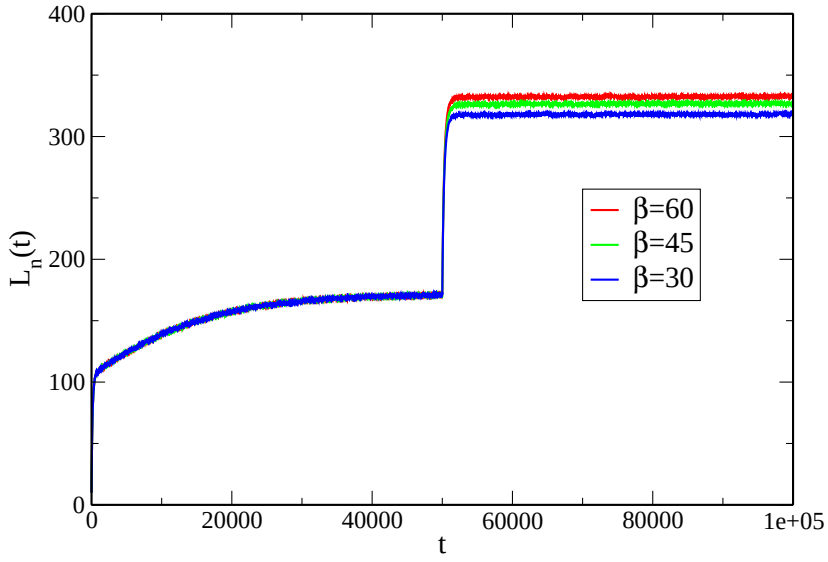

Figure 5.13: For $N = 5$ and $s = 2$, the number of links is plotted as a function of time for different shear angles. The shear angle β is increasing from 30 to 60. The number of links increases when β increases.

5.3.3 Lattice simulation: Returning to the original cell shape

After perturbing the cell, we bring it back to its original state. In reality, CSK will not return to the initial condition, but in our model the cell can recover its initial shape. Let us consider the case where the perturbation was stretching. To return the cell to the original shape, we gradually change the stretching coefficient back to $\alpha = 1$. For the gradual change of α from the perturbed value α_0 back to 1, we use

$$\alpha = (\alpha_0 - 1)\exp((T - t)/T_0) + 1 \tag{5.13}$$

α_0 is the value of α after change. Here T is the time at which we stretched the cell. At the same time α starts to deviate from α_0. T_0 is the typical time constant for changing α back to 1. For different values of s, the number of links in x, y and diagonal directions are different. In Fig. 5.14 (a), results for L_n, L_{nx}, L_{ny}, L_{nd}, with $N = 10$, $s = 4$, $\alpha_0 = 0.1$, are shown.

According to Fig 5.14 (a), right after stretching the cell the distance between nodes in x direction is decreasing and the number of links in x direction, L_{nx}, is increasing. For L_{ny} and L_{nd} we have the opposite behavior. In Fig. 5.14 (b), $N = 10$, $s = 5$, $\alpha = 0.1$, the number of links in the diagonal direction is less than the number of links in the x and y directions.

5.3.4 Off-lattice simulation: Stretching the cell

We want to see the effect of using a lattice. Therefore we also study an off-lattice version of our model. The crosslinks are now chosen randomly inside a two-dimensional cell with a fixed size. In Fig. 5.15, the

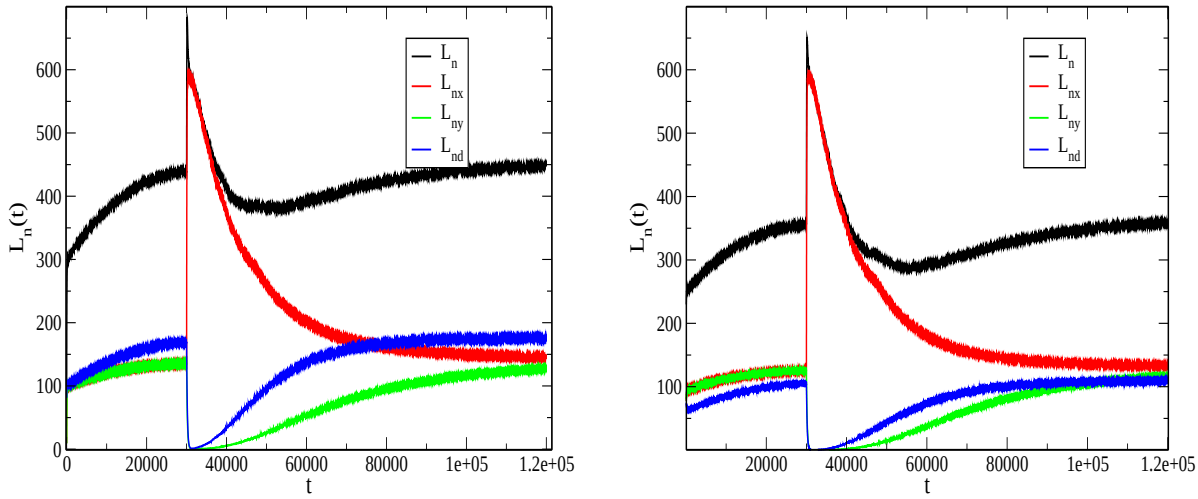

Figure 5.14: (a) For $N = 10$, $s = 4$, $\alpha = 0.1$ and 100 realization, the total number of links (black) and the number of links in x (red), y (green) and diagonal directions (blue) are shown. By gradually changing the stretching coefficient, α, from 0.1 to 1, L_{nx} is decreasing, whereas L_{ny} and L_{nd} are increasing in time. (b) For $N = 10$, $s = 5$, $\alpha = 0.1$ and 100 realization, the total number of links (black) and the number of links in x (red), y (green) and diagonal directions (blue) are shown.

behavior of L_n vs time, for $N = 10$, $s = 7$, $\alpha = 1$ (i.e. we do not change the cell) is shown,

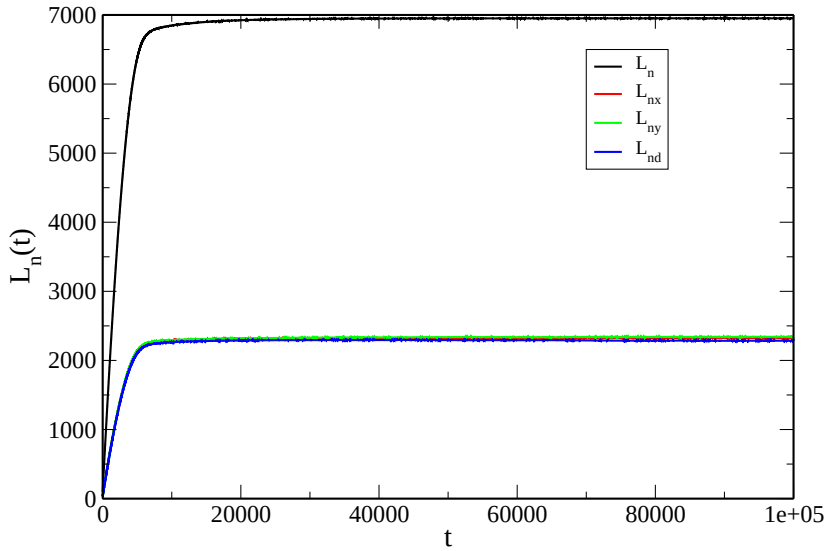

Figure 5.15: For $N = 10$, $s = 7$, $\alpha = 1$ and 1000 realizations, the number of links in x, y and diagonal directions have the same stationary value.

To calculate the number of links in x, y and diagonal directions, we proceed as follows. Each crosslink is considered to be at the center of a circle. The circle is divided into 12 parts and the links in the angle ranges

from $\frac{11}{6}\pi$ to $\frac{\pi}{6}$ and from $\frac{5}{6}\pi$ to $\frac{7}{6}\pi$ are counted as L_{nx} links. Links in the region with the angles from $\frac{\pi}{3}$ to $\frac{2}{3}\pi$ and from $\frac{4}{3}\pi$ to $\frac{5}{3}\pi$ are L_{ny} links. Links in the rest of the circle are considered as L_{nd}. As we see from Fig. 5.15, the number of links in x, y and diagonal directions reach to the same stationary value.

We also studied the stretching of the cell for this off-lattice situation. In figure 5.16 we show data where we stretched the cell with $N = 10$, $s = 7$ and $\alpha = 0.2$ at time $T = 50,000$.

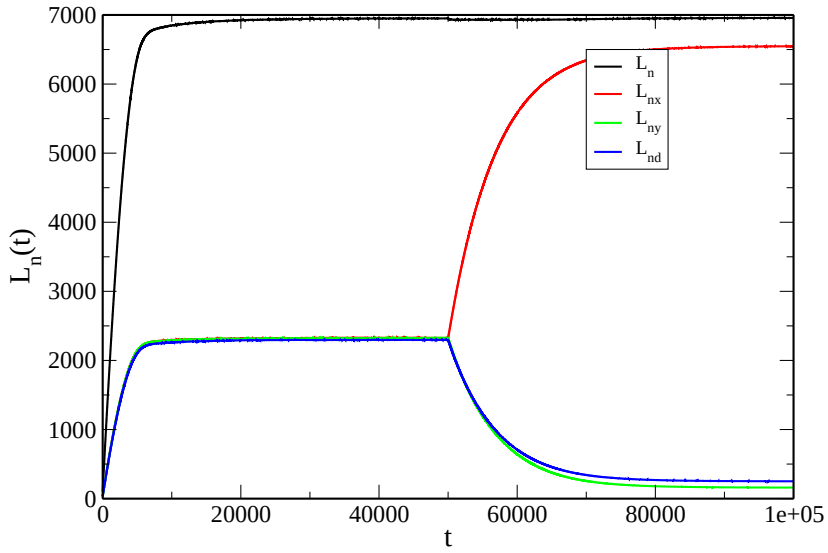

Figure 5.16: In the off-lattice case for $N = 10$, $s = 7$, $\alpha = 0.2$ and 1000 realizations, the number of links in x, y and diagonal directions reach to the same stationary value.

The trend we observe is similar to what we have seen in the on-lattice simulations of section 5.3.1, see figure 5.7. The only difference can be found in the absence of the initial shock right after stretching the cell. In the on-lattice simulations it takes time to adapt the length of the segments to the new geometry of the cell. But in off-lattice simulations this is not the case.

5.3.5 Off-lattice simulation: Returning to the original cell shape

In the figures 5.17, 5.18 and 5.19, the variation of number of links for different values of T_0 is shown where in the off-lattice simulation we change α from $\alpha_0 = 0.2$ back to 1. In all the cases, $T = 50000$. In Fig. 5.17, the number of links in each direction is shown for $T_0 = 5000000$.

The number of links in Fig. 5.17 is not showing much difference with the results obtained for a system with constant α in Fig. 5.16. If T_0 is of the same order as $T = 50000$, the system is showing a different behavior when comparing with the $T_0 \gg T$ case shown in Fig 5.17. Fig. 5.18 displays data for $T_0 \sim T$.

By changing α, the number of links in x direction is decreasing while the numbers of links in y and diagonal directions are increasing. The data show that by extrapolating the red, blue, and green lines, we reach to one stationary value for the numbers of links in the three different directions. For the small value of $T_0 = 500$ and $T = 50000$, shown in Figure 5.19, we see, that the numbers of links in the three different directions

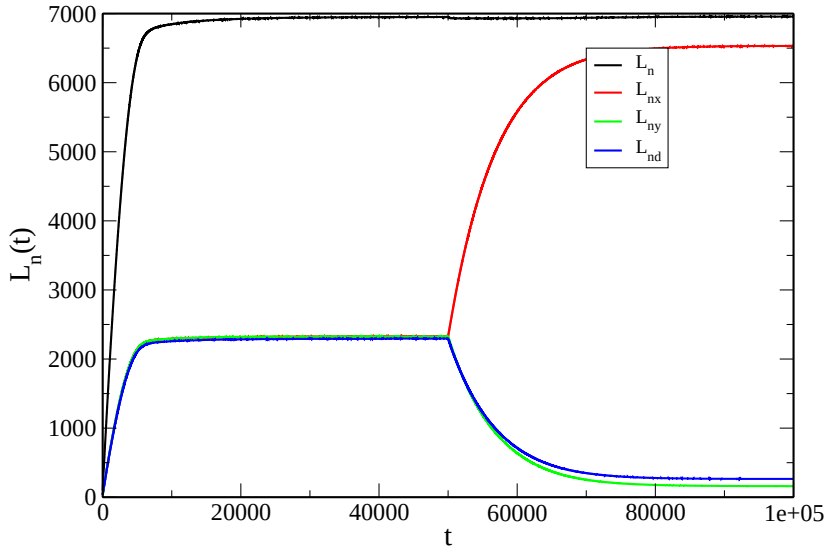

Figure 5.17: For $N = 10$, $s = 7$, $\alpha_0 = 0.2$, $\alpha = 1$ and 1000 realizations, the numbers of links in x, y and diagonal directions are changing very slowly when changing α from 0.2 back to 1. Here $T_0 \gg T$, as $T = 50000$ and $T_0 = 5000000$.

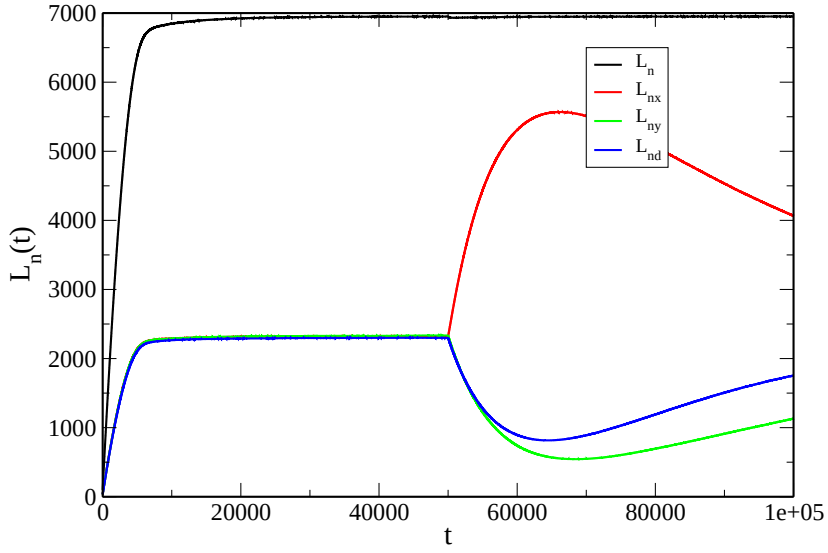

Figure 5.18: For $N = 10$, $s = 7$, $\alpha_0 = 0.2$, $\alpha = 1$ and 1000 realizations, the numbers of links in x, y and diagonal directions are changing slowly when changing α from 0.2 back to 1. Here $T_0 \sim T$, as $T = 50000$ and $T_0 = 50000$.

reach very fast to the same stationary value.

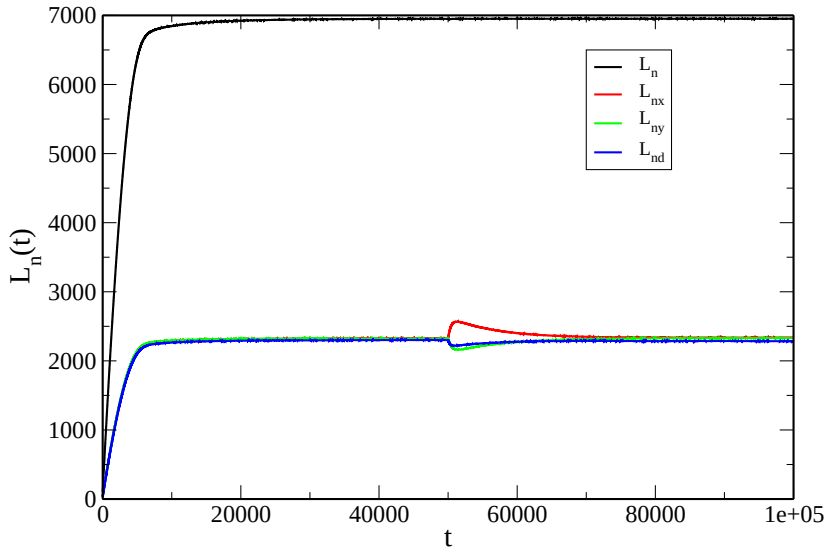

Figure 5.19: For $N = 10$, $s = 7$, $\alpha_0 = 0.2$, $\alpha = 1$ and 1000 realizations, the numbers of links in x, y and diagonal directions are changing very fast when changing α from 0.2 to 1. ($T \gg T_0$ and $T = 50000$ and $T_0 = 500$)

Chapter 6

Three-dimensional realistic model of the cytoskeleton

When studying the dynamics of the cytoskeleton, three-dimensional polymer based models capture better the physics of the system than two-dimensional models. The two-dimensional model discussed in chapter 5 study very basic elements of the network of the cytoskeleton. Here, we study a cytoskeleton model in three-dimensional space where we include important polymer aspects of the real network. This model is studied by Monte Carlo simulations, and the aging of the system is investigated. Our theoretical study closely follows the steps in recent experiments [117, 118].

Here we describe the main aspects of our model. At first, nodes or crosslinks are placed inside a three-dimensional box with periodic boundary conditions (PBC) on each side. Then following the rules from ref. [125], four individual segments are assigned to each crosslink, which yields a four-fold-connected network consisting of N nodes and $2N$ links, thereby creating a fully connected network.

To each of the segments we assign a polymer length taken from the distribution of semiflexible polymers [123] described in chapter 6.3. We chose to model an actin network as actin polymers participate in the mechanical response of the cell and hence provide strength to the cell. Actin polymers are semiflexible filaments and thus they are not flexible enough to follow the rules of the Worm-Like-Chain (WLC) model [90] and are not strong enough to behave as rigid rods. The contour length in the semiflexible network is close to the Euclidean length of the segment. The initial connected network of segments becomes thus a long entangled filament. As this initially created network is out of equilibrium, we are relaxing the system using the Monte Carlo method in order to reach the stationary state. The time to reach to the stationary state depends on the system's parameters such as the number of crosslinks, the persistence length of the polymer, and the filament concentration. This relaxation is achieved through a Monte Carlo move called rewiring that will be described in section 6.6.

In order to have a network similar to the actin network, that consists of different filaments, the initial entangled filament is chopped into smaller pieces until we reach the desired number of filaments. Finally, in order to fully relax the system, we allow for two additional Monte Carlo moves, called relabeling and shifting nodes, which are described in section 6.7. Shifting a node is a realistic move which is similar to the behavior of motor proteins that act as crosslinkers and move along the attached filaments.

Similar to what is done in the experiment, we apply a mechanical perturbation to the system. While the system is then relaxing to a new stationary state, we monitor the dynamics of the network through the measurement of two time quantities. In the rest of this chapter, we discuss our Metropolis algorithm as well as details of the model.

6.1 Metropolis algorithm

Monte Carlo Methods, where conformation changes are modeled as a Markov chain, are widely used in Statistical Mechanics [119]. Starting from the current state of the system, a new state is proposed and accepted with a certain transition probability. The proposed move is always accepted when the energy of the proposed state is less than the energy of the current state. If that is not the case, then the new state is added to the Markov Chain with rate $e^{-\beta\Delta E}$ where ΔE is the change in energy. The Metropolis criterion for the acceptance of an event is therefore:

$$P_{accept} = \min(1, \exp(-\beta\Delta E)) \tag{6.1}$$

In our three-dimensional model of the cytoskeleton, we allow for three different kinds of Monte Carlo moves. The first update scheme is rewiring of the long entangled filament. After that we cut the long filament into the desired number of small filaments and let the system relax through relabeling and shifting nodes.

6.2 Creation of a fully connected network

We start by randomly placing crosslinks in a three-dimensional box as shown in Fig. 6.1. To create the four-fold-connected network, we first choose three nearest nodes in our list of crosslinks and connect them. The whole network is created by adding one segment at a time to the already connected segments by using specific rules. At each time step we choose two crosslinks where one of the two nodes has to be part of the network, called old node, *A*, whereas the newly chosen node is called new node, *B*. Then one segment connected to the old node and closest to the new node is deleted. The other end of the deleted segment, *C*, should not already be connected to the new node, *B*. Then two new segments, *AB* and *BC*, are created, as shown in Fig. 4.2. Following these rules we let the network grow until the total number of links equals two times the number of crosslinks. Therefore, each crosslink is connected to four links and each link has been created just one time.

Following the network creation rules in Fig. 6.2, there are some cases that are not allowed during the network creation, see Fig. 6.3. Fig. 6.3 (a) shows the case of two crosslinks *A* and *B* that are already connected. Fig. 6.3 (b) shows two nodes, *A* and *B*, that have common neighbors, *C* and *D*. By choosing nodes *A* and *B*, there is not any possible link to delete. Fig. 6.3 (c) considers a case with only one possible segment to delete, namely the segment *AC* which is not necessarily the closest segment to the new node, *B*. We can not choose the segment *AF* for deletion as this would result in having the presence of *BF* twice in the segment list as shown in Fig. 6.3. In case we can delete a segment, then the new node will always add two new segments.

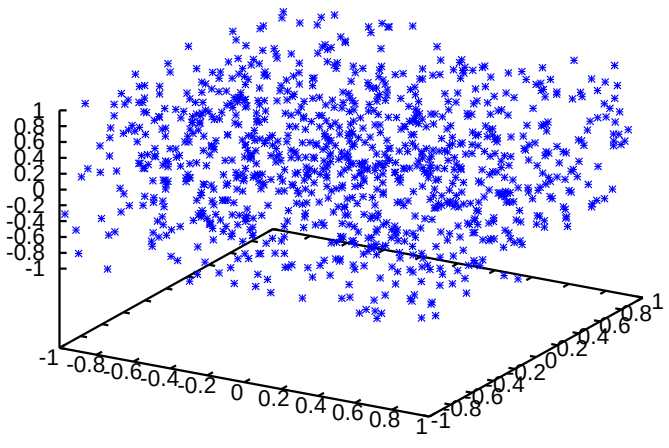

Figure 6.1: All the crosslinks are inside the original box.

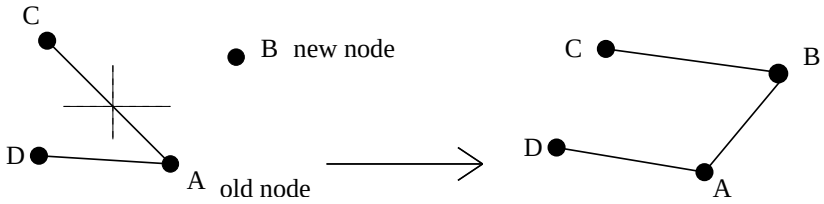

Figure 6.2: At each time step the nearest segment, *AC*, to the new node, *B*, is deleted and two new links, *AB* and *BC*, are created.

The degree[1] of the old node, *A*, does not change but the degree of the new one, *B*, increases by two. In this procedure some of the segments can be created and deleted more than once.

At the end each crosslink is connected to four segments. Figure 6.4 shows a schematic picture of the final four fold connected network.

In the next step we are assigning to every segment a polymer length taken from the distribution function given in [123].

6.3 Assignment of polymer length

The polymer distribution function, $G(\vec{R};L_c)$, is the main quantity for characterizing a single polymer. $G(\vec{R};L_c)$ provides the probability to find a polymer of contour length L_c for fixed end-to-end $\vec{R}$ and given persistence length l_p. For the semiflexible polymer that results from the wormlike chain model with short

[1]Degree of a node is the number of segments connected to the node.

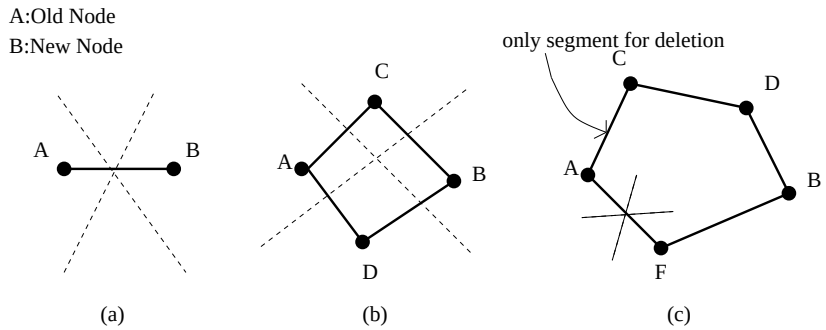

Figure 6.3: There are some cases that are not allowed. (a) Old node, *A*, and new node, *B*, should not already be connected. (b) Old node and new node should not be connected to common neighbors, as then one would not have a segment to delete. (c) Segment chosen for deletion should not be connected to any of the segments connected to new node. Here *AC* is the only allowed segment, as its deletion allows us to add two new segments, *BC* and *AC*.

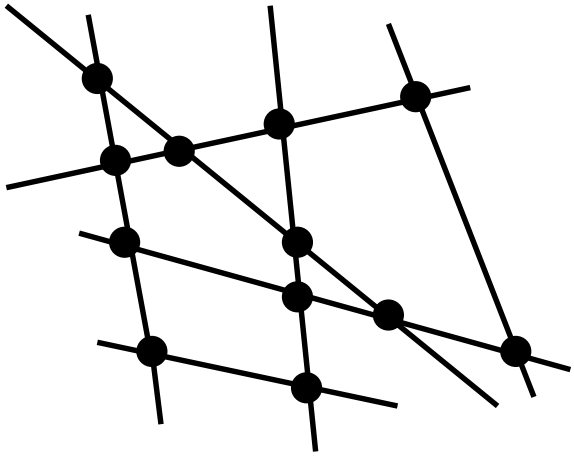

Figure 6.4: Schematic picture of final network. There are four links connected to each crosslink.

range interaction, $G(\vec{R};L_c)$ gives the probability to find two of the monomers at the distance $\vec{R}=\vec{R}(s)-\vec{R}(s')$ where the distance between two monomers along the chain is $L_c=|s-s'|$. For a freely jointed phantom chain [2] $G(\vec{R};L_c)$ is known from [135] and is approximately described by a simple Gaussian. When including self-avoidance, the calculation of the distribution is more complex. This distribution of the wormlike chain is calculated for large $t=L_c/l_p$ by adding higher terms to the Gaussian distribution [136, 137]. The exact distribution has been obtained in Wilhelm's paper [123] (for not too large t). The first three moments can be obtained analytically [138], whereas higher moments can be computed numerically [139]. When the contour length is of the same order as the persistence length of the polymer, $L_c/l_p\sim 1$, the distribution function shows different behavior than for flexible polymers. The authors of [123], through analytical calculation and a numerical Monte Carlo study of the distribution, provide a better understanding of the semiflexible polymer conformations. The analytical equation is

[2] A phantom chain is an ideal chain in polymer physics where segments can overlap with each other.

$$G(\vec{R};L_c) \approx \frac{l_p}{\mathcal{N}L_c^2} f(\frac{l_p}{L_c}(1-|\vec{R}|/L_c)), \tag{6.2}$$

$$\text{where } f(x) = \begin{cases} \frac{\pi}{2}\exp[-\pi^2 x] & \text{for} \quad x > 0.2 \\ \frac{1/x-2}{8\pi^{3/2}x^{3/2}}\exp[-\frac{1}{4x}] & \text{for} \quad x < 0.2 \end{cases}$$

$|\vec{R}|$ is the end-to-end distance, L_c is the contour length, l_p is the persistence length, and $\mathcal{N}$ is a normalization factor. This distribution is valid for $L_c \lessapprox l_p$, $x \lessapprox 0.5$ in three-dimensional space. The radial distribution of polymers is one of the observable quantities in fluorescence microscopy [140, 141, 142].

The distribution function, $G(r)$, is plotted as a function of the Euclidean distance $r = |\vec{R}|$, in Fig. 6.5 as obtained from Monte Carlo simulation, see the dashed lines. Curves obtained from Eq 6.2 are also shown by solid lines. There is a good agreement between numerical and analytical results for each case.

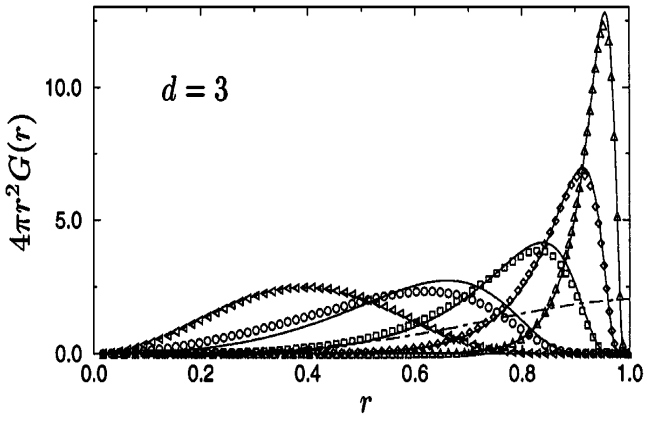

Figure 6.5: Analytical equation and Monte Carlo simulation of $G(r)$ plotted vs r. For different values of $L_c/l_p = 10, 5, 2, 1$, and 0.5 the maximum is shifted from right to left. Solid lines are obtained from Eq. 6.2 for the provided ratio and the dashed lines are Monte Carlo simulation results (Reprinted figure with permission from [123]. Copyright (1996) by the American Physical Society.)

To assign a contour length to each segment in the network, we use the distribution given in equation 6.2. For each Euclidean distance in the network, we choose one possible contour length at random. The probability distribution shown in Fig. 6.5 is a very steep function. A schematic picture of the assigned polymer length is shown in Fig. 6.6.

After a polymer length has been chosen for each Euclidean distance, we end up with a network that is a long entangled filament.

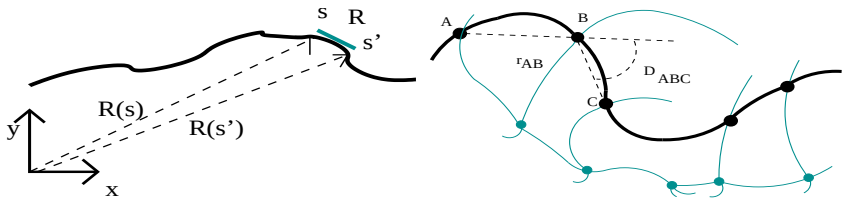

Figure 6.6: (a) For each segment, a contour length is assigned. (b) At the end there is a long entangled filament.

6.4 Energy of the system

The energy of the system consists of two parts:

$$\beta E = \sum_i \frac{\mu}{2}(|\vec{r}_i| - |\vec{r}_{0i}|)^2 + \sum_{i,j} \frac{l_p}{L_{c,i} + L_{c,j}} \theta_{ij}^2 \tag{6.3}$$

$$\beta = k_B T$$

The first term corresponds to the stretching energy calculated from Hooke's law and the second term is bending energy that results from the connection of two segments belonging to the same filament. $|\vec{r}_i|$ is the actual Euclidean length of the segment, whereas $|\vec{r}_{0i}|$ is the Euclidean length of the segment in the stationary state. μ is the stretching coefficient, θ_{ij} is the angle between segments i and j, l_p is the persistence length, and $L_{c,i}$ is the polymer contour length. Fig. 6.7 shows the two neighboring segments and the angle between them.

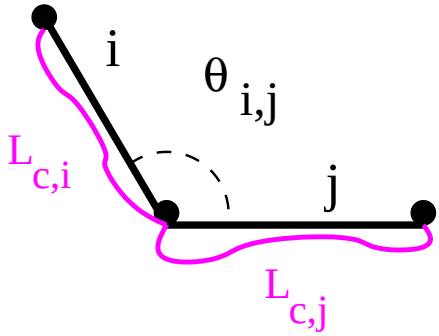

Figure 6.7: Two segments i and j are connected to each crosslink. The angle between segment i and j is $\theta_{i,j}$, and $L_{c,i}$ and $L_{c,j}$ are contour lengths assigned to segment i and segment j respectively.

In the initial relaxation process, the system is in viscous phase and there is no elastic energy. Therefore we consider just the bending energy for that process.

6.5 Rewiring

Rewiring is the only Monte Carlo move that is done in order to relax the long entangled initial filament. As it is shown in Fig. 6.8, three segments, *AB*, *BC*, and *CD*, are picked randomly such that the segments *AC* and *BD* do not exist before this move. Then with Metropolis rate two of the segments, namely *AB* and *CD*, are deleted and two new segments, *AC* and *BD*, are added.

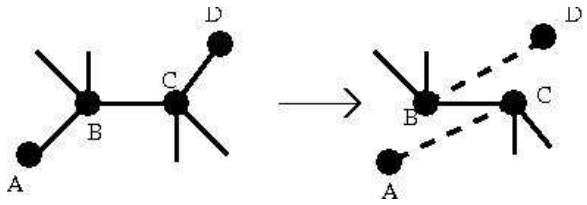

Figure 6.8: Two old links, *AB* and *CD*, are deleted and two new ones, *AC* and *BD*, are created.

To compute the energy, we need all angles for each crosslink. Therefore, we need 12 angles to describe the bending energies of the current and the proposed configurations.

6.6 Chopping the initial filament

The actin network consists of different filaments. To reach the desired number of filaments, our initial filament has to be chopped. This is shown in Fig. 6.9(a). At the end of rewiring, the network is still a connected network. That means we can go from each node to every other node by following the filaments. Fig. 6.9 (b) shows a connected network model, whereas Fig. 6.9 (c) shows a disconnected model.

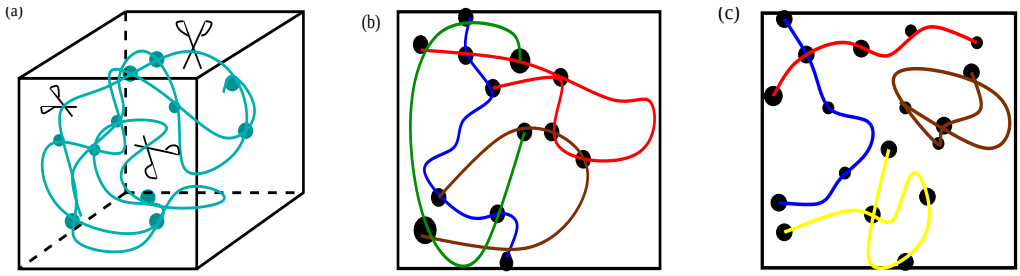

Figure 6.9: (a) The initial long entangled filament is chopped into smaller filaments until the desired number of filaments is reached. (b) By following the filaments, we can go from each node to every other one. (c) There are some filaments which are not connected anymore.

As can be seen in Fig. 6.9 (b), the connected network model has three- and four-fold connected crosslinks. In the disconnected model however, nodes can be one or two fold connected. Therefore one-fold and two-fold connected crosslinks show up when separating filaments in the network. In Fig. 6.10, the different node types are shown.

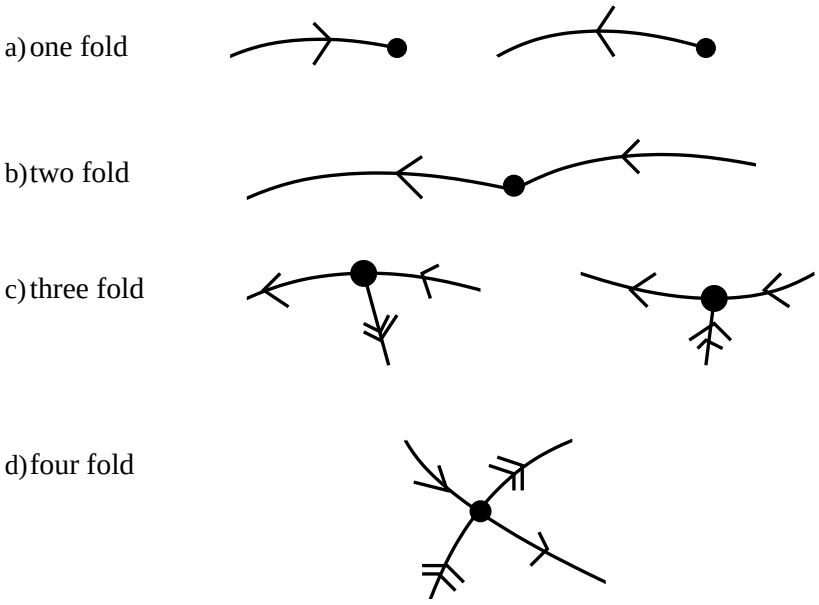

Figure 6.10: (a) One-fold-connected crosslinks can be end points or initial points of a filament. (b) A two-fold-connected crosslink is a regular point that is a connection node between two segments of one filament. (c) A three-fold-connected crosslink involves two different filaments. One filament is indicated by a single arrow, and the other one is indicated by a double arrow. For the single arrow filament, the shown crosslink is a regular point and for the double arrow filament it is an end or initial point. (d) A four-fold-connected crosslink is a regular point for two different filaments.

6.7 Relabeling and shifting nodes

After creation of the desired number of filaments, the system should relax towards the new stationary state. In order to do that, we propose two different moves. One of them is called relabeling and the other one is called shifting nodes. In the algorithm each one of the moves is chosen randomly with the same probability.

6.7.1 Relabeling

In the relabeling update, a node is selected randomly. Each crosslink in the network connects two different filaments. By switching two tails of two filaments, we propose a new conformation for the system. This new conformation is accepted or rejected by using Metropolis rate. To calculate the energy of the conformation, there are four segments and three angles involved, see Fig. 6.11 (a).

In Fig. 6.11 (b) the two chosen filaments are represented with dashed and solid lines. There are two angles entering the calculation of the energy, $AOB = \theta_1$ and $DOC = \theta_2$. When we change the two tails of the filaments, the new angles are *AOC* and *DOB*. To update the configuration, we use Metropolis rate.

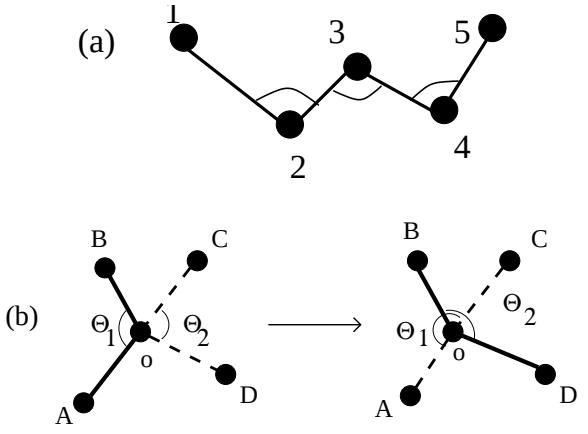

Figure 6.11: (a) For the energy calculation four segments and three angles are needed. (b) A four-fold-connected crosslink is chosen randomly. The solid line is one filament and the dashed line is another one. *AOB* and *DOC* are the angles for the two filaments. With the Metropolis rate, the two tails of the two filaments are switched. The new assigned filaments'angles are *AOC* and *DOB*.

6.7.2 Shifting Nodes

In this step, a node is selected randomly. Then the current bending energy is calculated. Next the coordinates of the chosen node will be moved by the distance $0.05 l_p$ (l_p is the persistence length). As the position of the chosen node is changed the bending energy of the new conformation is changed as well, as shown in Figure 6.12.

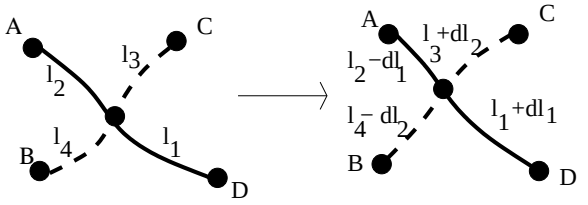

Figure 6.12: Node *O* is chosen randomly. The coordinates will change by $0.05 l_p$. A new polymer length will be assigned to each of the changed segments.

6.8 Measuring a two-times function

When the system is in the stationary state, a mechanical perturbation is added to the system. This perturbation can be different type of strains. Examples are shown in Fig. 6.13;

We shear the cell at time $t = 0$ and then measure two-times function. The perturbation can be instantaneous or spread over time. We follow Edwards and Lee's rule [124] to shear the cell with periodic boundary conditions. The two time function,

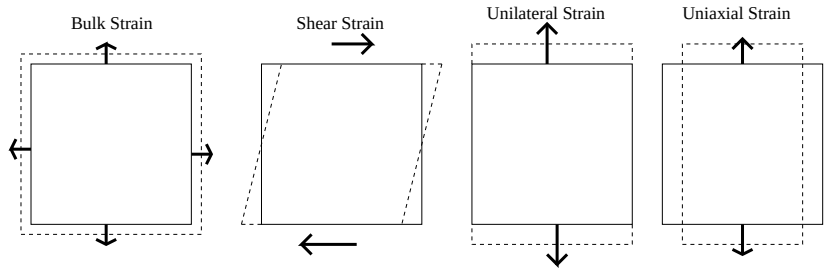

Figure 6.13: There are four types of perturbations: bulk, shear, unilateral and uniaxial strains.

$$\phi(t,s) = <\phi(t)\phi(s)> - <\phi(t)><\phi(s)> \tag{6.4}$$

depends on the observation time t and on the waiting time s. ϕ can be the Euclidean distance between two crosslinks, the global energy or the crosslink density, all considered as functions of different system parameters such as persistent length, l_p, filament density and shear angle. As can be seen in Fig. 6.14, the Euclidean distance between two crosslinks is changing with time,

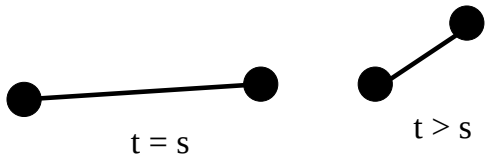

Figure 6.14: Each Euclidean distance can grow or shrink during time.

To assign a density function to the system, we choose a circle with radius $0.1l_p$ centered around each crosslink. Each node can move from the center and at large observation time can go out of the circle. This is illustrated in Fig. 6.15.

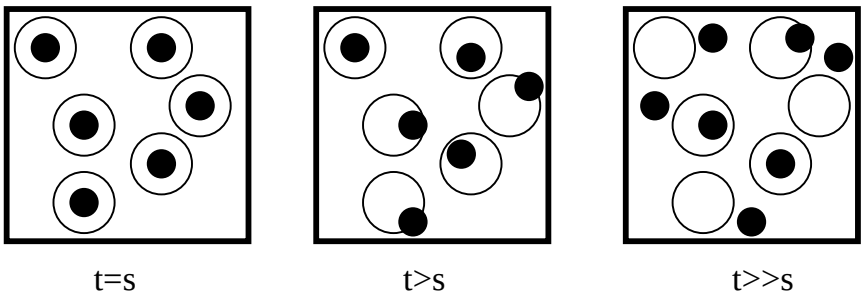

Figure 6.15: Crosslinks at time $t = s$ are in the center of a circle with radius $0.1l_p$. At later times, crosslinks moving in the cell can move outside of the assigned circles. At time $t \gg s$, most of the crosslinks are no longer in the initial circles.

Chapter 7

Two-times functions in the three-dimensional cytoskeleton

In order to gain a better understanding of aging processes in the cytoskeleton, we run simulations for various values of the persistence length, l_p, the number of filaments, f, and the angle corresponding to shear perturbation. I will first discuss briefly shear perturbation in section 7.1. Then in section 7.2, I study the average Euclidean distance as a function of time. Results for the density and Euclidean distance two-times functions are presented in sections 7.3 and 7.4.

7.1 Shear perturbation

To perturb the cell we apply an instantaneous shear that conserves the volume of the cell. During the perturbation each crosslink is shifted according to Eq. 4.11. Therefore some of the polymers will be stretched and some of the others will buckle. There are some polymers that do not show any change in length. A schematic picture of the cell before and after the shear is given in figure 7.1.

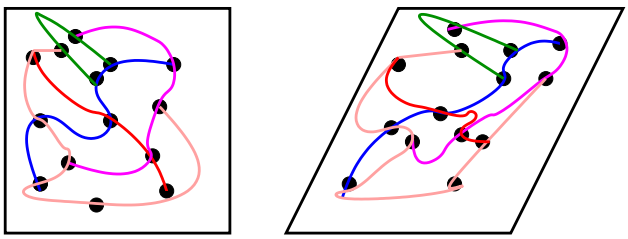

Figure 7.1: The cell is brought out of equilibrium at time $t = 0$ when it is sheared. The shear angle is kept constant when measuring the two-times functions. After the shear the system relaxes to a new equilibrium state. Some polymers, like the blue colored one, are stretched. The red colored polymer is buckled and the green colored polymer does not show any changes. The magenta and pink colored polymers are stretched and buckled in some parts.

Keeping the shear angle constant after the initial change, the system relaxes to a new equilibrium state. During this relaxation process we measure the density and Euclidean distance two-times functions.

7.2 Coarse-grained length as a function of time

In our model, we measure the average Euclidean distance, $< R(t) >$, between nodes at each time step. This length is representative of the average distance between crosslinkers of two different filaments. $< R(t) >$ is shown in Fig 7.2 as a function of time t for the persistence length $l_p = 0.1$, the number of filaments $f = 4$, the number of crosslinks $m = 30$, the stretching coefficient $\mu = 10$, and the shear angle $\alpha = 60$,

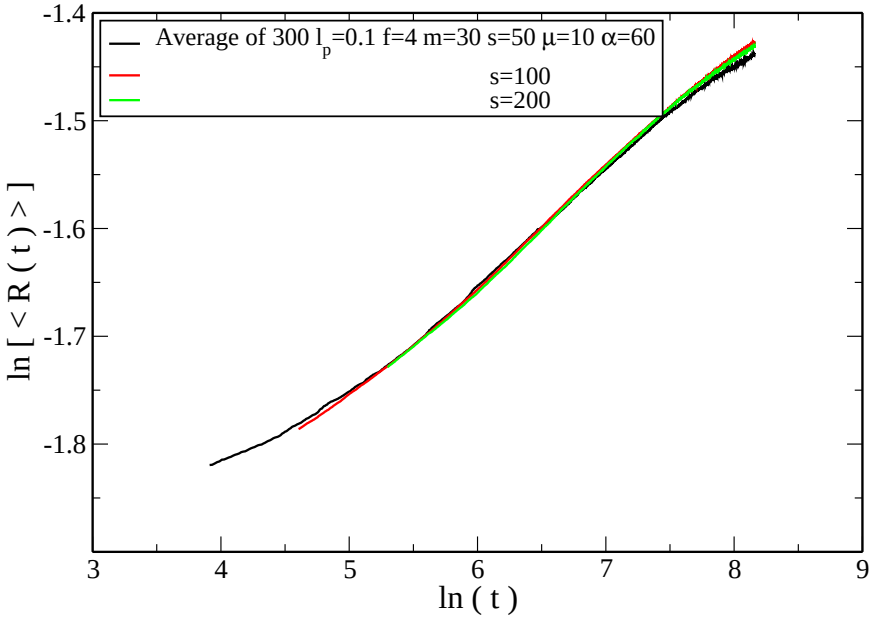

Figure 7.2: For $l_p = 0.1$, $f = 4$, $m = 30$, $\mu = 10$, and $\alpha = 60$, the average Euclidean distance at each time step $< R(t) >$ is plotted vs t.

The average Euclidean distance is found to have a regime where it is approximately given by a power law of time,

$$< R(t) > \sim t^{\xi} \tag{7.1}$$

where the value of the exponent ξ depends on the studied case. The value that we extract from the data for $l_p = 0.1$, $f = 4$, 8, and 12, $m = 30$, $\mu = 10$, and $\alpha = 60$ is $\xi \approx 0.1$. The log-log plot in Fig. 7.2 shows that the slope is changing over time. For larger time, the slope, and therefore the effective exponent, changes from 0.1 to 0.08. This shows that the system's dynamics is slowing down for larger times, presumably due to finite-size effects. [1]

[1]The exponent also changes roughly by 0.02 for other studied cases.

For other cases such as $l_p = 1$ and 10 with $f = 8$, $m = 30$, and $\alpha = 60$, the average Euclidean distance is displaying an additional regime at short times, see Fig. 7.3 and 7.4. These two figures show that for larger values of the persistence length the system takes longer to reach the regime characterized by an algebraic growth law.

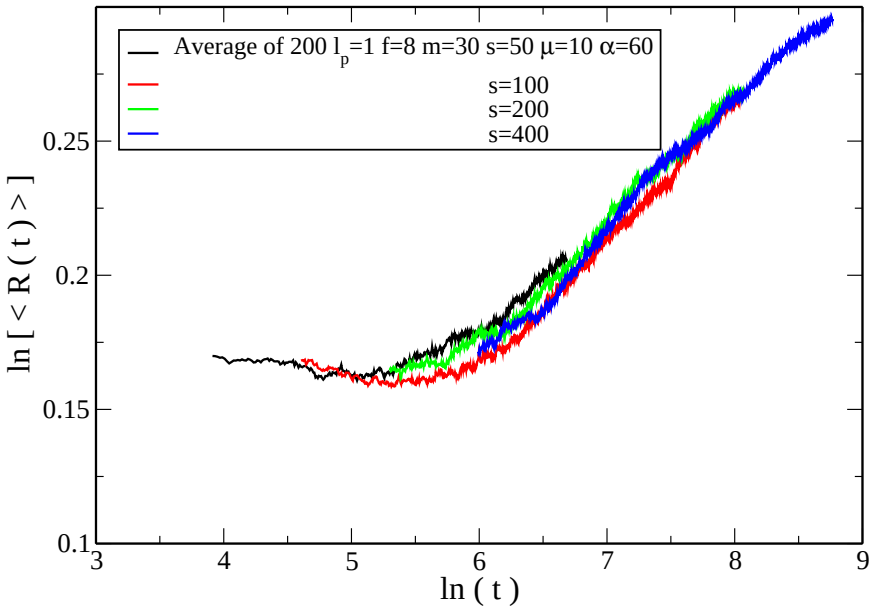

Figure 7.3: For $l_p = 1$, $f = 8$, $m = 30$, $\mu = 10$, and $\alpha = 60$, the average Euclidean distance $< R(t) >$ as a function of t displays an initial time regime before algebraic growth sets in.

For the system with $l_p = 1$ for large values of the waiting time, see Fig. 7.3, we find the value $\xi \approx 0.04$ in the algebraic growth regime. However for $l_p = 10$ shown in Fig 7.4 we could not reliably measure the exponent from the existing data. Still our data suggest that the exponent will be less than the exponent obtained for the case with $l_p = 1$.

7.3 Density two-times function

The density two-times function is revealing the dynamics of the crosslinks in the system. To measure the density two-times function, we follow the rules given in Fig. 6.15. The two-times density function is given by the expression,

$$C_n(t,s) = \frac{1}{N}\sum_{i=1}^{N} \phi_i(t)\phi_i(s) \tag{7.2}$$

N is the total number of crosslinks, where the crosslink i is characterized by the variable ϕ_i that can take on the values 0 or 1. $\phi_i = 1$, if the crosslink is still inside a sphere with radius $r = 0.1 l_p$ drawn around its position at the moment of the shear, and $\phi_i = 0$, if this is no longer the case. Results for the persistence

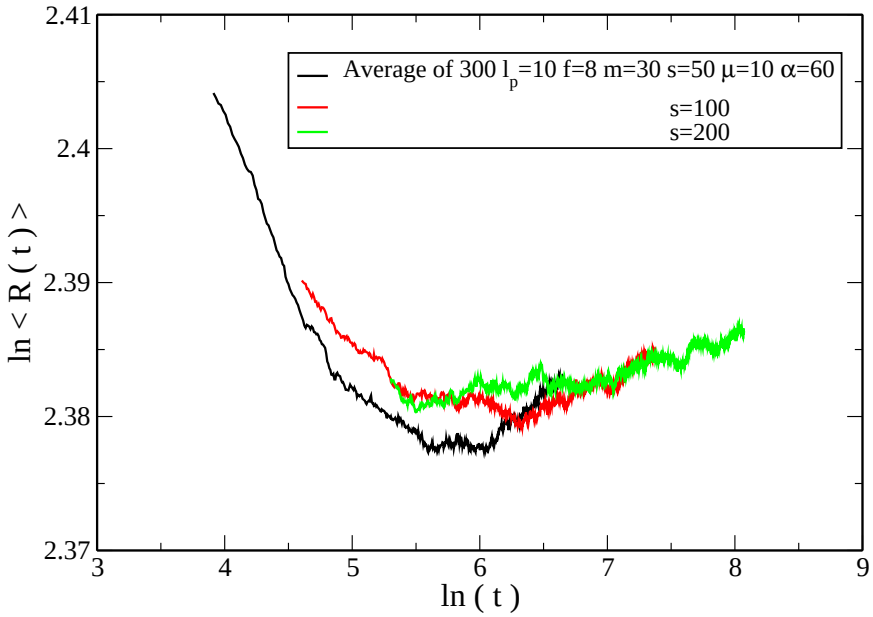

Figure 7.4: For $l_p = 10$, $f = 8$, $m = 30$, $\mu = 10$, and $\alpha = 60$, the average Euclidean distance at each time step $< R(t) >$ is plotted vs t.

length $l_p = 0.1$, the number of filaments $f = 4$, the number of crosslinks $m = 30$, the stretching coefficient $\mu = 10$, and the shear angle $\alpha = 60$ are shown in Fig. 7.5.

The panels in Fig. 7.5 are showing the density autocorrelation function as a function of $t - s$ and $\ln(t - s)$. Three different regimes are clearly visible in Fig 7.5(b). In the first regime, the system with smaller waiting time, $s = 50$ (black line), has a faster dynamics than the older systems with larger waiting times ($s = 100$ and 200). After a crossover, the older systems now decay slower, yielding a regime where aging is observed. In the final regime, the decay of the correlation becomes very slow. Some crosslinks remain trapped close to the position they had at the moment of the shear (at time s). To further study the density autocorrelation function of the system, we plot the data as a function of t in Fig.7.6(a). In Fig. 7.6(b) the data is plotted as a function of the ratio t/s.

We study the dynamical scaling of $C_n(t,s)$ vs t/s in Fig. 7.7. The measured dynamical exponent is $b = -0.107$. The simple scaling behavior is rather well respected by the data. We also plotted the density autocorrelation function as a function of the average Euclidean distance at each time step, $< R(t) >$, see Fig. 7.8(a). In Fig. 7.8(b), we plot the same data vs $< R(t) > / < R(s) >$ for each waiting time [41, 42].

As the data in Fig. 7.8(a) and (b) are showing, there are two regimes for this system. Furthermore, the data nicely follow the generalized simple aging scaling discussed in [41, 42] as shown in Fig. 7.9, with the dynamical exponent $b = -1.72$. This generalized scaling form works much better than the standard aging scaling shown in Figure 7.7.

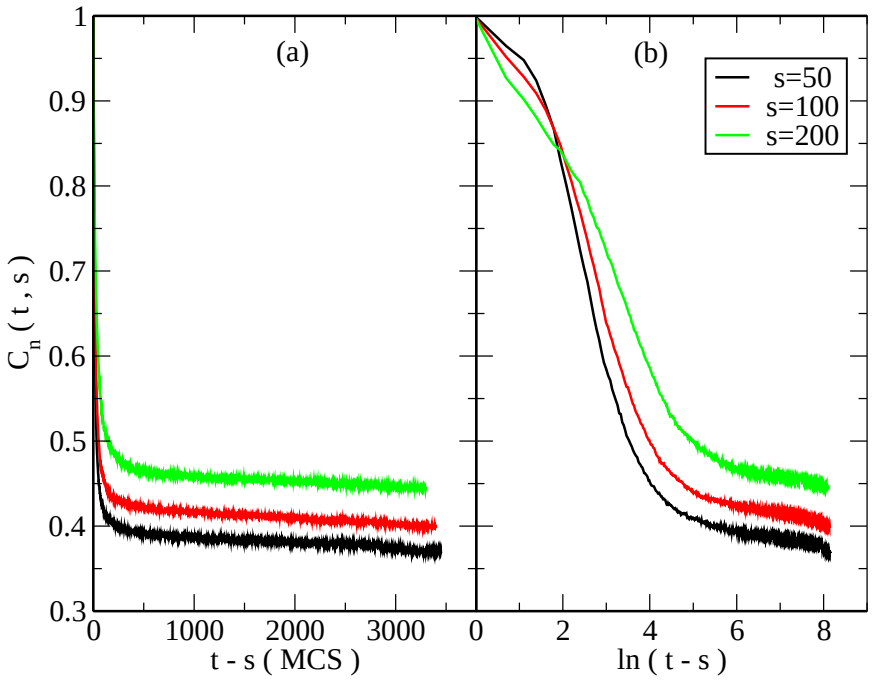

Figure 7.5: (a) The density autocorrelation function is plotted vs $t - s$. (b) The same data, but now plotted as a function of $\ln(t - s)$. The data reveal the existence of three distinct regimes.

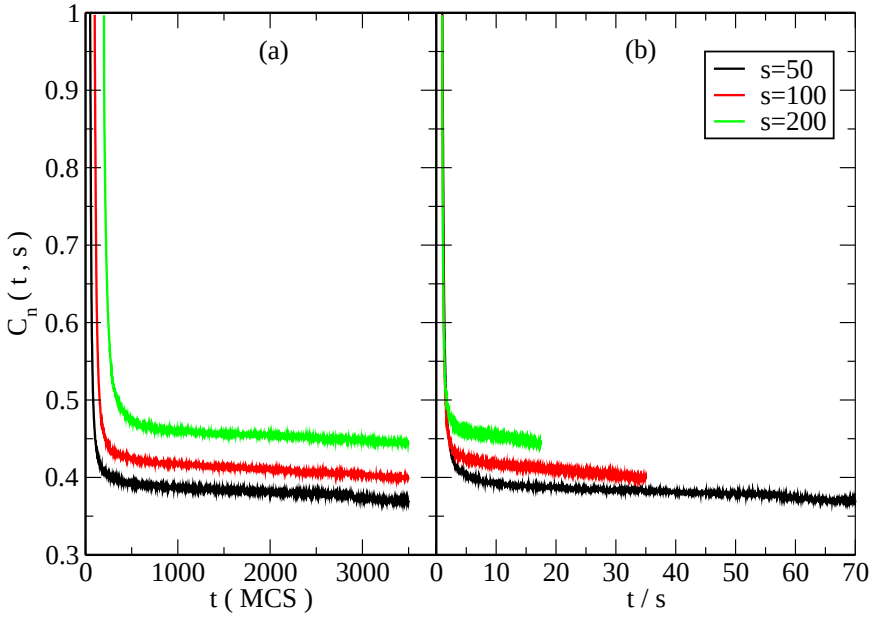

Figure 7.6: (a) The density autocorrelation function vs observation time t for the set of data shown in Fig. 7.4. (b) The density autocorrelation function is plotted vs t/s for the same set of data.

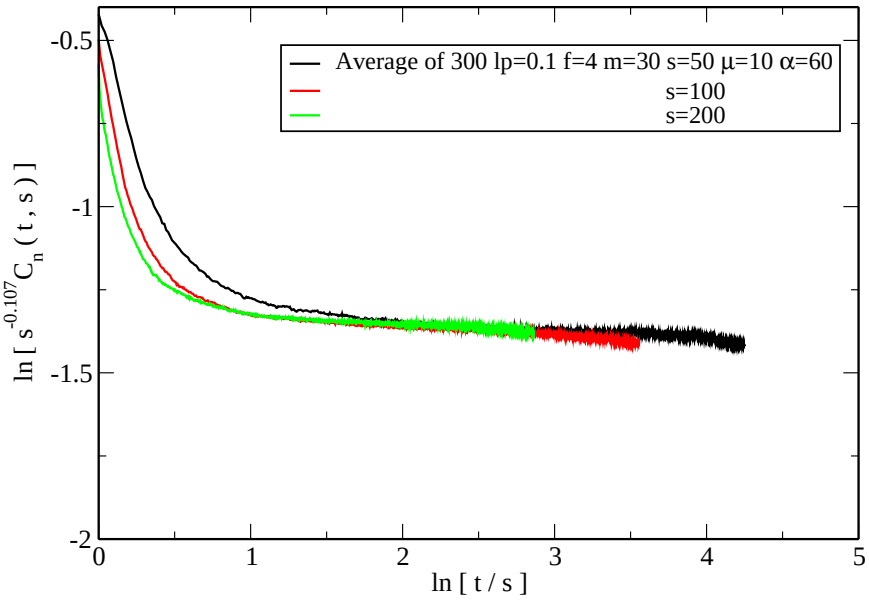

Figure 7.7: Dynamical scaling of the density autocorrelation function plotted as a function of t/s. The dynamical exponent is $b = -0,107$.

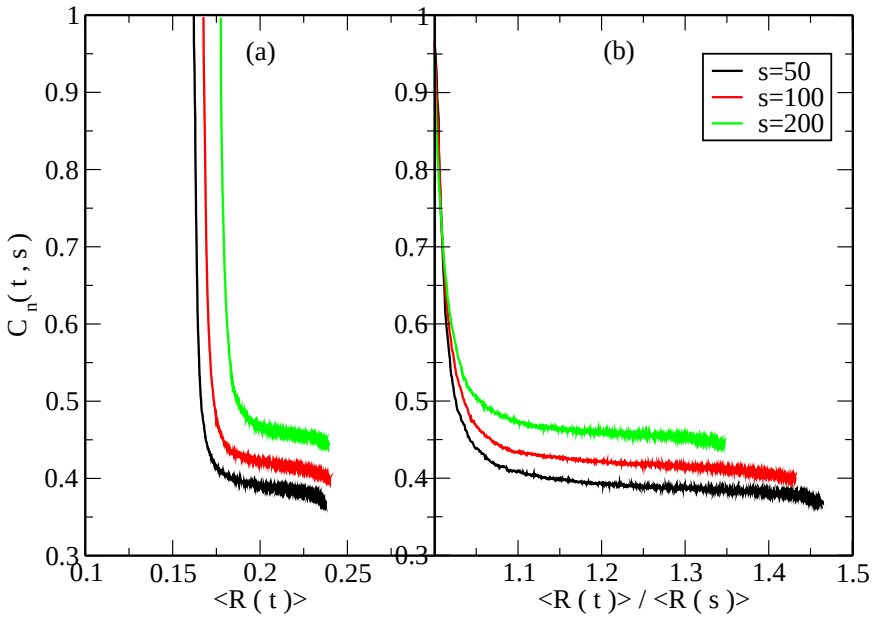

Figure 7.8: (a) The density autocorrelation function plotted as a function of $< R(t) >$ is showing three parallel curves for three waiting times $s = 50$ (black curve), 100 (red curve), and 200 (green curve). (b) The same data is plotted as a function of $< R(t) > / < R(s) >$.

7.4 Euclidean distance two-times function

The Euclidean distance two-times function also yields information on the dynamics of the system. The additional two-times function provides a complementary picture of the dynamics of the crosslinks. As

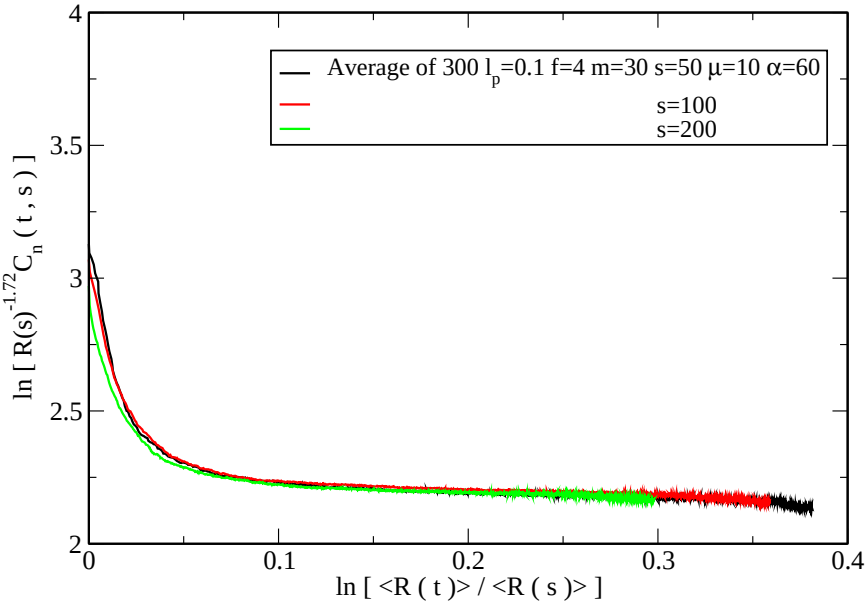

Figure 7.9: Dynamical scaling of the density autocorrelation function when plotted as a function of $< R(t) > / < R(s) >$. The data shows simple aging in the system with the exponent $b = -1.72$.

shown schematically in Fig. 7.10 this two-times function can provide interesting information in cases where the density two-times function does not allow to gain any insights. In our study we measure the connected

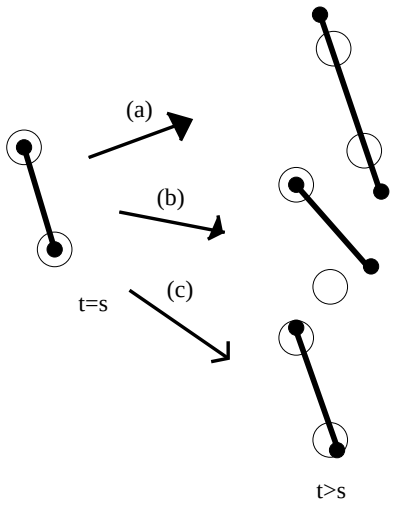

Figure 7.10: There are some situations where the Euclidean distance two-times function provides additional information on the conformation of the system. (a) Two crosslinks are out of the assigned spheres with radius $0.1l_p$. (b) Only one of the crosslinks is out out of its sphere. (c) Two of the crosslinks change their location but they are still inside the spheres. For this case the density two-times function will not show any change.

Euclidean distance two-times function,

$$C_{ED}(t,s) = < R(t)R(s) > - < R(t) >< R(s) > \tag{7.3}$$

$R(t)$ is the length of each segment at time t. $< R(t) >$ is the average over all segments in the system at time step t. According to our data the system shows a complex behavior over time, where the results depend on l_p, f, and α. For some of the parameters we observe aging scaling in the system. The typical behavior of the system is shown in figures 7.11 to 7.15. For the largest value of the persistence length we chose in our simulation, we note that the Euclidean distance two-times function is in the aging regime, see figures 7.11 and 7.12 where we plot the data as a function of t/s and $< R(t) > / < R(s) >$. For this large value of the persistence length, we find for the studied waiting times that the correlation function is monotonically decreasing. In fact, plotting the data as a function of $< R(t) > / < R(s) >$, see figure 7.12, yields curves

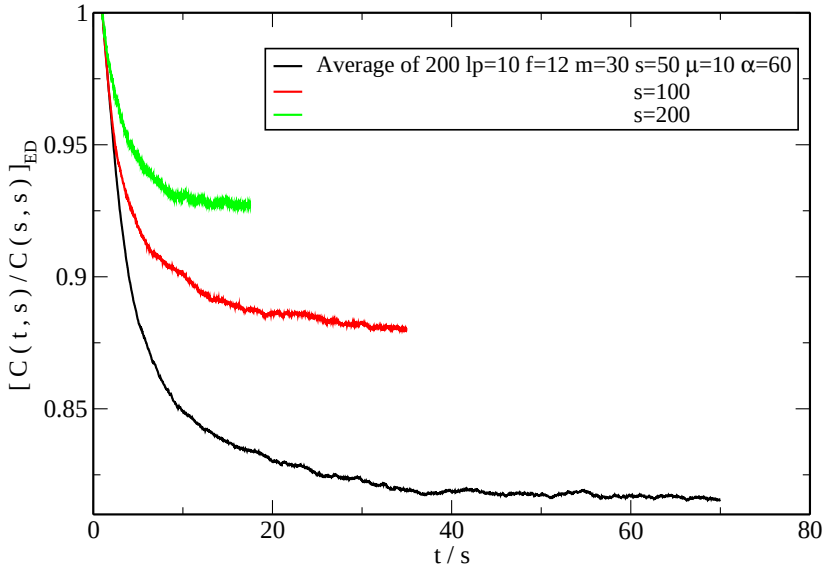

Figure 7.11: For $l_p = 10$, $f = 12$, $m = 30$, $\mu = 10$, and $\alpha = 60$, the average Euclidean distance two-times functions, $C(t,s)/C(s,s)_{ED}$, is plotted vs t/s.

that are approximately parallel, thus indicating the possibility of dynamical scaling. However longer waiting times are needed to really confirm that dynamical scaling occurs in those cases. In Figures 7.13 and 7.14 we show the behavior of the Euclidean distance two-times function for the smallest studied persistence length $l_p = 0.1$. In Fig. 7.13 the typical behavior of the Euclidean distance two-times function as a function of $< R(t) > / < R(s) >$ is shown for different waiting times and $l_p = 0.1$, $f = 8$, $m = 30$, $\mu = 10$, and $\alpha = 60$. The data show that for $s \leq 50$, the correlation function decays monotonically. However for the larger values $s = 100$ and 200, the function displays a maximum. If the shear angle decreases from $\alpha = 60$ to $\alpha = 30$, the position of the maximum is shifted to lower values.

Fig. 7.14 (a) reveals for $f = 4$ a complex and waiting time dependent behavior. The two-times function for $s = 50$, shown in black, is decreasing initially until at $t \sim 500$ an increase sets in. This is in contrast to the initial increase observed for large values of s. The Euclidean distance two-times function shows a complicated behavior that needs further study. Especially, the strong dependence on the value of the persistence length needs to be further elucidated.

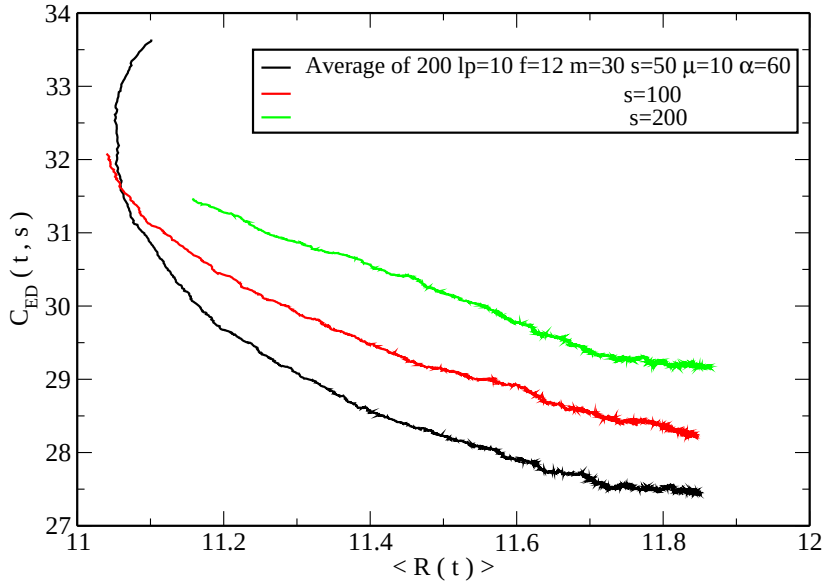

Figure 7.12: For $l_p = 10$, $f = 12$, $m = 30$, $\mu = 10$, and $\alpha = 60$, the average Euclidean distance two-times functions, $C_{ED}(t,s)$ is plotted vs $< R(t) >$.

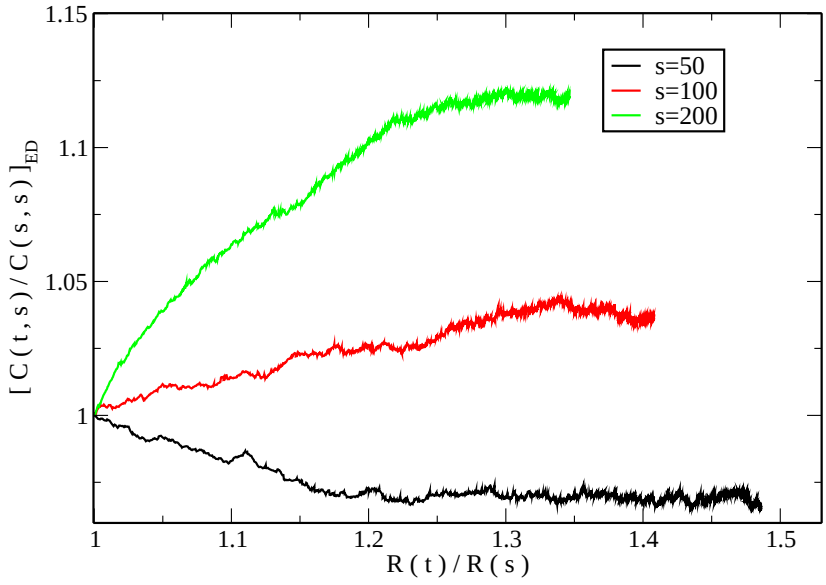

Figure 7.13: For $l_p = 0.1$, $f = 8$, $m = 30$, $\mu = 10$, and $\alpha = 60$, the average Euclidean distance two-times functions, $C_{ED}(t,s)$, is plotted vs $< R(t) >$.

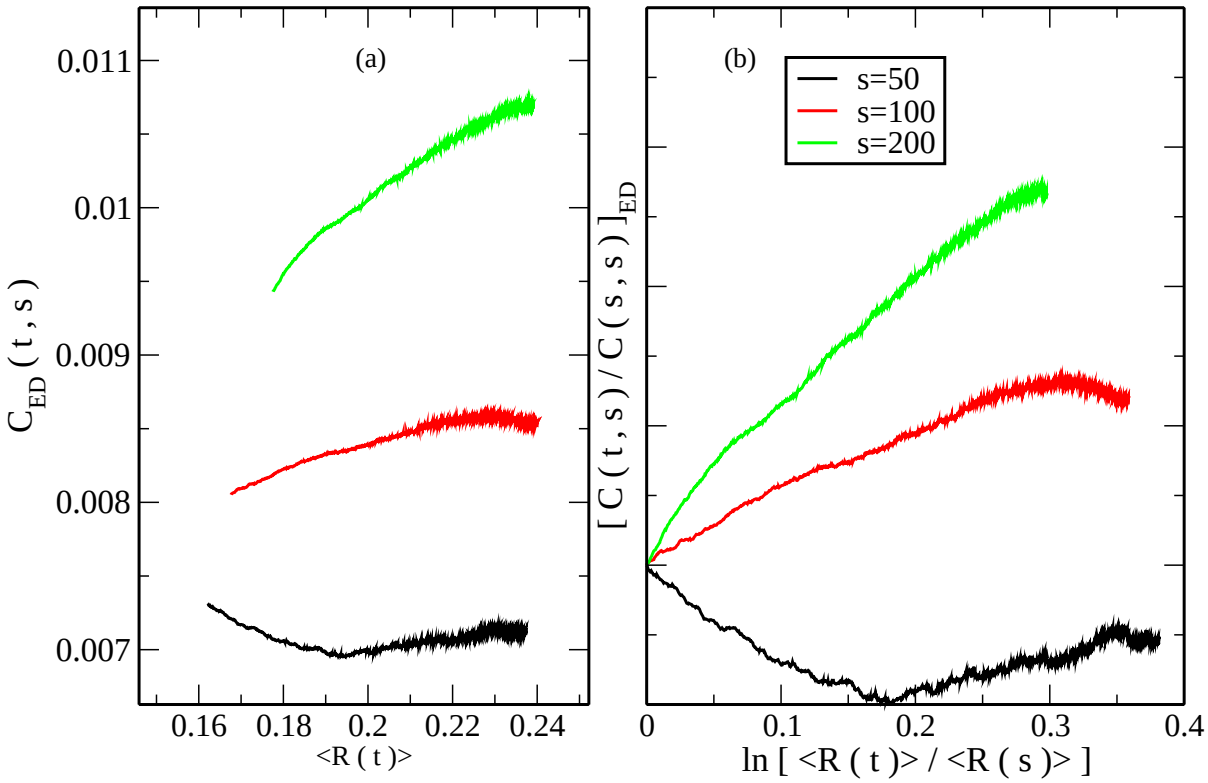

Figure 7.14: (a) $C(t,s)_{ED}$ vs $< R(t) >$ for $l_p = 0.1$, $f = 4$, $m = 30$, $\mu = 10$, and $\alpha = 60$. (b) $[C(t,s)/C(s,s)]_{ED}$ vs $< R(t) > / < R(s) >$.

Chapter 8

Conclusion

In this chapter we have investigated non-equilibrium relaxation processes taking place in reversible reaction-diffusion systems, in coarsening systems with anomalous slow dynamics as well as in polymer networks. Our conclusions for each project are given in separate sections.

8.1 Reversible reaction-diffusion system

Our particular models for reaction-diffusion systems consist of one- and two-dimensional lattice models with single occupancy of each species for each site. We study our systems through the investigation of the species densities, the two-times autocorrelation function, and the two-times response function. This systematic approach helps us to investigate the various scaling forms for the two-times functions. By varying the perturbation, we looked at different responses of the system.

When investigating the asymptotic behavior of reversible reaction-diffusion systems, one needs to take into account the slow dynamics that occurs in these systems. By comparing our results with the corresponding model without site restriction, we note that, the exponent describing the approach to the stationary state is the same. Our results for the response function with the conserved quantity K are the same as for the model without site restriction. We note that, the dynamical scaling of the response function depends on whether the perturbation conserves the quantity or not.

Future studies of reversible reaction-diffusion systems should consider other types of perturbations to further check the impact of the conservation of K on the response function. Moreover our present study can be generalized to much more complex reaction and diffusion schemes. It would be interesting to study the effects of the different perturbations on dynamical scaling for these more complex reaction and diffusion schemes.

8.2 Coarsening systems with anomalous slow dynamics

Motivated by the absence of systematic studies of aging in system with logarithmic growth expected in many disordered systems, we propose to follow a different route and to focus on model systems for which it is possible to access the logarithmic regime. We study the ABC-model and the domain ABC-model on a one-dimensional lattice with single site occupancy. In the ABC-model, the initial state of the system is prepared randomly. We focus on the domain length $L(t)$ which grows as a logarithmic function of time and on two-times autocorrelation functions. In the ABC-model it takes a long time to reach the asymptotic regime, whereas in the domain ABC-model the system reaches the asymptotic regime much faster. Our systematic approach allows us to investigate various scaling forms for two-times functions.

Our study of the ABC-model shows that the correlation function in the crossover regime can be rather complicated. Once the domains are formed and the system is in the logarithmic growth regime for large enough waiting times, the two-times autocorrelation functions start to reveal dynamical scaling. The data show dynamical scaling provided that the time dependence is expressed through the length scale $L(t)$ that increases logarithmically with time. Furthermore to study the response of the system to a perturbation, we keep the swapping rate q, the only parameter in the model, at some initial value q_i up to the waiting time s, where we then change this rate and set it equal to the final value q_f. The measured response function is then a time integrated response of the system. We find different behaviors depending on whether the q value increases or decreases. For the case when q decreases, we have dynamical scaling with the typical length $L(t)$ as scaling variable.

We view the present study of the ABC-model as a first step in the systematic study of aging properties of systems undergoing logarithmic growth. We expect additional insights through the study of two-times space-time autocorrelation functions. Also, in future one can consider a local response to the local perturbation instead of the time integrated global response.

8.3 A non-equilibrium polymer network: the cytoskeleton

In our final project we studied non-equilibrium polymer networks that can be used to describe the cytoskeleton. We investigate two- and three-dimensional models. The two-dimensional model describes the static properties of the system in the presence of perturbations. This model is similar to a birth-death model for link creation and dissolution. The three-dimensional model is a semiflexible polymer network used to study aging and non-equilibrium relaxation. The persistence length of the polymers, the number of filaments, and the amount of perturbation are all varied in order to systematically measure the Euclidean distance and density two-times functions. Furthermore, we investigate the dynamical scaling of these two-times functions.

In the two-dimensional model, we study the number of links which are created and dissolved with certain probabilities as a function of time. Moreover, the distribution of links as a function of the Euclidean distance of the crosslinks has been studied in the presence of various perturbations. For the three-dimensional model, we investigate the Euclidean distance and density two-times functions when shearing the system. Different values of the persistence length, the number of filaments, and shear angles are considered. The measured value of the average Euclidean distance is a power law function of time. For the density two-times function with $l_p = 0.1$, we see dynamical scaling for the density two-times function. For the Euclidean distance

two-times function, different behaviors are observed for different values of the persistence length.

Our study of the three-dimensional model focused on shear perturbation. In future, the aging of the system can also be studied through other types of perturbations such as bulk, uniaxial, and unilateral strains. Additionally, the global energy of the system and filaments' properties are other functions that can be studied. Furthermore, the buckling and mechanical moduli of the system are other interesting quantities that can be measured.

Bibliography

[1] Struik L. C. E., *Polymer Engineering and Science, March, Vol.17, No 3* (1977).

[2] Struik L. C. E. *Elsevier, Amsterdam* (1978).

[3] Henkel M. and Pleimling M., *Non-equilibrium Phase Transitions Vol. 2: Ageing and Dynamical Scaling Far from Equilibrium* (Dordrecht: Springer and Bristol: Canopus) (2010).

[4] Henkel M., Hinrichsen H. and Lübeck S. *Non-equilibrium Phase Transitions Vol. 1: Absorbing Phase Transitions* (Dordrecht: Springer and Bristol: Canopus) (2008).

[5] Henkel M. and Pleimling M., *Non-Equilibrium Phase Transitions, Volume 2: Ageing and Dynamical Scaling Far From Equilibrium* (Springer, Heidelberg, 2010).

[6] Ódor G., *Universality in Nonequilibrium Lattice Systems: Theoretical Foundations* (Singapore: World Scientific) (2008).

[7] Enss T., Henkel M., Picone A., and Schollwöck U., J. Phys. A: Math. Gen. **37**, 10479 (2004).

[8] Ramasco J. J., Henkel M., Santos M. A., and da Silva Santos C. A., J. Phys. A: Math. Gen. **37**, 10497 (2004).

[9] Baumann F., Henkel M., Pleimling M., and Richert J, J. Phys. A: Math. Gen. **38**, 6623 (2005).

[10] Hinrichsen H., J. Stat. Mech., L06001 (2006).

[11] Ódor G., J. Stat. Mech., L11002 (2006).

[12] Baumann F., Stoimenov S., and Henkel M., J. Phys. A: Math. Gen. **39**, 4905 (2006).

[13] Baumann F. and Gambassi A., J. Stat. Mech., P01002 (2007).

[14] Takeuchi K. A., Kuroda M., Chaté H, and Sano M, Phys. Rev. Lett. **99**, 234503 (2007).

[15] Henkel M., J. Phys. Condens. Matt. **19**, 065101 (2007).

[16] Durang X. and Henkel M., J. Phys. A: Math. Gen. **42**, 395004 (2009).

[17] Durang X., Fortin J-Y., Del Biondo D., Henkel M. and Richert J., J. Stat. Mech., P04002 (2010).

[18] Durang X., Fortin J-Y. and Henkel M. 2011 *J. Stat. Mech.,* P02030 (2011).

[19] Zel'dovich Y. B. and Ovchinnikov A. A., JETP Lett. **26**, 440 (1997).

[20] Zel'dovich Y. B. and Ovchinnikov A. A., Sov. Phys. JETP **47**, 829 (1977).

[21] Kang K. and Redner S., Phys. Rev. A **32**, 435 (1985).

[22] Oshanin G. S. and Burlatsky S. F., J. Phys. A **22**, L973 (1989).

[23] Oshanin G. S., Ovchinnikov A. A., and Burlatsky S F, J. Phys. A **22**, L977 (1989).

[24] Agmon N. and Edelstein A. L., J. Chem. Phys. **100**, 4181 (1994).

[25] Agmon N. and Edelstein A. L., J. Phys. Chem. **99** 5389 (1995).

[26] Rey P-A. and Cardy J., J. Phys. A **32**, 1585 (1999).

[27] Gopich I. V. and Agmon N., Phys. Rev. Lett. **84**, 2730 (2000).

[28] Agmon N. and Gopich I. V., J. Chem. Phys. **112**, 2863 (2000).

[29] Gopich I. V. and Szabo A., Chem. Phys. **284**, 91 (2002).

[30] Huppert D., Goldberg S. Y., Masad A., and Agmon N., Phys. Rev. Lett. **68**, 3932 (1992).

[31] Solntsev K. M., Huppert D., and Agmon N., J. Phys. Chem. A **105**, 5868 (2001).

[32] Pines D. and Pines E., J. Chem. Phys. **115** 951 (2001).

[33] Elgart V. and Pleimling M., Phys. Rev. E **77**, 051134 (2008).

[34] Bray A. J. , Adv. Phys. **43**, 357 (1994).

[35] Henkel M., J. Phys.: Condens. Matter **19**, 065101 (2007).

[36] Cugliandolo L. F. in *Slow Relaxation and Non-equilibrium Dynamics in Condensed Matter*, editors Barrat J.-L., Dalibard J., Kurchan J., and Feigel'man M. V., (Springer, 2003).

[37] Kolton A., Rosso A., and Giamarchi T., Phys. Rev. Lett. **95**, 180604 (2005).

[38] Noh J. D. and Park H., Phys. Rev. E **80**, 040102(R) (2009).

[39] Iguain J. L., Bustingorry S., Kolton A. B., and Cugliandolo L. F., Phys. Rev. B **80**, 094201 (2009).

[40] Monthus C. and Garel T., J. Stat. Mech., P12017 (2009).

[41] Park H. and Pleimling M., Phys. Rev. B **82**, 144406 (2010).

[42] N. Afzal and M. Pleimling, Phys. Rev. E **87**, 012114 (2013).

[43] Corberi F., Cugliandolo L. F., and Yoshino H., in *Dynamical Heterogeneities in Glasses, Colloids, and Granular Media*, edited by Berthier L., Biroli G., Bouchaud J.-P., Cipelleti L., and Van W.Saarloos (Oxford University Press, Oxford, 2011).

[44] Corberi F., Lippielli E., Mukherjee A., Puri S., and Zannetti M., Phys. Rev. E **85**, 021141 (2012).

[45] Park H. and Pleimling M., Eur. Phys. J. B **85**, 300 (2012).

[46] Huse D. A. and Henley C. L., Phys. Rev. Lett. **54**, 2708 (1985).

[47] Evans M. R., J. Phys.: Condens. Matter **14**, 1397 (2002).

[48] Evans M. R., Kafri Y., Koduvely H. M., and Mukamel D., Phys. Rev. Lett. **80**, 425 (1998).

[49] Evans M. R., Kafri Y., Koduvely H. M., and Mukamel D., Phys. Rev. E **58**, 2764 (1998).

[50] Clincy M., Derrida B., and Evans M. R., Phys. Rev. E **67**, 066115 (2003).

[51] Bodineau T., Derrida B., Lecomte V., and van Wijland F., J. Stat. Phys. **133**, 1013 (2008).

[52] Ayyer A., Carlen E. A., Lebowitz J. L., Mohanty P. K., Mukamel D., and Speer E., J. Stat. Phys. **137**, 1166 (2009).

[53] Lederhendler A. and Mukamel D., Phys. Rev. Lett. **105**, 150602 (2010).

[54] Lederhendler A., Cohen O., and Mukamel D., J. Stat. Mech. (2010) P11016.

[55] Barton J., Lebowitz J. L., and Speer E. R., J. Phys. A: Math. Theor. **44**, 065005 (2011).

[56] Bertini L., Cancrini N., and Posta G., J. Stat. Phys. **144**, 1284 (2011).

[57] Barton J., Lebowitz J. L., and Speer E. R., J. Stat. Phys. **145**, 763 (2011).

[58] Gerschenfeld A. and Derrida B., EPL **96**, 20001 (2011).

[59] Cohen O. and Mukamel D., J. Phys. A: Math. Theor. **44**, 415004 (2011).

[60] Bodineau T. and Derrida B., J. Stat. Phys. **145**, 745 (2011).

[61] Gerschenfeld A. and Derrida B., J. Phys. A: Math. Theor. **45**, 055002 (2012).

[62] Cohen O. and Mukamel D., Phys. Rev. Lett. **108**, 060602 (2012).

[63] Cohen O. and Mukamel D., arXiv:1210.3788.

[64] Lahiri R. and Ramaswamy S., Phys. Rev. Lett. **79**, 1150 (1997).

[65] Arndt P. F., Heinzel T., and Rittenberg V., J. Phys. A: Math. Gen. **31**, L45 (1998).

[66] Lahiri R., Barma M., and Ramaswamy S., Phys. Rev. E **61**, 1648 (2000).

[67] Kafri Y., Biron D., Evans M. R., and Mukamel D., Eur. Phys. J. B **16**, 669 (2000).

[68] Lipowski A. and Lipowska D., Phys. Rev. E **79**, 060102(R) (2009).

[69] Calabrese P. and Gambassi A., J. Phys. A: Math. Gen. **38**, R133 (2005).

[70] Afzal N., Waugh J., and Pleimling M., J. Stat. Mech. (2011) P06006.

[71] Ahmed A., Konrad D., and Pleimling M., J. Stat. Mech. (2012) P07014.

[72] Vincent E., in *Ageing and the Glass Transition*, Lecture Notes in Physics **716**, edited by Henkel M., Pleimling M., and Sanctuary R. (Springer, Berlin, Heidelberg, 2007).

[73] Mukherjee T., Pleimling M., and Binek Ch., Phys. Rev. B **82**, 134425 (2010).

[74] Henkel M., Noh J. D., and Pleimling M., Phys. Rev. E **85**, 030102(R) (2012).

[75] Barrat A., Phys. Rev. E **57**, 3629 (1998).

[76] Afzal N. and Pleimling M.,Phys. Rev. E **87**, 012114 (2013).

[77] Lieleg O., Nat. Mat. **10** 236-242 (2011).

[78] Ingber D.E., J. Cell Sci. **104** 613-627 (1993).

[79] Fuller B., Portfolio Artnews Annual, **4** 112-127 (1961).

[80] Cytoskeletal Mechanics Models and measurement (Cambridge University Press 2006), Edited by M. R. K Mofrad and R. Kamm (2006).

[81] Sander E. A. et al., Trends in Computational Nanomechanics, Chapter 19, Out of Many One: Modeling Schemes for Biopolymer and Biofibril Network, 557-602 (2010).

[82] Wang N., Butler J.P. and Ingber D.E., Science, **26** 1124-1127 (1993).

[83] Bray D., Heat J. and Moss D., J. Cell Sci. Suppl., **4** 71-88 (1986).

[84] Boey S. K., Boal DH and Discher D.E., Biophys. J. **75** 1537-1583 (1998).

[85] Coughlin M. F. and Stamenovic D., Biophys. J. **84** 1328-1336 (2003).

[86] Coughlin M. F. and Stamenovic D., ASME J. Biomech.Eng., **120** 770-777 (1998).

[87] Mandadapu K. K., Govindjee S. and Mofrad M.R.K., J. of Biomech. **41** 1467-1478 (2008).

[88] Cloitre M., Borrega R. and Leibler R., Phys. Rev. Lett., **85** 4819-4822 (2000).

[89] Ramos L., Cipelletti L., Phys. Rev. Lett. **87** 245503 (2001).

[90] Kratky O., Porod G., Recl. Trav. Chim. **68** 1106 (1949).

[91] Kronick P. L. and Sacks M. S., Connect. Tissue Res., **27** 1-13 (1991).

[92] Billiar K. L. and Sacks M. S. J. Biomech., **30** 753-756 (1997).

[93] Heussinger C. and Frey E., Phys. Rev. E **75**, 011917 (2007).

[94] Pourdeyhimi B., Ramanathan R., Dent R., Text. Res. J., **66** 713-722 (1996).

[95] Head D. A. and et al., Phys. Rev. E, **68** 061907 (2003).

[96] Kellomaki M. and et al., Phys. Rev. Lett., **77** 2730-2733 (1996).

[97] Howard J., Mechanics of motor proteins and the cytoskeleton, (Sunderland, MA: Sinauer Associate, 2001, 367pp) (2001).

[98] Janmey P. A. and et al., Nat. Mater, **6**, 48-51 (2007).

[99] Doi M. and Edwards S. F., The theory of polymer dynamics, (New York: Oxford University Press, 1986).

[100] MacKintosh F. C. and et al., Phys. Rev. Lett. **75** 4425-4428 (2007).

[101] Chandran P. L. and et al., J. Biomech. Eng. **128** 259-270 (2006).

[102] Wyart M. and et al., Arxiv 0806.4653, (2008).

[103] Palmer J. S. and et al., Acta. Biomaterialia. **4**, 597-612 (2008).

[104] Klapper I. and et al., Biophys. J., **74**, 2504-2514 (1998).

[105] Sastry A. M. and et al., J. Thermoplast. Compos. Matter., **11** 288-296 (1998).

[106] Bathe K. J., Finite element procdures, New Jersery: Prentice-Hall (1996).

[107] Risler T., arXiv:1105.2423v1 [physics.bio-ph] (2011).

[108] Stamenovic D. et al., J. Appl. Physiol. **96** 1600-1605 (2004)

[109] Fabry B and Fredberg J., Resp. Phys. and Neur. **137** 109-124 (2003).

[110] Bouchaud J., Journal de Physique I France 2, 1705-1713 (1996).

[111] Monthus C. and Bouchaud J., Journal of Physics A, **29**, 3847-3869 (1996).

[112] Sollich P., Phys. Rev. E, **58** 738 (1997).

[113] Bursac P. at al., Nature material, **4** 557-561 (2005).

[114] Reese S. and Govindjee S., Int. J. Solids and Struct., **35**, 3455-3482 (1998).

[115] Reese S. and Govindjee S., ASME. J. Eng. Mat. and Tech., **119**, 251-255 (1998).

[116] Trepat X., Nature, **447**, 592-596 (2007).

[117] Fabry B. et al., Phys. Rev. Lett., **87** 148102 (2001).

[118] Fabry B. et al., Phys. Rev. E., **68** 041914 (2003).

[119] Landau D. P. and Binder K. 2005 *A guide to Monte Carlo simulation in statistical physics* (Cambridge, New York, 2005).

[120] Marko J. F. and Siggia E. D., Macromolecules, **28** 8759 (1995).

[121] Wooten F., Winer K., and Weaire D., Phys. Rev. Lett, **54**, 1392-1395 (1985).

[122] Barkema G. T. and Mousseau N., Phys.Rev. B, **62**, 4985-4990 (2000).

[123] Wilhelm J. and Frey E., Phys. Rev. Lett., **77**, 2581-2584 (1996).

[124] Lees A. W. and Edwards S F., J. Phys. C: Solid State Phys., **5**, 1921 (1972).

[125] Huisman E. M. et. al, Phys. Rev. E., **78**, 051801 (2008).

[126] Huisman E. M. et. al, Phys. Rev. Lett., **99**, 208103 (2007).

[127] Storm C., Pastore J. J., MacKintosh F. C., Lubensky T. C., and Janmey P. A., Nature Publishing Group, **435** 191-194 (2005).

[128] Wang I. and Ingber D.E., Control of the Cytoskeletal Mechanics by Extra Cellular Matrix, Cell Shape and Mechanical Tension, **66**, 2181-2189 (1994).

[129] Binder K., Walter K. H and Lübeck S., Glassy Materials and Disordered Solids, (World Scientific Publisher Co. Pte. Ltd.) (2008).

[130] Gunst et. al, J. Appl. Physiol., **95**, 413-425 (2003).

[131] Silveria P. S. P. et. al, J. Appl. Physiol., **99**, 2087 (2005).

[132] Latouche G., Ramaswami V. 1999 *Introduction to Matrix Analytic Methods in Stochastic Modeling, 1st edition. Chapter 1: Quasi-Birth-and-Death Processes; ASA SIAM, 1999.*

[133] Schaller V., Weber C., Semmrich C., Frey E. and Bausch A. R., nature, **467**, 73-77 (2010).

[134] Kratky O. and Porod G., Recl. Trav. Chim., **68**, 1106 (1949).

[135] Yamakawa H. 1971 *Modern Theory of Polymer Solutions*(Harper and Row, New York, 1971).

[136] Daniels H. E., Proc. R. Soc., **63A**, 29 (1952).

[137] Gobush W. et. al, J. Chem. Phys., **57**, 2839 (1972).

[138] Hermans J. J. and Ullman R., Physica (Utrecht), **18**, 951 (1952).

[139] Yamakawa H. and Fujii M., Macromolecules, **7**, 649 (1974).

[140] Gittes F. et. al, J. Cell Biology, **120**, 923 (1993).

[141] K*ä*s et. al, Europhysics Letter, **21**, 865 (1993).

[142] Ott A. M. et. al, Phys. Rev. E., **48**, R:1642 (1993).